UNIVERSITY OF KWAZULU-NATAL

MACHINE LEARNING, CLASSIFICATION OF 3D UAV-SFM POINT CLOUDS IN THE UNIVERSITY OF KWAZULU-NATAL (HOWARD COLLEGE)

By

Simiso Siphenini Ntuli

Submitted in fulfilment of the academic requirements for the degree of

Master of Science in Land Surveying

School of Engineering

College of Agriculture, Engineering and Science

University of KwaZulu-Natal

December 2020

Supervised by: Mr A.M. Forbes

As the candidate's Supervisor I agree to the submission of this thesis.

_____   _____

Mr A.M. Forbes   Date
(Supervisor)

PREFACE

The research contained in this thesis was completed by the candidate while based in the Discipline of Land Surveying, School of Engineering of the College of Agriculture, Engineering and Science, University of KwaZulu-Natal, Howard College, South Africa. The research was financially supported by the South Africa's National Research Foundation (NRF).

The contents of this work have not been submitted in any form to another university and, except where the work of others is acknowledged in the text, the results reported are due to investigations by the candidate.

DECLARATION 1 – PLAGIARISM

I, Simiso Ntuli declare that:

1. The research reported in this thesis, except where otherwise indicated, and is my original research.

2. This thesis has not been submitted for any degree or examination at any other university.

3. This thesis does not contain other persons' data, pictures, graphs or other information, unless specifically acknowledged as being sourced from other persons.

4. This thesis does not contain other persons' writing, unless specifically acknowledged as being sourced from other researchers. Where other written sources have been quoted, then:

   a) their words have been re-written but the general information attributed to them has been referenced;

   b) where their exact words have been used, their writing has been placed inside quotation marks, and referenced.

5. This thesis does not contain text, graphics or tables copied and pasted from the Internet, unless specifically acknowledged, and the source being detailed in the thesis and in the References sections.

_____

Signed: Simiso Ntuli

Date: 01 December 2020

ACKNOWLEDGEMENTS

ABSTRACT

Three-dimensional (3D) point clouds derived using cost-effective and time-efficient photogrammetric technologies can provide information that can be utilized for decision-making in engineering, built environment and other related fields. This study focuses on the use of machine learning to automate the classification of points in a heterogeneous 3D scene situated in the University of KwaZulu-Natal, Howard College Campus sports field.

The state of the camera mounted on the unmanned aerial vehicle (UAV) was evaluated through the process of camera calibration. Nadir aerial images captured using a UAV were used to generate a 3D point cloud employing the structure-from-motion (SfM) photogrammetric technique. The generated point cloud was georeferenced using natural ground control points (GCPs). Supervised and unsupervised classification approaches were used to classify points into three classes: ground, high vegetation and building. The supervised classification algorithm used a multi-scale dimensionality analysis to classify points. A georeferenced orthomosaic was used to generate random points for cross-validation. The accuracy of classification was evaluated, employing both qualitative and quantitative analysis.

The camera calibration results showed negligible discrepancies when a comparison was made between the results obtained and the manufacturer's specifications in parameters of the camera lens; hence the camera was in the excellent state of being used as a measuring device. Site visits and ground truth surveys were conducted to validate the classified point cloud. An overall root-mean-square (RMS) error of 0.053m was achieved from georeferencing the 3D point cloud. A root-mean-square error of 0.032m was achieved from georeferencing the orthomosaic. The multi-scale dimensionality analysis classified a point cloud and achieved an accuracy of 81.3% and a Kappa coefficient of 0.70. Good results were also achieved from the qualitative analysis. The classification results obtained indicated that a 3D heterogeneous scene can be classified into different land cover categories. These results show that the classification of 3D UAV-SfM point clouds provides a helpful tool for mapping and monitoring complex 3D environments.

TABLE OF CONTENTS

TABLE OF FIGURES

xii

LIST OF TABLES

LIST OF ACRONYMS

2D	Two-dimensional
3D	Three-dimensional
AI	Artificial Intelligence
API	Application Program Interface
ANN	Artificial Neural Network
CANUPO	CAractérisation de NUages de POints
CCD	Charge-coupled device
CMVS	Clustering Multi-View Stereo
CNN	Convolutional Neural Network
CRF	Conditional Random Fields
DSLR	Digital single-lens reflex
DSM	Digital Surface Model
DTM	Digital Terrain Model
EC	Error of commission
EO	Error of omission
Exif	Exchangeable image file format
FoV	Field of View
FW	Full-waveform
GBT	Gradient Boosted Trees
GCP	Ground Control Point
GIS	Geographical Information System
GNSS	Global Navigation Satellite System
GPS	Global Positioning System
ISODATA	Iterative Self-Organizing Data Analysis Techniques
LiDAR	Light Detection and Ranging
MVS	Multi-View Stereo
OA	Overall Accuracy
PA	Producers Accuracy
PMVS	Patch-based Multi-View Stereo
RF	Random Forests
RGB	Red, Green and Blue
RGB-D	Red, Green and Blue – Depth
RMS	Root-mean-square

RPAS	Remotely-Piloted Aerial System
SACAA	South African Civil Aviation Authority
SfM	Structure-from-Motion
SGM	Stacked graphical model
SIFT	Scale Invariant Feature Transform
SVM	Support Vector Machine
TLS	Terrestrial Laser Scanner
UA	Users Accuracy
UAS	Unmanned aerial systems
UAV	Unmanned aerial vehicle
UTM	Universal Transverse Mercator

CHAPTER 1

INTRODUCTION

1.1 Background

Classifying different objects is not a complicated function for humans, but it has been determined to be an intricate issue for machines (Kamavisdar et al., 2013). There is a necessity to automate the detection of objects since it yields results that can be employed in the determination of information for various applications, such as the creation of 3D city replicas for representation and simulations (Niemeyer et al., 2012).

Remote sensing technologies are advancing, leading to the escalated necessity of acquiring point cloud data. These technologies incorporate but are not limited to UAV-based photogrammetry, consumer RGB-D sensor (low cost), and indoor mobile mapping (Liu and Boehm, 2015).

1.1.1 Unmanned Aerial Vehicles (UAVs)

UAVs are becoming popular in various fields due to their capacity to present in a flexible manner high-quality spatial information; also, they are cost-effective. Their ability to perform a simultaneous collection of high-resolution imagery and a photogrammetric point cloud is a unique advantage enabling a wide range of applications including but not limited to agriculture, geomorphology, cultural heritage, forestry and damage assessment (Gevaert et al., 2016).

The United States Department of Defense (DOD), together with the Civil Aviation Authority (CAA) of the United Kingdom, adopted the term UAS (Unmanned Aerial Systems), now commonly known as UAVs or drones (ICAO, 2011). The concept of Remotely-Piloted Aerial System (RPAS) was established by the International Civil Aviation Organization (ICAO) in order to incorporate the RPAS into the civil aviation system internationally (ICAO, 2011; Colomina et al., 2014). In South Africa, the term RPAS is also used by the South African Civil Aviation Authority (2017). Figure 1-1 (DJI, 2017) shows a quadcopter UAV Phantom 1 with a CCD camera as a payload.

Figure 1-1: Phantom 1, unmanned aerial vehicle

The use of UAVs has some concerns, including privacy, safety and security, which should be guided by proper regulations and policies (Shakhatreh et al., 2019). To regulatory bodies, policymakers, and all other mapping authorities world-wide, Colomina et al. (2014) published a journal article sending a message, **"***Let them fly and they will create a new remote sensing market in your country***."**

1.1.2   3D Point Clouds

The point clouds are created by a massive quantity of data with many redundant coordinates (Rodríguez et al., 2019). They are a collection of points, each associated with X, Y, Z coordinate in some three-dimensional coordinate system (Van Genechten, 2008). Point clouds may have additional information, for example, reflectivity values and color (Van Genechten, 2008).

The terrestrial laser scanner (TLS) is the first instrument that was used to collect a point cloud. Like other surveying instruments, a TLS is mounted and levelled over a tripod (Rodríguez et al., 2019). Based on the environment of which laser scanning is performed, the parameters are configured before commencing the collection of points. The collected points are referenced to the scanner's coordinate system with the laser optical center as the origin for each scan (Rodríguez et al., 2019). These scans need to be brought together by registration, whereby the transformation of points from the local to the ground coordinate system is performed. This is done using targets known as common or tie points (Akca, 2003).

Points in a point cloud are joined seamlessly to form a mesh, which is a 3D solid surface resulting from the triangulation process (Van Genechten, 2008). A mesh is usually the final product in the process of 3D modelling, and it can be textured by giving color information (Cignoni et al., 2008). There is a vast number of applications in which point clouds are utilized. Since point clouds are associated with high accuracies, they are employed in construction, agriculture, risk assessment, monitoring, and preservation of cultural objects (Abmayr et al., 2005; Zogg et al., 2008).

1.1.3   What is Point Cloud Classification

Point cloud classification is the operation of labeling a segment of points with a class, assigning some semantic to a group of points (Guo et al., 2015; Weinmann et al., 2013). Supervised, unsupervised, and interactive classification approaches are the commonly utilized techniques in assigning class labels (Grilli et al., 2017). For example, a particular class, vegetation, can be assigned a value of 1 while a different label is issued to another class. The classification objective determines the type of information obtained and the style in which labels are assigned to classes (Kumar et al., 2019). Point cloud classification has numerous applications: environmental modeling, navigation, damage assessment, and cultural heritage (Grilli et al., 2017; Roynard et al., 2018).

1.2 Research Problem

Classification of lidar data into different land cover categories has been a centre of attention in numerous studies, mainly 2.5D airborne lidar data (Antonarakis et al., 2008; Sithole and Vosselman, 2004). In machine learning, the classification of 3D photogrammetric point clouds is still a problem (Liu and Boehm, 2015). Working with point cloud data is very convenient in a wide range of applications. Extensive information carried by point cloud data can be employed for various analyses, such as identifying an object in a scene comprising of different items of different sizes and shapes.

Ground and non-ground points require to be identified for design purposes in engineering and construction. Therefore, it is essential to address the classification problem as it may provide solutions to multiple disciplines such as forestry, geomorphology, agriculture, damage assessment, and cultural heritage (Gevaert et al., 2016).

1.3 Research Motivation

The study area of this research is situated at the University of KwaZulu-Natal (Howard College Campus) sports field. The budget towards travel costs will be minimal, and this area is easily accessible. The sports field comprises different features, both natural and man-made, which are suitable to be utilized in the classification of 3D point clouds. Undertaking surveys using UAV photogrammetry requires authorization to fly over a specific area. In addition, there is legislation about the use of drones, regulated by the South African Civil Aviation Authority (SAACA). Since the study area is within Erf 12494 Durban, which is the University of KwaZulu-Natal (Howard College Campus), no special consent is required to fly.

The use of new technologies plays a vital role in spatial modeling and visualization of 3D objects. Alonso (2019) states, "*In the drone industry, and the geospatial sector more broadly, there is a lot of talk about how AI will help extract actionable information from unstructured image data at a scale and speed never previously seen.*" Classification of photogrammetric point clouds requires more research, unlike image classification that has been done satisfactorily in the research industry. The applications of UAV photogrammetry using Structure-from-Motion are increasing in different fields. This study will be mainly conducted using open-source software with the primacy of being cost-effective. The classification of point clouds may provide numerous solutions for decision-making in engineering, built environment and other related fields.

1.4 Research Question

The research question was formulated based on the research problem and motivation as:

Employing the UAV-based and Structure-from-Motion (SfM) photogrammetry to create a 3D point, how can 3D point clouds in a heterogeneous environment be classified?

1.5 Aim and Objectives

1.5.1 Aim

This research aims to perform the classification of 3D point clouds generated from UAV-based photogrammetry using an automated approach and using training samples to produce a classified point cloud. In addition, assessing the classification accuracy and determine the possible applications of 3D point cloud classification.

1.5.2 Objectives

1. Find the most suitable area of study comprising of different features to be utilized for point cloud classification.
2. Evaluate the state of the UAV payload, which is an RGB camera, through the process of camera calibration.
3. Generate a 3D point cloud using the Structure-from-Motion photogrammetric technique and georeference the resulting cloud.
4. Perform the unsupervised and supervised classification techniques on the point cloud and evaluate the competence of classification.

1.6 Structure of the Thesis

This thesis contains seven chapters:

- Chapter 1 is a brief introduction to this research. The context of the problem (classification of 3D point clouds) is outlined, the aim and objectives are discussed, giving solutions to the main problem.

- Chapter 2 is based on the review of literature from previous research. The processes involved from image acquisition to the final classified product are discussed. This chapter explores various techniques employed in addressing the classification problem of different data formats and, lastly, the applications.

- Chapter 3 introduces the study area employed in this research. A geographical representation of this area is defined.

- Chapter 4 discusses the methodology used in this research. The steps undertaken from planning, preparation, classification, and lastly, assessment of accuracy.

- Chapter 5 presents the results obtained from camera calibration and classification accuracy of the 3D point cloud. Further analyses are discussed.

- Chapter 6 is the overall discussion of this research; the key objectives of this study are discussed.

- Chapter 7 is the conclusion of this thesis. The recommendations and future applications on the classification of 3D point clouds are outlined.

CHAPTER 2

LITERATURE REVIEW

2.1   Introduction

This chapter reviews the theoretical and practical concepts based on previous research undertaken on classification. The sub-topics covered include Traditional and Structure-from-Motion photogrammetry from computer vision using unmanned aerial vehicles, image classification, LIDAR classification, 3D point cloud classification, classification techniques, and assessment of accuracy. Classification is reviewed from different data formats since the same concept is used to achieve products such as thematic maps. Point clouds are explained in detail and their applications in various fields.

2.2   Point Cloud

A point cloud is explained as a collection of points having XYZ coordinates arranged in some three-dimensional coordinate system representing an object. Point clouds may contain some extra information, for instance, colour and reflectivity values (Van Genechten, 2008).

There is a vast range of methods to acquire 3D point clouds. Point clouds are extracted from raw data scanned from physical objects and structures such as building exteriors and interiors, process plants, topographies, and other manufactured items (Autodesk, 2018). These are from significant principles: Stereo vision, Active triangulation, and Laser time-of-flight measurement (Wulf and Wagner, 2003). Figure 2-1 (Eling and Klingbeil, 2015) shows a 3D point cloud generated using SfM.

Figure 2-1: Point cloud from SfM

2.2.1 Structure-from-Motion

2.2.1.1 Introduction

Structure-from-Motion (SfM) is introduced, and the stages involved are discussed from the beginning (acquisition of image data) to the end (point cloud). The word SfM comes from the computer vision community; the structure is produced by the images taken from a sensor in motion (Spetsakis and Aloimonos, 1991).

High-resolution data acquired at a low-cost, easy-to-use method of photogrammetry at different scale extents is achieved using SfM. The SfM technique automates the decoding of scene geometry and camera pose at the same time by using image matching. Unlike classical photogrammetry that requires the ground control points and camera pose(s) to perform triangulation and 3D reconstruction. (Liu and Boehm, 2015).

Classical photogrammetry relies on ground control points that are located manually on images to find the position of the camera. There is a distinction between classical photogrammetry and SfM. No prior information is needed to perform scene reconstruction when using SfM. SfM plays a vital role in acquiring datasets from remote areas and regions that are not easily accessible (Westoby et al., 2012).

During the image acquisition, short camera baselines should be maximized. A high percentage of overlap of images is required for offset images. The images are captured in different directions and positions (Micheletti et al., 2015). The survey should be adequately planned before image acquisition. It is advisable to initially take the image of the whole area or object, checking if the obstructions are included before taking overlapping images. The coverage should be such that it allows a point to be visible in three consecutive images taken from distinct locations, see figure 2-2 (Micheletti et al., 2015). The scene should be static and have consistent lighting, avoiding underexposure and overexposure of photographs. Blurred photographs, high reflective, and glassy surfaces should also be avoided (Micheletti et al., 2015).
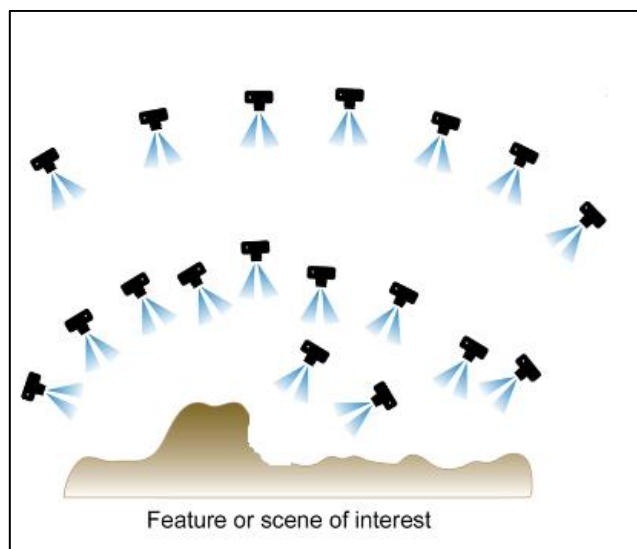
Figure 2-2: Image acquisition for SfM photogrammetry in different directions and positions.

2.2.1.2   Method

2.2.1.2 (a)   The acquisition of images and keypoints

SfM gives a solution to the 3D position of feature matching in several images captured from different angles (Snavely, 2008). The more suitable pictures for calibrating a grid of images are identified; they are then utilized to determine the relative camera orientations (Moulon and Bezzi, 2011). The first step involves the computation of local content; this is performed on each photograph. The second step mainly identifies the nearest descriptor between two images (presumed matches). Lastly, the Epipolar geometry of assumed matches is checked. This concept is called image matching (Moulon and Bezzi, 2011). Figure 2-3 (Moulon and Bezzi, 2011) shows the steps involved in image matching.
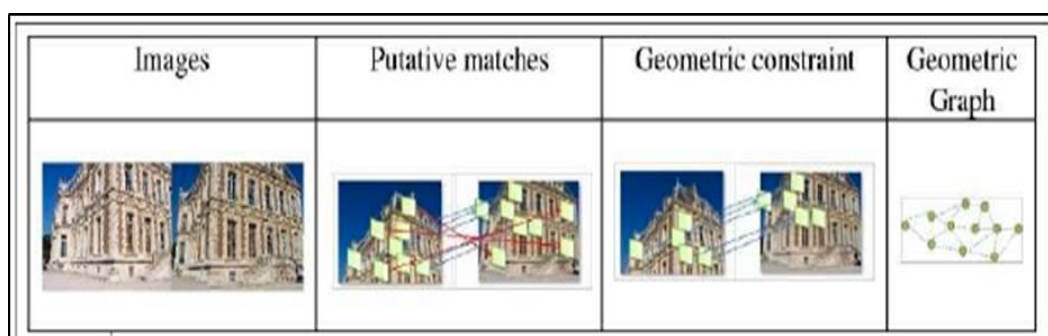
Figure 2-3: Steps involved in image matching.

Before feature descriptors are created, the keypoints are identified automatically and this process covers all positions and scales in each photograph. The uniqueness of the descriptors created enables large datasets of features to be matched (Westoby et al., 2012). The resolution and texture of images determine the number of keypoints that can be computed. The high-resolution images give good results (Westoby et al., 2012). The factors that affect the resulting point cloud quality include the sharpness, density and resolution of the input images. At close range, the spatial resolution of images is increased, resulting in an enhanced point cloud (Westoby et al., 2012).

A wide range of sensors can be employed for SfM, digital cameras, and video stills. If data is acquired in remote areas, considerations should be made about the batteries and weather conditions (extreme temperatures) (Westoby et al., 2012). DSLR cameras with a resolution above 12 megapixels are used to improve the resolution and quality of images. High-resolution images are resized, leading to the loss of some image details (Westoby et al., 2012). The images are acquired after establishing the GNSS target network; they are then enhanced and resized. Executing SIFT (Scale Invariant Feature Transform), SIFT is a feature detector broadly used for multiple tasks, used in the 3D reconstruction. It provides robust features resulting in good camera pose estimations (Berjón et al., 2016). The bundle adjustment follows, producing a sparse point cloud. Clustering Multi-View Stereo (CMVS) and Patch-based Multi-View Stereo (PMVS) are executed, resulting in a dense point cloud (Westoby et al., 2012). The steps involved in SfM are illustrated in the flow chart below (see figure 2-4):
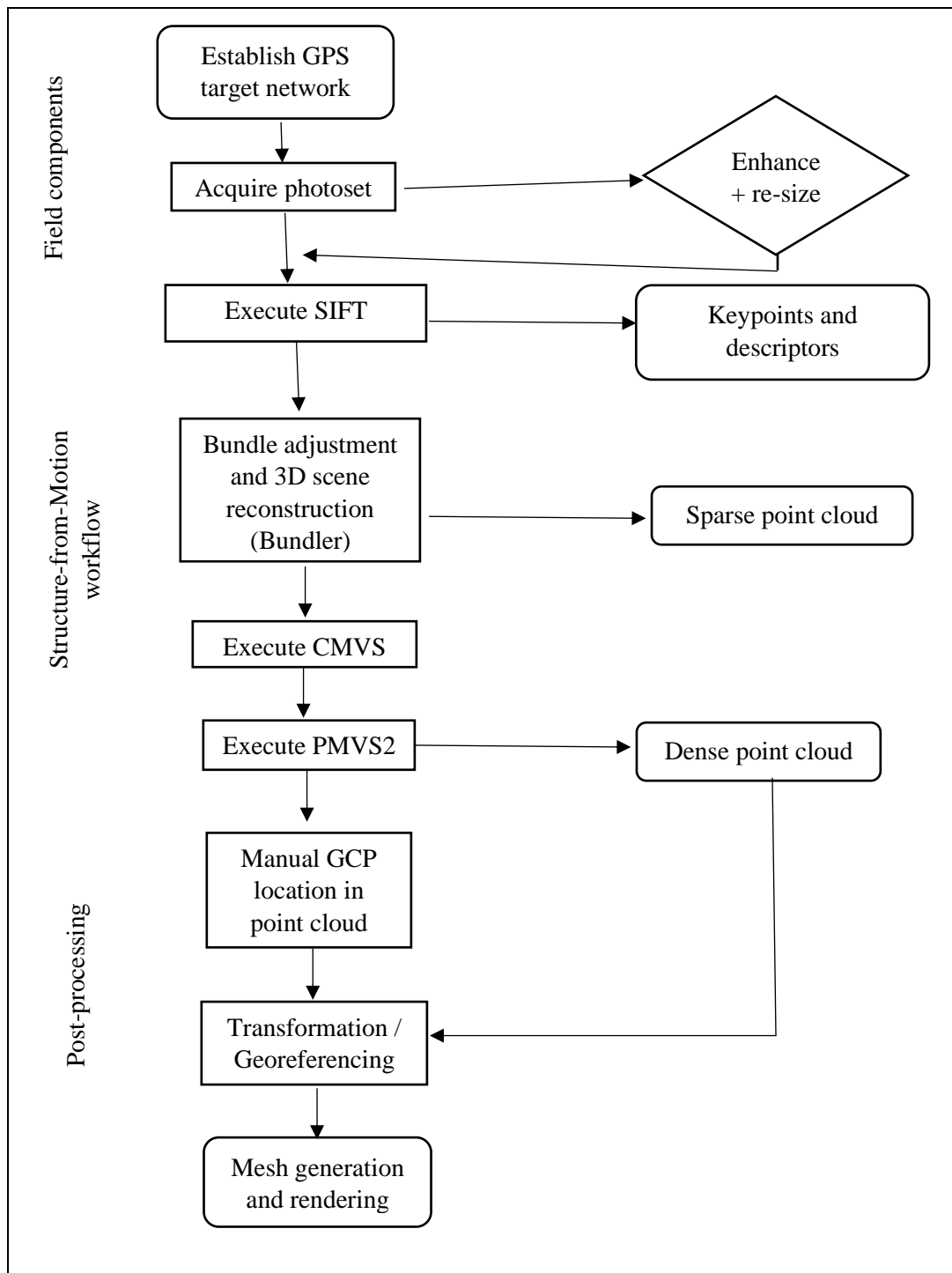
Figure 2-4: The SfM workflow from images to point cloud (Westoby et al., 2012)

2.2.1.2 (b)   Bundle adjustment

Bundle adjustment is generally considered the last stage of the SfM pipeline. Camera poses (exterior orientations) and coordinates of points in 3D are improved in nonlinear optimization (Verykokou and Ioannidis, 2018). The results from SfM are georeferenced by 3D similarity transformation estimates between the object space arbitrary coordinate system and the reference system of the real world through the use of ground control points (Verykokou and Ioannidis, 2018).

In computer vision applications, bundle adjustment is now pre-eminent enabling efficient 3D reconstruction and SfM (Engels et al., 2006). A bundle adjustment study that investigated the repute on a real-time camera tracking system showed that it improves accuracy and eliminates camera tracking failures. The accuracy of bundle adjustment gives the approximations very close to actual values (Engels et al., 2006).

Features identifiable on multiple images may be off-target; these tie points are not triangulated but rejected. Iterative fixed bundle adjustment eliminates all the possible outliers and erroneous tie points using least-squares adjustment. For other images, both exterior and interior orientation parameters are fixed (Verykokou and Ioannidis, 2018). Bundle adjustment is denoted by a mathematical replica in terms of collinearity equations (Verykokou and Ioannidis, 2018). Equations 2.1 and 2.2 (Juea, 2008) represent the collinearity equations. Equation 2.3 (Juea, 2008) is a 3×3 matrix representing the orientation parameters in an implicit form.

$$x - x_0 = -f \frac{a_1(X-X_s)+ b_1(Y-Y_s)+c_1(Z-Z_s)}{a_3(X-X_s)+ b_3(Y-Y_s)+c_3(Z-Z_s)} \qquad \textbf{Equation 2.1}$$

$$y - y_0 = -f \frac{a_2(X-X_s)+ b_2(Y-Y_s)+c_2(Z-Z_s)}{a_3(X-X_s)+ b_3(Y-Y_s)+c_3(Z-Z_s)} \qquad \textbf{Equation 2.2}$$

$$R = \begin{bmatrix} a_1 & a_2 & a_3 \\ b_1 & b_2 & b_3 \\ c_1 & c_2 & c_3 \end{bmatrix} \qquad \textbf{Equation 2.3}$$

Where:

(x and y)	-	Image coordinates
(x_0, y_0, f)	-	Interior orientations
f	-	Focal length of the camera

$(x_0$ and $y_0)$	-	Principal point coordinates
(X, Y, Z)	-	Object space coordinates of the ground points
(D_s, Y_s, Z_s)	-	Object space coordinates of the perspective centres
$(a_1, a_2, a_3, b_1, b_2, b_3, c_1, c_2, c_3)$	-	Elements of the rotation matrix
R	-	Rotation matrix

After determining the interior parameters, the six exterior orientation parameters can be calculated from the collinearity equations. Collinearity equations are linearized, and the Least Square technique is initiated using at least three control points. Good preliminary values are needed for the Least Square approximation in order to converge to accurate values (Juea, 2008).

2.2.1.2 (c)   3D scene reconstruction

A sparse point cloud is generated during bundle adjustment after the recognition of keypoints and assigning descriptors. The approximate nearest neighbor matches keypoints in image pairs (Arya et al., 1998). Objects in motion and momentary features, for example, helicopters and moving people in the scene, are discarded automatically before 3D reconstruction (Snavely et al., 2006).

An approximation of 3D point positions is achieved through triangulation where 3D reconstruction of the scene is anchored in a comparative coordinate system; this process is fully automated (Westoby et al., 2012). The density of the point cloud is enhanced by executing the CMVS (Clustering Multi-View Stereo) and PMVS2 (Patch-based Multi-View Stereo). The camera positions determined during bundle adjustment serve as input (Westoby et al., 2012).

CMVS removes images of low quality and performs clustering of images into tiny elements through the Normalized Cuts technique. Images are added to infirm clusters resulting in a dense cluster (Westoby et al., 2012). Numerous metric constraints examined in photogrammetric network designs are disregarded because CMVS was developed for an extensive collection of images. Using the Blunder output, PMVS is responsible for creating a dense point cloud model (Mahami et al., 2019). The orientation parameters of undistorted images and projection matrices are used to enhance a sparse point cloud, resulting in a collection of rectangular patches that are accurate and dense (Mahami et al., 2019).

2.2.1.2 (d)   DTM generation and post-processing

Ground control points (GCPs) are not necessarily needed for the SfM technique. The 3D visualization is the part of interest employed in many different applications. Bringing together point clouds produced by a scanner and SfM results in a robust geomorphological analysis tool (Westoby et al., 2012). The use of GCPs is essential if the model requires to be transformed into the absolute coordinate system from a relative system. GCPs are identified manually from images; these points need to be visible on the actual ground and images (Westoby et al., 2012).

2.3 Image Classification

Image classification is explained as an operation of allocating pixels to groups, creating thematic maps from imagery. Grouping pixels of similar identity is achieved by comparing pixels to one another and known values based on classes relevant to the operator (Turner et al., 2001). Different classes may occur, for example, vegetation, soil and water bodies. The description can be more detailed and have different soil types, water depth and vegetation (Schowengerdt, 2007).

The classification of remotely sensed data has been a challenge to date. Many contributing factors include the convolution of the topography in a study area, selection of data, methods utilized for image-processing and classification (Lu and Weng, 2007). The significance of image classification applies to various fields, including video surveillance, visual inspection in industries, vehicle navigation, remote sensing and robot navigation (Gevaert et al., 2016).

Scientists have invented numerous classification techniques throughout the years. A classification strategy must be selected by the analyst, depending on the objectives of a specific task (Campbell, 2002). Figure 2-5 (Singh, 2013) shows the steps of image classification.
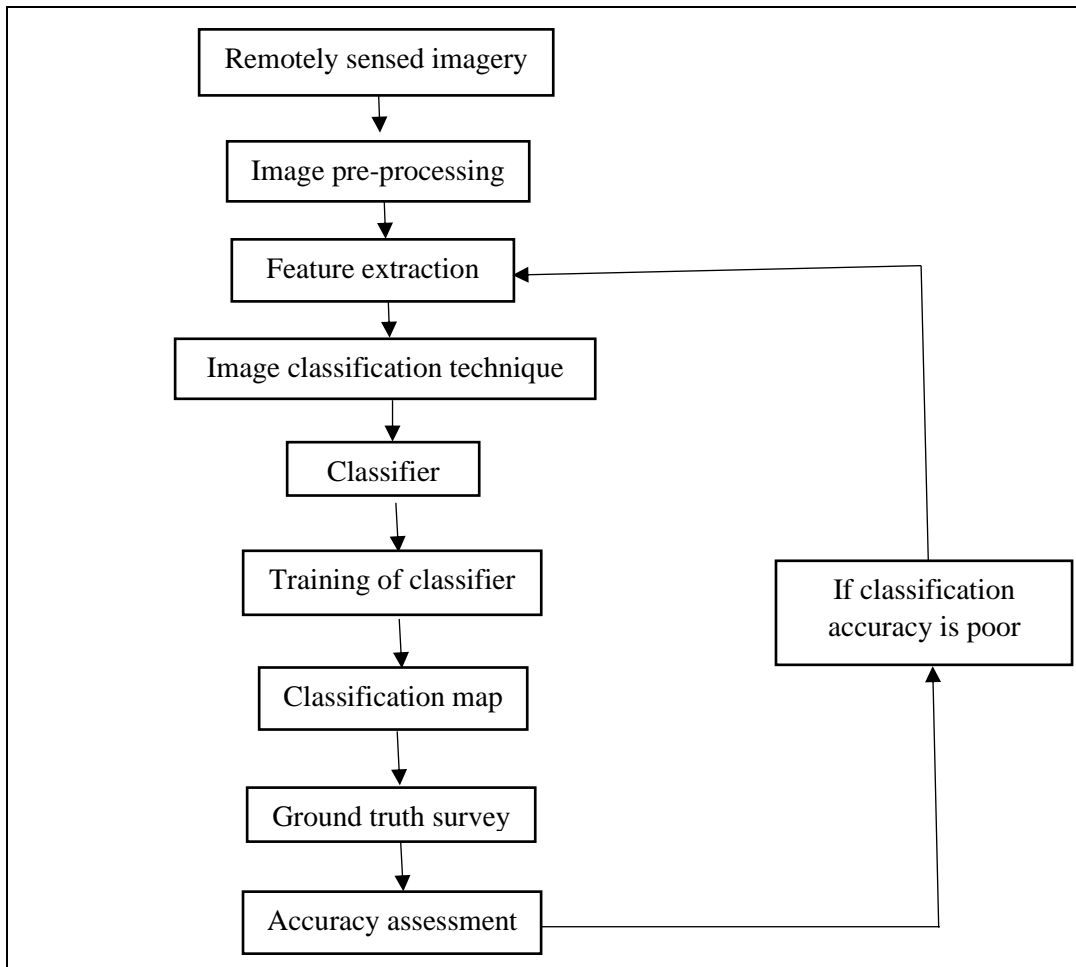
Figure 2-5: Steps involved in image classification.

2.3.1 Image Classification Procedures

2.3.1.1 Remotely Sensed Imagery

Remotely sensed data can be acquired using spaceborne and airborne sensors. These data differ in terms of resolution, spectral, spatial, temporal, and radiometric resolutions. It is requisite to apprehend the capabilities of different kinds of sensor data, the strengths and incapacities towards the classification of images (Lu and Weng, 2007).

Various factors should be considered when selecting remotely sensed data. These factors include the scale, properties of the area of study and the images, the user's need, cost and time limitations. However, the analyst's experience of working with selected remotely sensed data is the most critical factor towards successful classification (Lu and Weng, 2007; Quattrochi and Goodchild, 1997).

2.3.1.2 Image Pre-processing

The preliminary step performed before the actual processing of remotely sensed data. Preprocessing images may comprise topographic and atmospheric corrections, repairing bad lines, image registration, or geometric correction (Lu and Weng, 2007). Geometric preprocessing establishes the relationship between the image and a map or another georeferenced image (Campbell, 2002).

Since images are acquired by remote sensing, there is a need to perform atmospheric correction if the training data is to be applied to a different image. Atmospheric correction is not crucial when a single-date image is classified. The other method is to normalize the second image to the first one (Schowengerdt, 2007).

Image preprocessing's primary purpose is to improve images' quality; valuable information is extracted from images for evaluation (Campbell, 2002).

2.3.1.3 Feature Extraction

The statistical image characteristics are obtained in feature extraction, the band values containing statistics about the site. Thus, feature extraction minimizes the number of bands used for analysis, which is less computational. This may have a positive effect on improving accuracy (Campbell, 2002).

A crucial step when performing image classification is determining appropriate variables. Employing various variables in the classification process may have a negative effect reducing accuracy (Lu and Weng, 2007; Price et al., 2002).

2.3.1.4 Training of Classifier

For an image to be classified into different categories, training the classification algorithm must be performed to identify those categories. The classifiers following the rules established during training identify the samples from the training process. All the image pixels are labeled into different categories (Campbell, 2002).

Remote sensing imagery can be clustered using supervised and unsupervised classification algorithms, which is part of machine learning. Machine learning gives results from given input data. The computer learns from a set of indicative samples (Canty, 2014).

2.3.2   Image Classification Techniques

A wide range of classifier categories exists. Some approaches are briefly explained especially the supervised classification techniques. The categories include object-oriented, hard and soft classification, spectral and contextual classifiers, per-pixel and subpixel classifiers, parametric and non-parametric classifiers (Campbell, 2002).

2.3.2.1 Supervised Classification

The analyst determines sample pixels for each category. Homogeneous training are samples of great significance, but simultaneously a variation in range for the class has to be included; this results in multiple training areas (Schowengerdt, 2007). The location, form, and magnitude should be such that favorable recognition is achieved on the ground and the image. The advantages of supervised classification include the analyst being in full control of classification categories. There is preliminary information, and no spectral classes are to be matched towards producing a map. The errors in classification may be detected (Campbell, 2002).

The disadvantages of supervised classification include the data used for training may not be good enough to accommodate all the conditions in every part of the image. This method fails to identify categories not present on training data, and it consumes much time (Campbell, 2002).

2.3.2.1 (a)   Artificial Neural Network

Artificial Neural Network (ANN) is defined as artificial intelligence that emulates some human-mind tasks. ANN tends to save experimental knowledge. This technique comprises a succession of layers, of which each has a series of neurons. Weighted connections link all the neurons in layers in such a manner that the succeeding and preceding layers are connected (Campbell, 2002; Kamavisdar et al., 2013).

The ANN utilizes a Non-parametric approach. The number of inputs and the structure of the networks determines the accuracy and performance of this technique (Kamavisdar et al., 2013). The advantages of ANN include a high computation rate, handles noisy inputs efficiently, supports Boolean functions (OR, AND, NOT). It is also a global functional estimator with arbitrary accuracy. The disadvantages of ANN include more time required during training, semantically inadequate, and complicated in deciding the type of network architecture (Kamavisdar et al., 2013).

2.3.2.1 (b)   Maximum Likelihood

The decision rule for maximum likelihood is a chance that a pixel is part of a particular class (Pouncey et al., 1999). Training data is used to approximate variances and averages per class; this is used in determining the likelihood of belonging (Campbell, 2002). Equation 2.3 (Erdas field guide, 2010) is used for maximum likelihood calculation.

$$D = \ln(a_c) - [0.5 \ln(|Cov_c|)] - \left[0.5(X - M_c)^T (Cov_c^{-1})(X - M_c)\right]$$ **Equation 2.3**

Where:

D	- Weighted distance
c	- Certain class
X	- Measurement vector of the candidate pixel
M_c	- Mean vector of the sample of class c
A_c	- Probability that any candidate pixel is a member of class c
Cov_c	- Covariance matrix of the pixels in the sample of class c
$|Cov_c|$	- Determinant of Cov_c
Cov_c^{-1}	- Inverse of Cov_c
ln	- Natural logarithm function
T	- Transposition function

2.3.2.1 (c)   Minimum Distance

The decision rule for minimum distance calculates the spectral separation joining the measurement vector for the pixel and the mean vector per signature (Campbell and Wynne, 2011; Pouncey et al., 1999).

The minimum distance decision rule is quick and all pixels are classified. The downside of minimum distance is that variability of a class is not contemplated. It results in the inappropriate classification of outlying pixels (Pouncey et al., 1999).

2.3.2.1 (d)   Parallelepiped Classification

The decision rule is based on the training data range. The lower and upper pixel is used to establish whether the candidate pixel falls within the range then allocated to appropriate categories (Pouncey et al., 1999).

The standard deviations of training data can be used to determine the decision boundaries instead of using ranges. Thus, fewer pixels are not classified; also, the chances of class overlap increase (Campbell and Wynne, 2011). Parallelepiped classification is fast, accurate and straightforward, but features near the boundary remain ambiguous in class belonging (Campbell and Wynne, 2011).

2.3.2.1 (e)   Decision Trees

For the Decision tree to determine class belonging, a dataset is repeatedly partitioned into homogeneous subsets. Class labels are accepted and rejected by the hierarchical classifier at each mediator stage (Kamavisdar et al., 2013). A decision tree comprises three sections: Partitioning the nodes, detecting end nodes, and assigning group labels to the end node. Like ANN, the Decision tree uses a Non-parametric approach (Kamavisdar et al., 2013).

The advantages of a Decision tree include simplicity and superb computational efficiency, non-parametric training data can be handled, no large training and design data are required. On the other hand, decision trees' disadvantages include compound calculation when dealing with many undecided values and correlated outcomes (Kamavisdar et al., 2013).

2.3.2.1 (f)   Support Vector Machine

Support Vector Machine (SVM) is applied in diverse types of data such as Landsat multispectral data. SVM is a non-parametric classifier that recognizes and separates classes; this is achieved by the establishment of boundaries in the feature extent and enlarging the lines between the classes (Keuchel et al., 2003). SVM creates a hyperplane or a group of hyperplanes in a high-dimensional space for categorizing classes. If the margin is large, the generalization error is reduced for the classifier (Al-Doski et al., 2013).

SVM is a Non-parametric classifier that uses a binary approach. As a result, high-volume input data can be handled more efficiently. The kernel parameter and the hyperplane selection determine the accuracy and performance (Kamavisdar et al., 2013). The advantages of SVM include easy control of error frequency and decision rule, the lowered computational complexity. SVM completely removes the issue of overfitting. It also accommodates a non-linear transformation (Kamavisdar et al., 2013). The downside of SVM is that it takes much more time for classifier training. It is not easy to apprehend the algorithm's structure, and the clarity of results is low (Kamavisdar et al., 2013).

2.3.2.2 Unsupervised Classification

Unsupervised classification identifies natural categories or shapes within multispectral data (Campbell, 2002). A massive number of pixels, all whose values are unknown, are analyzed and grouped into different classes following the values found on images. No prior information is needed for unsupervised classification. The computer deduces the information of spectrally distinguishable classes, thus reducing the chance of human error (Campbell, 2002; Kamavisdar et al., 2013).

The limitation of unsupervised classification is that the analyst is not in full control of the classes used. In addition, classification is distributed across the entire image, including the parts not relevant to the analyst (Campbell, 2002). Examples are the K-means clustering algorithm and ISODATA (Kamavisdar et al., 2013).

2.3.2.2 (a)   Fuzzy Measure

The properties of the image are detailed using stochastic associations. The fuzzy integral and threshold designation determines the accuracy and performance (Kamavisdar et al., 2013). Fuzzy classification can be applied to both classification techniques, unsupervised and supervised (Venkateswaran et al., 2013).

The advantages of fuzzy classification include the ability to handle uncertainties more efficiently. The image characteristics are detailed by distinguishing different stochastic relationships. The downside of fuzzy classification is that the results are not satisfactory if no prior information was available (Kamavisdar et al., 2013).

2.3.3   Accuracy Assessment

The accuracy assessment problem is explained as a comparison between two maps from different sources. The first map is to be examined and the second map acts as a reference map based on the assumption that it is error-free (Campbell, 2002). The analyst should know the sources of error prior to performing the assessment of classification accuracy. Examples of errors affecting accuracy include interpretation errors, position errors and inferior test samples (Campbell and Wynne, 2011; Lu and Weng, 2007).

2.3.3.1 Error Matrix

The error matrix is one of the methods employed in classification accuracy assessment (Lu and Weng, 2007). In order to assess accuracy, a comparison between classified images and ground truth (reference data) is performed. The error matrix is sometimes referred to as a confusion matrix, comprising reference and classified data in columns and rows, respectively (Campbell and Wynne, 2011; Story and Congalton, 1986).

The overall accuracy, producer's accuracy, and user's accuracy are computed from the confusion matrix (Story and Congalton, 1986). Some elements of accuracy assessment are obtained from the error matrix, such as omission and commission errors and kappa coefficient (Lu & Weng, 2007; Congalton et al., 2002). The overall accuracy refers to the correctness of the entire product determined by the ratio of correct classifications to the sum of samples (Lillesand et al., 2015; Story and Congalton, 1986). The producer's accuracy is the ratio of correct classifications to the sum of reference data from the same sample. It relates to the error of omission (EO) (Story and Congalton, 1986). The user's accuracy is the correct classification ratio to the sum of classified data of the same kind. The user's accuracy relates to the error of commission (EC) (Campbell and Wynne, 2011; Story and Congalton, 1986). Modified Table 2-1 and Table 2-2 from Story and Congalton (1986) show how the error matrix is determined.

Table 2-1: Confusion matrix

| | | Reference | | | |
		A	B	C	Sum
Classified Data	A	28	14	15	57
	B	1	15	5	21
	C	1	1	20	22
	Sum	30	30	40	100

Table 2-2: Accuracy Calculations

Sum of the major diagonal = 63 Overall Accuracy (OA) = $\frac{63}{100}$ = 63%	Producer's Accuracy (PA) A = $\frac{28}{30}$ = 93% B = $\frac{15}{30}$ = 50% C = $\frac{20}{40}$ = 50%	User's Accuracy (UA) A = $\frac{28}{57}$ = 49% B = $\frac{15}{21}$ = 71% C = $\frac{20}{22}$ = 91%

Errors of commission take place when a pixel is allocated to a land cover category that is not true on the ground. Inversely, the errors of omission occur when a pixel is not allocated to a particular land cover category on the ground (Campbell and Wynne, 2011; Lillesand et al., 2015).

2.3.3.2 Kappa Coefficient

The Kappa statistic is defined as a technique used to examine interrater reliability (Viera and Garrett, 2005). The Kappa is derived from the proportion agreement that is observed and the chance agreement (Uebersax, 1982). The Kappa coefficient shows the proportional error reduction from classification in contrast with random classification error (Pouncey et al., 1999).

Contrast is made between the true agreement between computerized classifier and reference information and the possible arrangement between random classifier and reference information (Lillesand et al., 2015). Equation 2.4 (Lillesand et al., 2015) is used to determine the Kappa statistic.

$$\hat{k} = \frac{observed\ accuracy - chance\ agreement}{1 - chance\ agreement}$$ **Equation 2.4**

Table 2-3, extracted from table 2 of Viera and Garrett (2005) shows the Kappa value ratings and their interpretation.

Table 2-3: Interpretation of Kappa

	Poor	Slight	Fair	Moderate	Substantial	Almost perfect
Kappa	< 0	$0.01 - 0.20$	$0.21 - 0.40$	$0.41 - 0.60$	$0.61 - 0.80$	$0.81 - 0.99$

The Kappa takes the possibility of guessing into consideration, but it may result in underestimation when it comes to classification accuracy (McHugh, 2012).

2.4   LiDAR Classification

2.4.1   Introduction

In our lives, LiDAR technology is present more than we notice (GIM, 2019). The use of Light Detection and Ranging (LiDAR) is growing in multiple applications and disciplines, producing spatial point cloud data with high resolution (Antonarakis et al., 2008). Precise information, both horizontal and vertical, can be obtained with ±30cm nominal accuracy. Digital terrain models and digital surface models are examples of replicas that can be generated from LiDAR (Brennan and Webster, 2006). In addition, LiDAR technology is cost-effective; it can simultaneously compute intensity data and position for the same area (Song et al., 2002).

The feature vector containing 21 elements represents airborne LiDAR features: 4 full-waveform and 17 multi-echo LiDAR features. Multi-echo features are categorized based on height, echo, local 3D-plane, and eigenvalue (Chehata et al., 2009). Multiple classifiers have been used in LiDAR data, modifying datasets and applying them in the training process (Chehata et al., 2009). While having the unstable base classifier, the minor changes result in massive changes in the classifier results. The most commonly used unstable classifiers include Decision Trees and Neural Networks (Briem et al., 2002).

2.4.2   Random Forests

Random Forests (RF) is a group-based classifier that uses a decision tree approach and produces excellent classification results compared to Support Vector machines (SVMs) (Breiman, 2001). Random Forests are non-parametric, and there are no presumptions required on the data distribution enabling the use of various input attribute scales (Breiman, 2001; Chehata et al., 2009).

Random Forests supports large datasets and can manage input variables without deletion. Every single tree for the most favored class gives a unit vote. They run effectively, providing correct classification (Chehata et al., 2009).

Chehata et al. (2009) studied various LiDAR features, Full-waveform (FW) and multi-echo, to perform urban scene classification into four groups: Vegetation, buildings, artificial and natural ground. Random Forests were used as a classifier, producing good classification results; an overall accuracy of 94.35% was achieved using selected variables.

2.4.3   Previous Research on LiDAR Classification

2.4.3.1 Assessing the Possibility of Land-Cover Classification

Song et al. (2002) conducted a study on a land-cover classification that evaluated LiDAR data intensity's compatibility. Four classes were used to evaluate intensity data separability: asphalt road, house roof, tree, and grass. It was deduced that LiDAR is cost-effective, accurate, and LiDAR intensity can be applied in land-cover classification (Song et al., 2002).

2.4.3.2 Object-based Land Cover Classification

Antonarakis et al. (2008) used airborne LiDAR, the intensity and elevation data to classify ground types and forests (planted and natural) employing a supervised approach. The software packages used include ArcGIS, C++ programming and MATLAB. The digital aerial photographs used to assess the classification accuracy were taken on the same day as the airborne LiDAR data (Antonarakis et al., 2008).

Equation 2.5 (Antonarakis et al., 2008) gives the overall classification accuracy:

$$AI(\%) = \left[\frac{(n-(O+C))}{n} \right] \times 100 \qquad\qquad \textbf{Equation 2.5}$$

Where:

AI	- Accuracy index
O	- Omission errors
C	- Commission errors
n	- Sum of trees to be detected in the image

Land types were classified successfully with 95% and 94% accuracy from three sites using bimodal and unimodal distribution skewness and kurtosis models, respectively (Antonarakis et al., 2008). The limitations of this study included missing values in lidar return which could give unrealistic height information.

Brennan and Webster (2006) classified land cover types into ten classes using segmentation and rule-based approach. Then, the GIS was used for digitizing polygons of ground reference data obtained from LiDAR intensity images and orthophotographs. The average accuracy of 94% was achieved; it was increased to 98% after clustering the classification results into seven classes (Brennan and Webster, 2006).

2.5 Aerial Photography Classification

The segmentation and classification of aerial photography features have been widely used, producing more detailed models on a human scale (Nguyen et al., 2010). In aerial photography, an airborne sensor is used to acquire the collection of photographs (Wolf et al., 2014). These photographs may be oblique or vertical, depending on their application (Morgan et al., 2010). Utilizing products generated from aerial photography is cost-effective. Numerous management decisions that encompass planning and mapping rely on aerial photography (Morgan et al., 2010).

5.2.1 Methods for Aerial Photography Analysis

The new image enhancement and classification automated approaches are applicable to aerial photographs and hold the potential of addressing some issues associated with traditional photo interpretation (Morgan et al., 2010). The automated digital techniques enable a separate and explicit analysis of photograph characteristics ((Morgan et al., 2010). A summary of the advantages and disadvantages of classification techniques employed in aerial photography is presented in Table 2-4.

Table 2-4: Comparative advantages and disadvantages of aerial photography classification techniques (modified from Table 5 of Morgan et al. (2010)).

Type	Advantage	Disadvantage
• **Manual interpretation**	• Fairly accurate • Less image preparation needed • Comprehensive, human knowledge is utilized in making logical decisions • Used in resource management map creation	• Consumes more time • Subjective and expensive • Scarcity of well-trained interpreters • Inconsistent among interpreters • The standards of accuracy vary widely
• **Pixel-based classifiers**	• Systematic, consistent • Repeatable • Well-developed accuracy assessment methods, sufficient software available	• Mainly use spectral information • Arbitrary analysis units (pixels) • Not suitable for high spatial resolution imagery analysis
• **Object-based classifiers**	• Systematic, consistent • Repeatable • Accommodates multiple scales and integrate attributes (shape, tone, texture, size, context)	• Software expensive • Difficult object creation • Less developed accuracy assessment procedures • Suitable for high spatial resolution imagery

2.5.2 Pixel-based Classification

Over the years, the automated classification of buildings has been a challenge (Nguyen et al., 2010). A stacked graphical model (SGM) ensemble is employed as an approach proposed by Nguyen et al. (2010), which integrates different features such as texture, color, and 3D information in an attempt to improve the extraction of buildings from aerial images. A randomized forest that comprises decision trees was utilized as a base classifier since it provides accurate image classification activities that are challenging (Shotton et al., 2008).

The comparison was made between SVM, RF, Staked RF model and SGM model. The SGM was applied with success in the classification of building and non-building classes. Classification accuracies above 91% were obtained from 3 datasets that were used. Among all classification models, the SGM produced the best results. Nguyen et al. (2010) concluded that this model is applicable in learning 3D objects such as buildings and other object classes.

The availability of reference data and its quality should be considered prior to commence the accuracy assessment task, classification and positional accuracy are evaluated (Paine and Kiser, 2003). Classification accuracy is based on assigning labels to classes, while positional accuracy has to do with feature location and boundaries (Morgan et al., 2010; Thompson et al., 2007). Comparison is made between the classified photograph and reference information from thematic data sets or field data (Foody, 2002; Morgan et al., 2010).

2.6   3D Point Cloud Classification

The automatic categorization of point cloud information is essential and challenging at the same time (Roynard et al., 2018). State of the art includes shallow and deep-learning techniques for classifying 3D point clouds (Roynard et al., 2018).

A great diversity of work has been undertaken on classifying scenes of 3D point clouds without learning or by shallow learning (Roynard et al., 2018). It is achieved by implementing two approaches: the first approach is based on classifying each point and grouping points into objects, whereas the second approach segments the point cloud into objects and then classifies each object. Following the first approach, Weinmann et al. (2015) classified points by determining simple descriptors, being the neighborhood dimensionality attributes. In the second approach, the global descriptors are computed after segmentation. These can be geometrical descriptors, histograms of normal distribution curves, and shape functions. (Roynard et al., 2018).

2.6.1   Deep-Learning for Classification of 3D Point Clouds

Classifying 3D point clouds using deep learning methods has been growing over the past years (Roynard et al., 2018). The new network architectures on point cloud and voxel grids, resulting from the research teams of ShapeNet Core55 challenge, have beaten state-of-the-art 3D reconstruction from single view image and part-level segmentation of 3D shapes (Yi et al., 2017).

Deep-learning on 2D views of the cloud includes projections including but not limited to elevation maps, depth-map, panorama image, RGB image, and range image (Roynard et al., 2018). Capturing multiple views of the particular scene or object and integrating the results can enhance these methods (Boulch et al., 2017). On the voxel grid, 3D point clouds are classified. An object instance is transformed by occupying a density grid; a Convolutional Neural Network (CNN) is then applied (Huang and You, 2016). Huang and You (2016) classified clouds of urban scenes. The class belonging was predicted by the network from its neighborhood's density grid (Huang and You, 2016). A few methods import point clouds as input; this has the advantage of operating clouds very close to the level of raw data (Roynard et al., 2018).

Roynard et al. (2018) proposed a method of training in each class, balancing the number of points during each period and a multi-scale CNN that has the ability to learn classifying point cloud scenes. Equations 2.6 - 2.10 (Nevalainen et al., 2017; Roynard et al., 2018) present the metrics utilized in performance evaluation. This was achieved by comparing two architectures (balancing the number of points and CNN) on three selected datasets, namely Paris-Lille-3D, Semantic3D, and S3DIS (Roynard et al., 2018).

$$P_c = \frac{TP_c}{TP_c + FP_c}$$

Equation 2.6

$$R_c = \frac{TP_c}{TP_c + FN_c}$$

Equation 2.7

$$F1_c = \frac{2TP_c}{2TP_c + FP_c + FN_c} = 2\frac{P_c R_c}{P_c + R_c}$$

Equation 2.8

$$Acc_c = \frac{TP_c}{TP_c + FN_c}$$

Equation 2.9

$$IoU_c = \frac{TP_c}{TP_c + FP_c + FN_c}$$

Equation 2.10

Where:

P_c	- Precision of class c
R_c	- Recall of class c
$F1_c$	- F1-score of class c
Acc_c	- Accuracy of class c
IoU_c	- Intersection-over-Union score of class c
TP_c	- True-Positives in class c
TN_c	- True-Negatives in class c

FP$_c$ - False-Positives in class c

FN$_c$ - False-Negatives in class c

2.6.2   Gradient Boosted Trees

Gradient Boosted Trees (GBT) is a supervised classification method that operates by training an ensemble of trees by reducing in an acquisitive way its loss over training data (Friedman et al., 2001). The GBT and RF methods are similar in a manner that they are both capable of generating conditional probabilities and can be applied in multi-class problems (Becker et al., 2017).

Becker et al. (2017) presented a robust method that integrates color and geometric features to estimate each point's class belonging in the cloud. The colour features were computed based on the neighboring points. It was deduced that the incorporation of color information increases the accuracy of classification at different dataset ranges. Additionally, this method has high computational efficiency (Becker et al., 2017).

2.6.2   Conditional Random Fields

Conditional Random Fields (CRF) uses a non-linear decision surface to accurately isolate the object groups in feature space (Niemeyer et al., 2012). CRF can learn and model the interface of all object classes without initial segmentation and offer a great probabilistic framework for contextual classification (Niemeyer et al., 2012). CRFs are categorized under undirected graphical models, represented by the $G(\boldsymbol{n}, \boldsymbol{e})$ graph comprising of nodes **n** and edges **e** (Niemeyer et al., 2012).

Niemeyer et al. (2012) introduced and evaluated a context-based CRF classifier. 3D urban scenes were classified and evaluated in accordance with the 'ISPRS Test Project on Urban Classification and 3D Reconstruction'. Lidar data was used to train five classes: natural and asphalt ground, building, trees, and low vegetation. The classification results were promising but improved OA after enhancement by 5.38%. It was concluded that the CRFs show a high potential in classifying urban scenes (Niemeyer et al., 2012).

2.6.3   Tree Crown Classification

A study based on big point cloud data classification using the Cloud Computing method presented by Liu and Boehm (2015) uses Apache Spark as a cluster computing framework, yielding optimistic outcomes that may give solutions to the processing of large datasets of

point clouds. This study is based on specifying whether a point cloud exists in a tree crown. The classification algorithm followed a supervised learning problem and was approached by feature computation, training of a model, and prediction. (Liu and Boehm, 2015)

The experiments conducted had point clouds with 3 million points each. Figure 2-6 (Liu and Boehm, 2015) shows the classification outcomes with tree crown points identified, among other features at the scene.
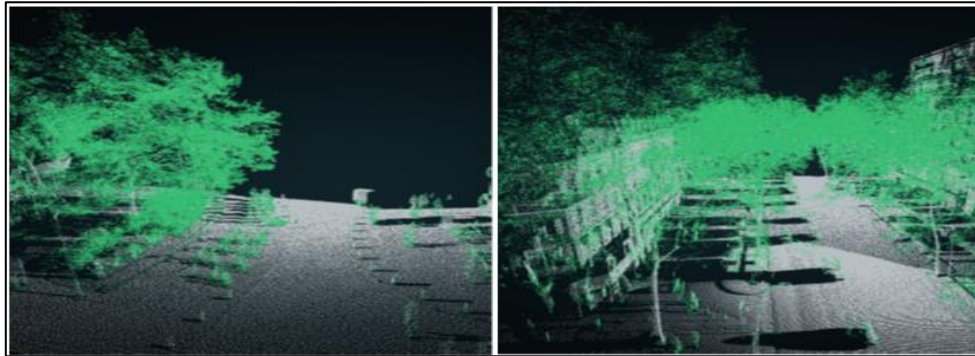
Figure 2-6: Visualized point cloud results.

2.6.4   Multi-scale Dimensionality Classification

Brodu and Lague (2012) proposed a classification method that utilizes the dimensionality of points at multiple scales to accomplish a high classification level for complex natural environments. This classification algorithm was implemented in the CloudCompare software as CANUPO. Signatures that recognize classes present in the scene are constructed using knowledge from different scales. These signatures through the training point are automatically generated, enabling optimization of class separability. The algorithm presented by Brodu and Lague (2012) aimed to recognize features, including scenes that were not part of the training samples. In simple terms, the classifiers should work in unknown scenes. The classification result gives probabilistic confidence at each point enabling the operator to remove suspicious points with uncertainty. The multi-scale dimensionality criterion was used in classifying vegetation and ground, yielding an accuracy above 98% (Brodu and Lague, 2012).

The balanced accuracy measure quantifies the classifier performance, considering the number of points present in each class. Equation 2.11 (Brodu and Lague, 2012) is used to determine the balanced accuracy. Equations 2.12 and 2.13 (Brodu and Lague, 2012) define the two classes' accuracy.

$$ba = \frac{1}{2}(a_v + a_g)$$ **Equation 2.11**

$$a_v = \frac{t_v}{t_v + f_g}$$ **Equation 2.12**

$$a_g = \frac{t_g}{t_g + f_v}$$ **Equation 2.13**

Where:

ba	- Balanced accuracy
a_v	- Accuracy of vegetation
a_g	- Accuracy of ground
t_v	- Number of points truly classified as vegetation
t_g	- Number of points truly classified as ground
f_v	- Number of points falsely classified as vegetation
f_g	- Number of points falsely classified as ground

$$fdr = \frac{(\mu_2 - \mu_1)^2}{(v_1 - v_2)}$$ **Equation 2.14**

The Fisher Discriminant Ratio (fdr) was used to evaluate the separability of classes. In equation 2.14 above, μ_c and v_c represent the average and variance of d of the signed distance to the separation line (Theodoridis and Koutroumbas, 2009). The ba measure and the fdr play a vital role in assessing the classifier and the final classification (Brodu and Lague, 2012). A large value of ba denotes a good recognition measure. Likewise, well-separated classes are denoted by a high value of fdr (Brodu and Lague, 2012).

Grilli et al. (2017) analysed popular algorithms and techniques for 3D point cloud classification; the CANUPO classification was used to filter stones and vegetation in the archaeological site successfully. The CANUPO classification was also used by Farella (2016) to automatically separate artificial and natural structures for mapping 3D underground environments. Another study conducted by Bonneau and Hutchnison (2019) aimed to identify and interpret the geomorphological processes taking place at a cliff. The separation of vegetation and granular material above the cliff was successful.

2.7   Applications

2.7.1   Cultural Heritage Field

Segmentation and classification can apply to architectural documentation and preservation of historical buildings (Grilli et al., 2017); this can be implemented at various scales ranging from small-scale artifacts to large archaeological sites (Grilli et al., 2017). It plays an essential role in the restoration of historical buildings (Reinoso et al., 2014).

2.7.2   Monitoring

The applications are potentially endless; classifying objects has a powerful role in diverse disciplines (De Morsier et al., 2019). Table 2-5 displays applications of AI-powered object detection and automated platform offered by Picterra (Picterra, 2019).

Table 2-5: Application of Object Detection

Field	Description
Farming	• Farmers are interested in knowing if their plants are underproductive. • In case floods occurred, ranchers need to know about the survival of their cattle.
Insurance companies	• In an event whereby a storm occurs, insurance companies can determine the number of roofs that were damaged.
Electricity companies	• Electricity companies can determine the number of solar panels present in the city.
Oil companies	• Oil companies can detect oil spills
Water companies	• Water companies can find out the number of manhole covers missing. • This information can be utilized for maintenance and planning for the expansion of the network.

2.8   Summary

Point clouds were introduced, including the Structure-from-Motion photogrammetry, which is a proposed method for this research. Classification from different sources of data is discussed in this chapter: Image classification, Lidar, and three-dimensional point cloud classification. The techniques and approaches used in the classification of different formats are more or less similar, supervised and unsupervised, being the two major categories. Lastly, the applications and methods used for accuracy assessment were discussed in this chapter.

CHAPTER 3

STUDY AREA

3.1 Introduction

The University of KwaZulu-Natal (Howard College Campus) sports field was selected as the study area for this research. It is situated in Glenwood with a GPS waypoint of 29°52'16" S, 30°59'03" E on Google Earth. This study area was selected based on its location within the university Erf 12494 Durban (CSG, 2001). This area was accessible with no extra costs required for travel. It also comprises different features, both natural and man-made objects. These are land cover categories to be classified in a point cloud format.

It comprises a water body, sparse and dense vegetation, buildings and road surface. The environment poses no hazardous effects to instruments used for data acquisition and the operator of the instruments.

3.2 The University of KwaZulu-Natal

The proposed area of study is shown in figure 3-1. This satellite image was taken from Google Earth Pro. Figure 3-1 is also referred to as the testing site.

Figure 3-1: Study area

Another study area was identified to be utilized as the training site. This area is also situated at the University of KwaZulu-Natal (Howard College Campus) with a GPS waypoint of 29°51'58" S, 30°58'22" E on Google Earth. Using the criterion employed to identify the area in figure 3-1, another sports field, Erf 471 Cato Manor, was selected. Figure 3-2 shows the training site captured from Google Earth Pro.

Figure 3-2: Training site

A layout plan showing the boundaries of the training and the testing site was produced using the ESRI GIS software, ArcMap. Figure 3-3 shows the geographical location of the sites within the University of KwaZulu-Natal.
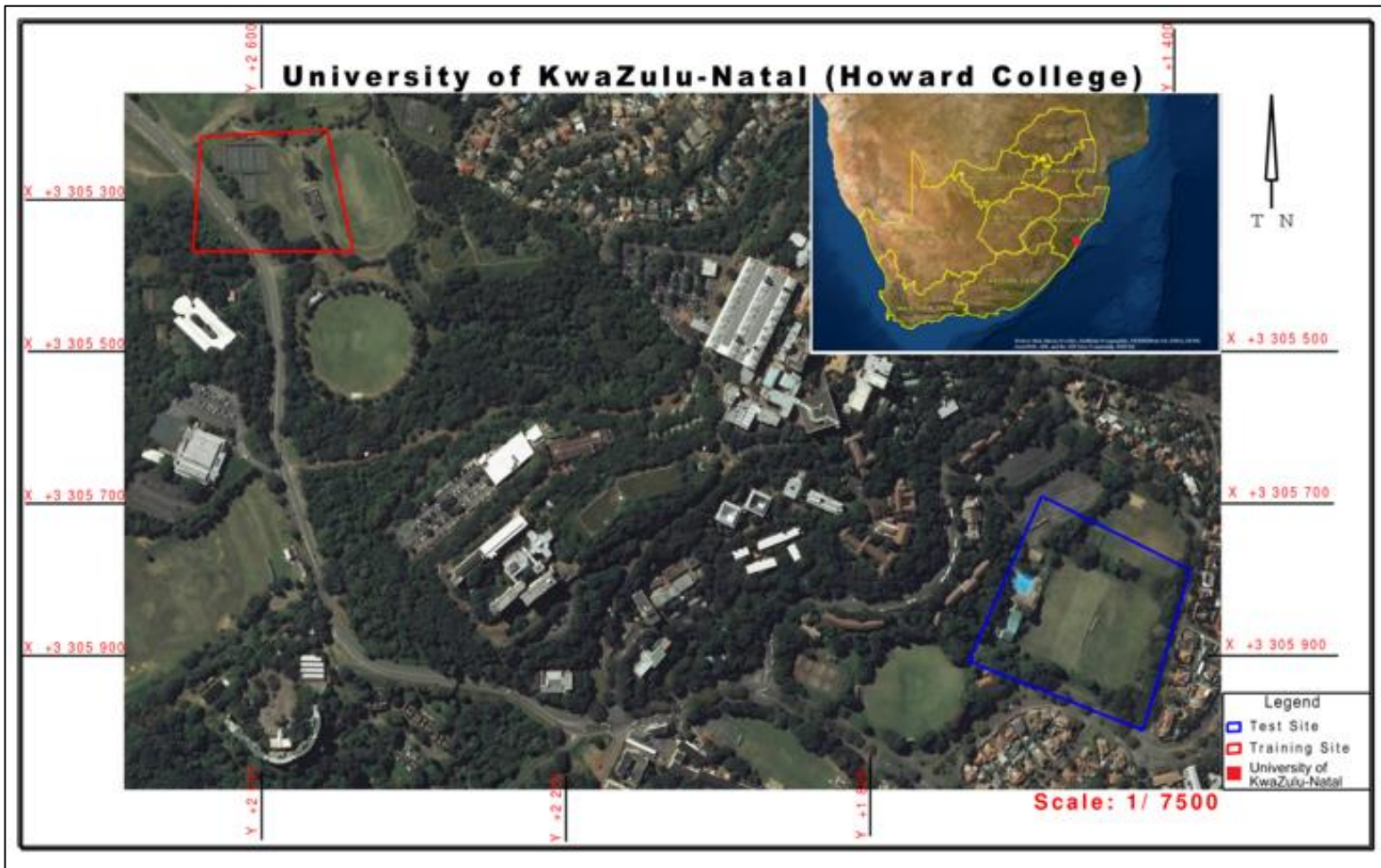
Figure 3-3: The location of the study sites, WGS84/Hart94 - Lo31

CHAPTER 4

RESEARCH METHODOLOGY

4.1   Introduction

This chapter covers the materials, instruments required and methods employed in this research. A chronological sequence of tasks is explained comprehensively, starting with camera calibration, planning, acquisition of images, data preparation, and ending with the actual classification of 3D UAV point clouds.

4.2   Outline of Research Methodology

The methodology of this research was subdivided into seven phases. The first phase involved project planning, which included site visits and determining the type of equipment to be utilized for the collection of data. The second phase involved the acquisition of chessboard images and camera calibration to determine the parameters of the camera lens. The data was further collected; the third phase dealt with site measurements of GCPs and the acquisition of images of the study area, including the test area. The fourth phase involved the generation of 3D point clouds, georeferencing, and data preparation for classification into various categories. Phase 5 is the main focus of this research, the classification of point clouds. Two different filtering algorithms were used, CANUPO and Pix4DMapper classification. Phase 6 involved the interpretation and analysis of results obtained from different filtering algorithms. In addition, the assessment of accuracy was performed. The comparison of classification results was conducted in phase 7, which was the final step. Figure 4-1 shows a summarized overview of this research methodology.
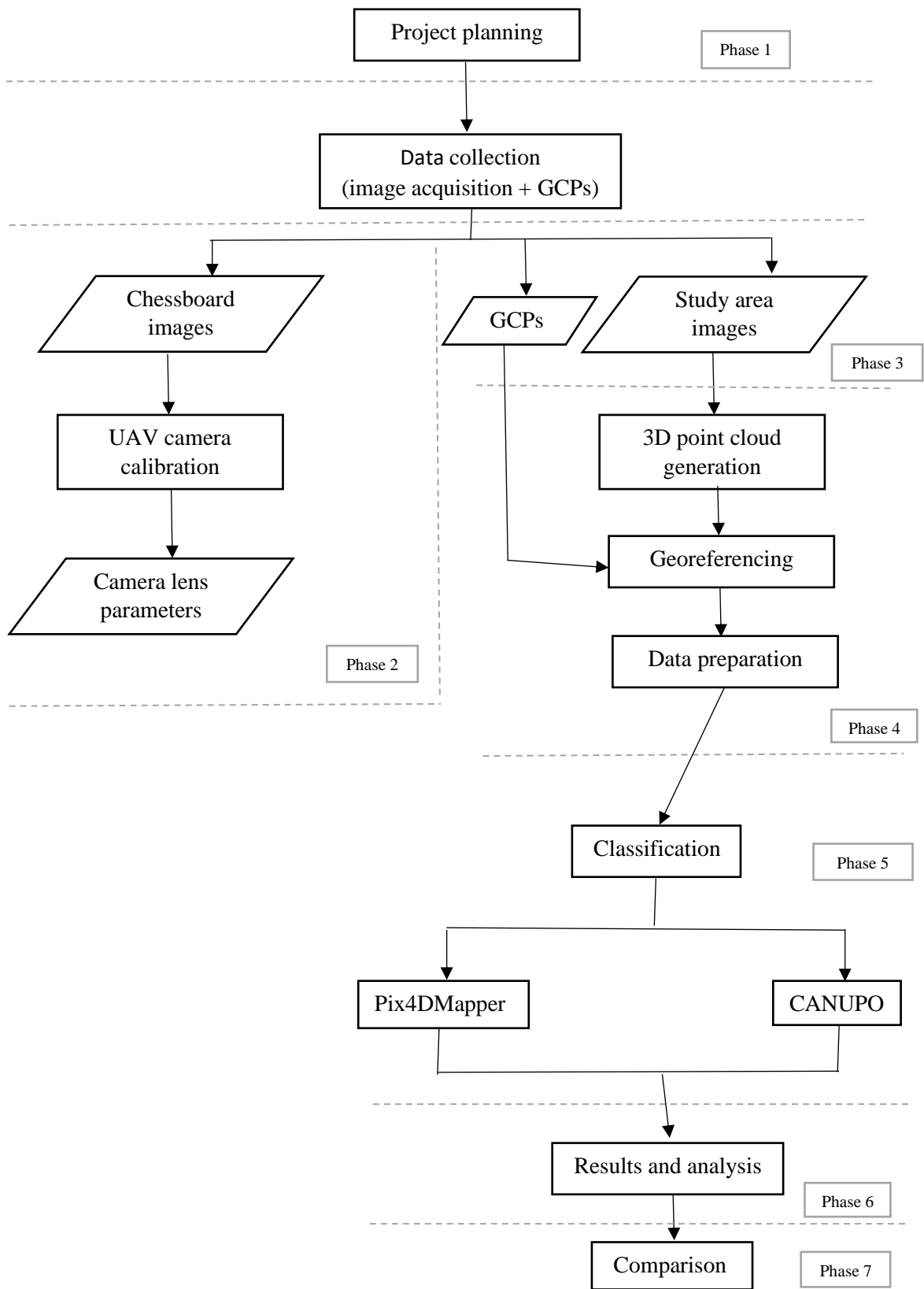
Figure 4-1: Research methodology overview

37

4.3   Materials Required

4.3.1   UAV and GPS equipment

A UAV (drone) with a CCD camera as a payload; The UAV is required as a primary instrument for acquiring images. The UAV was used to capture images required for camera calibration, the images of the test data, and the images of the proposed study area. A DJI Phantom 3 Professional quadcopter UAV was utilized in this research, remotely controlled and connected to a Samsung Galaxy tablet using the PrecisionFlight application. Figure 4-2 (DJI, 2017) shows a Phantom 3 professional quadcopter drone that was employed to acquire images for this research.

Figure 4-2: Phantom 3 Professional UAV.

The global positioning system (GPS) equipment is required for site calibration and measurements of GCPs. A Trimble R4-3 GPS was used for the collection of data.

4.3.2   Software

Various software programs were used for this research. The choice was made based on the availability of the software, mostly open-source. Google Earth Pro was used in conjunction with Precision Flight to create a flight plan. Google Earth Pro was also utilized in the search for a suitable study area. MATLAB R2018b was used to calibrate the camera lens. WebODM was used for generating the point cloud and other 3D surfaces. Finally, ArcMap version 10.7.1 from ArcGIS was used to create a map of the study area.

Different applications were required to run WedODM. Docker for Windows v19.03, Python 2.7, Git, Pip, and Powershell were used. Pix4Dmapper was used to perform the unsupervised classification of a point cloud. The segmentation and the supervised point cloud classification were performed using the CANUPO module from CloudCompare 2.11. alpha, the leading software for this research.

4.4 UAV Camera Calibration

Camera calibration is a fundamental constituent in computer vision applications (Fetić et al., 2012). The camera calibration process aims to achieve 2D image coordinates from the 3D coordinates of an object; in other words, the intrinsic and extrinsic camera parameters are determined (Fetić et al., 2012; Zhang, 2000).

The intrinsic camera parameters include the focal length, principal point, skew coefficient, and distortions. The rotations and translations are the extrinsic camera parameters (Bouguet, 2015). The camera calibration steps are outlined in figure 4-3.
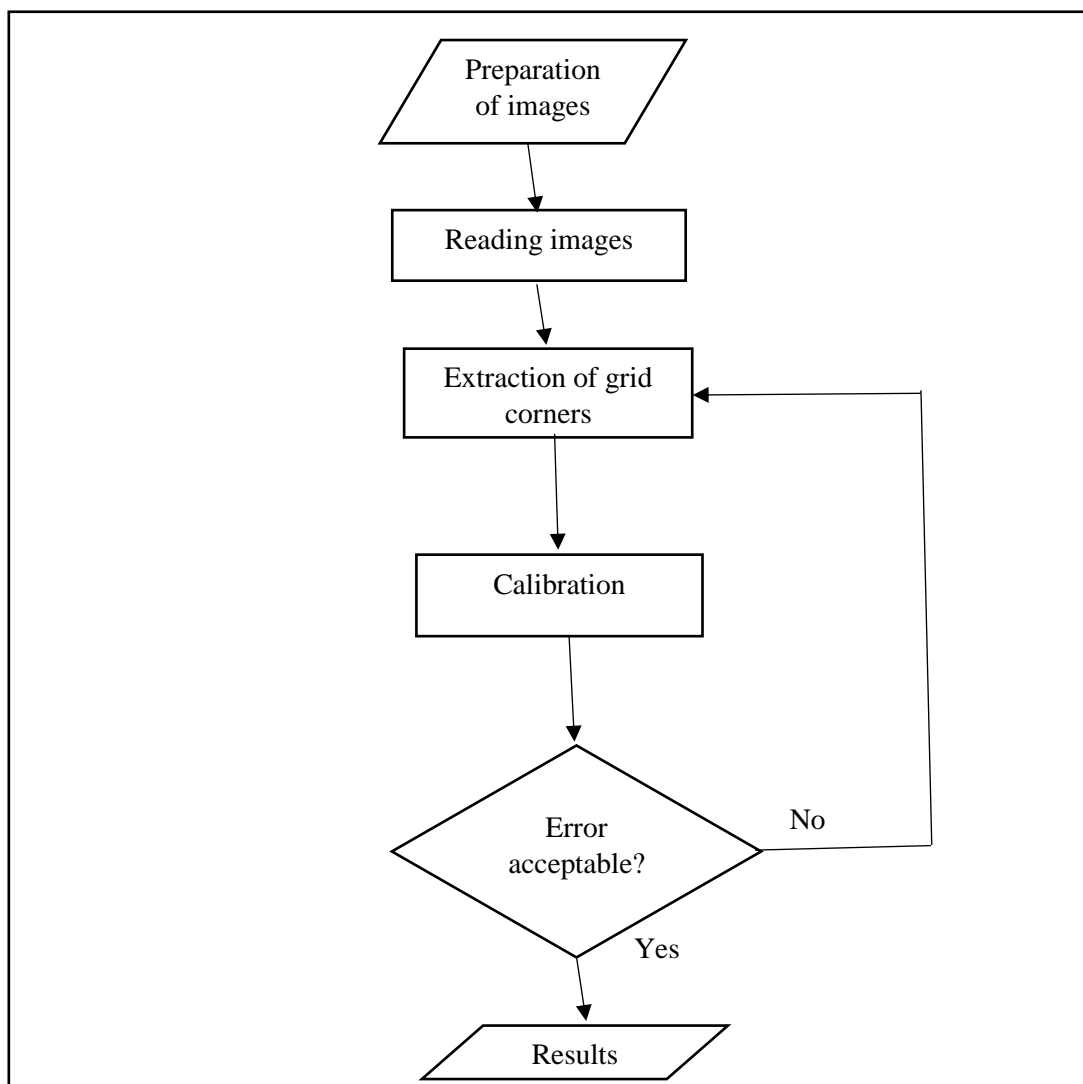
Figure 4-3: Camera calibration steps.

The calibration was performed using MATLAB programming software. Using a camera calibration toolbox for MATLAB by Bouguet (2015) and following the procedure documented on the web page, the following steps were performed:

- The calibration images (chessboard) were captured at different camera attitudes using a phantom 3 professional UAV and saved to a separate folder.
- The scripts used for calibration were downloaded and saved to a separate folder. This folder was added to the path in MATLAB.
- The main calibration function was run and the standard mode was selected since the computer had sufficient memory.
- The camera calibration toolbox displayed in figure 4-4 appeared on the screen:
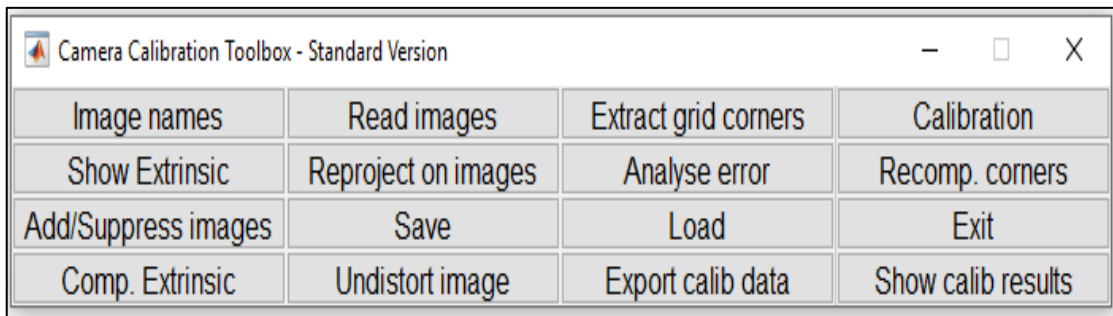
Figure 4-4: Camera calibration toolbox.

- The 'Read images' function was selected, a total of 8 images were read; MATLAB requires the prefix of the image names to be specified. Figure 4-5 shows the images used for camera calibration.
- Starting at the same reference corner, grid corners were extracted from all images, and the sizes of the chessboard squares were specified as 35mm by 35mm (along the x and y-direction).
  7 and 9 squares were detected in the x and y directions, respectively and the default window size of 63 by 63 was used.
- The calibration was performed by clicking the 'Calibration button' from the toolbox. The results were shown on the command window.
- If the calibration results are unsatisfactory, the pixel error is huge and not acceptable. Then the calibration procedure must be repeated. Inaccuracies may cause this during the extraction of grid corners.

It is necessary to calibrate a CCD (charge-coupled device) camera due to their increasing utilization in professional and scientific applications requiring high-quality image data (Fetić et al., 2012). In machine vision applications, the camera calibration enables the camera to be utilized as a measuring device (Nedevschi et al., 2002). In other words, camera calibration determines whether a particular camera is fit to be used as a device from which measurements can be taken.
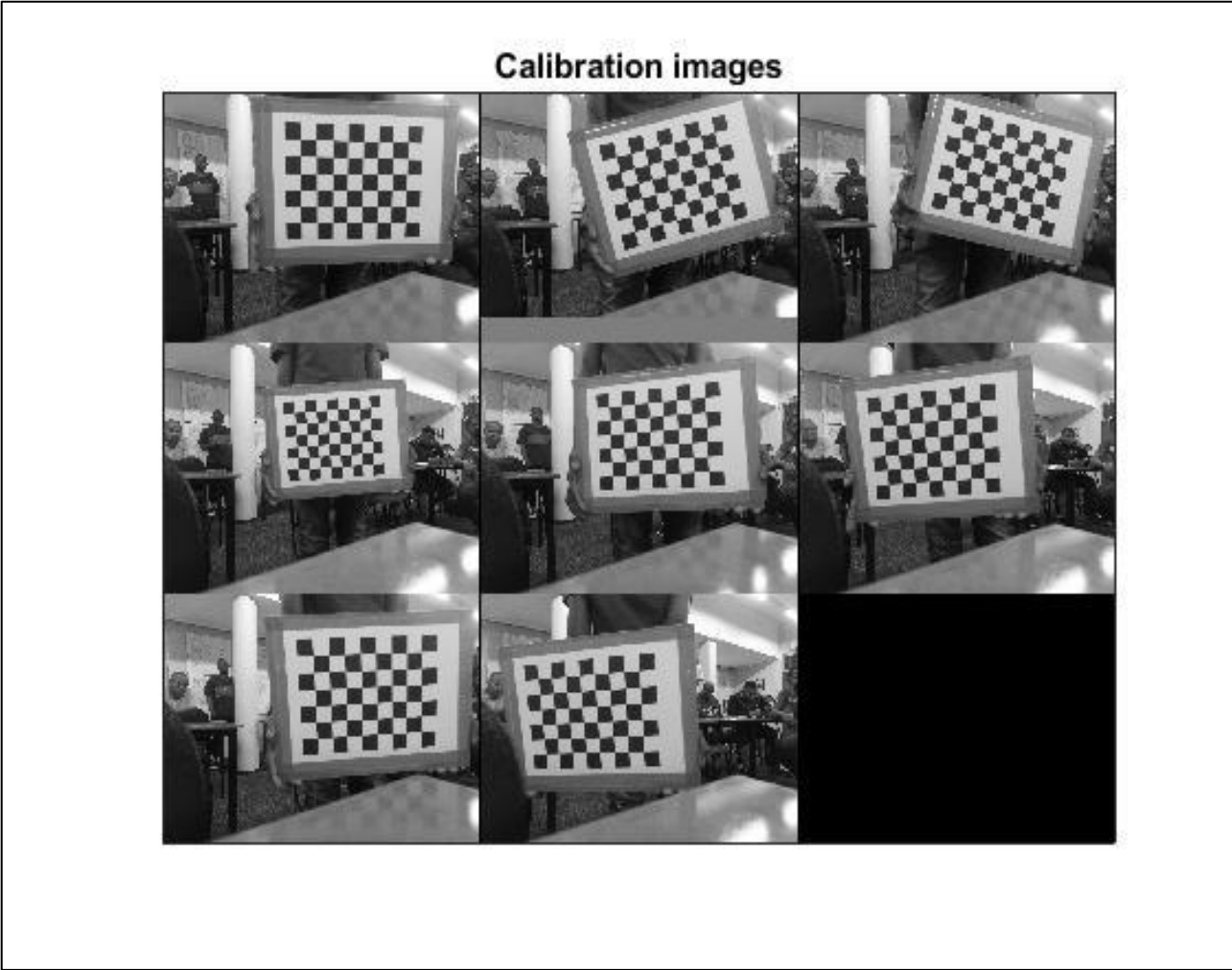
Figure 4-5: Chessboard images used for UAV camera calibration

4.5   Project Planning

4.5.1   UAV Flight Planning

Before every photogrammetric project, a flight plan is necessary. First, a reconnaissance survey was conducted whereby the study area of interest was inspected. The objective of planning is to determine the most suitable camera exposure stations and flight lines. This reduces the cost of aerial surveys and speeds up the arrangements to start the flight mission and considers the safety of the flight (Demirel et al., 2004). In contrast with the past, present UAV technologies are much faster than classical photogrammetry.

The PrecisionFlight application was utilized to create a flight plan shown in figure 4-6. This was achieved by panning on the map and drawing a polygon surrounding the study area. The flying height was fixed to 60m above the ground. The image overlap was 80% and the sidelap of 70%. The duration of the mission from taking off to landing was 11 minutes and 21 seconds.
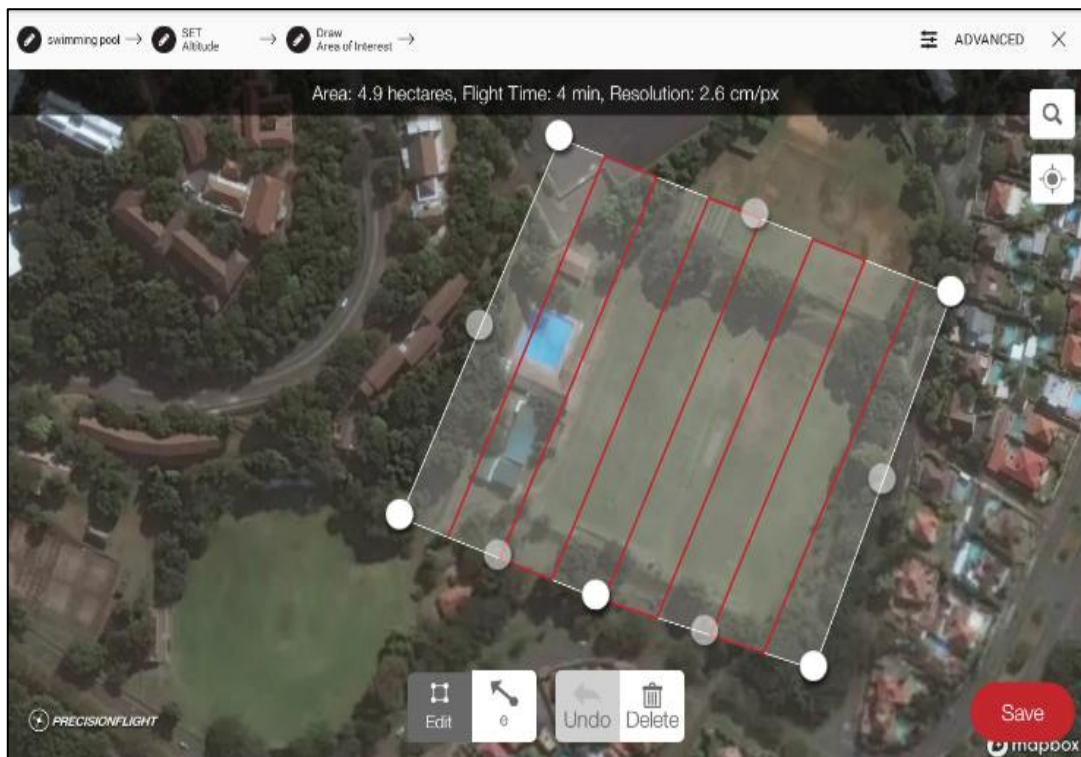
Figure 4-6: Flight Plan created using PrecisionFlight.

4.6   Data Collection

4.6.1   Acquisition of Aerial Imagery

The collection of data was divided into two sections. The first part was capturing images for UAV camera calibration and the second part had to do with the actual images of the study area. Chessboard images were taken at different orientations with a UAV resting on top of a table. Numerous images were captured, and blurry images were discarded.

The presence of wind consumes more battery from the drone as it tends to counteract the movement caused by the wind; the drone must be stable in the air. Therefore, the data was collected during a sunny day with static atmospheric conditions. This was the second part of data capture, whereby the images of the study area were taken.

The flight mission was uploaded to the UAV using the PrecisionFlight application running on a Samsung Galaxy tablet. The entire mission was automated and there was no disturbance. 90 images were captured using a Phantom 3 Professional UAV with seven flight lines covering 4.9 hectares ($0.049km^2$). Truly vertical images were taken at the height of 60m above the ground. The images were copied to the external hard drive, all having a Jpeg format, each associated with Exif data containing helpful information about the images.

4.6.2   GPS Survey

The GPS survey was conducted using a Trimble R4-3 GPS connected to the virtual reference station (VRS). A connection to a single base in Durban was established for corrections to the rover. A local Trignet connection was established and the calibration was performed on the trigonometrical beacon Biesheuvel (TR621) and checked on another trigonometrical beacon Rekaju (TR99). The site calibration was necessary to reference the project to a defined coordinate system. The calibration results were excellent, with an accuracy of +/- 1cm and +/- 2cm for the horizontal and vertical measurements, respectively. The GPS calibration sheet is arranged in Appendix B.

The World Geodetic System 1984 (WGS84) coordinate system based on the Hartebeesthoek94 datum, was used. The longitude of origin for all measurements was Lo31. GCPs were measured on-site, each point observed for 30 seconds to increase the accuracy of measurements. The GCPs are necessary when aerial surveys are conducted since they bring the project to the spatial coordinate system and improve the absolute accuracy of data obtained

(Garcia and Oliveira, 2020; Geavis, 2020). In addition, real-world measurements can be obtained.

The GCPs were distributed across the entire study site to maximize the number of best possible configurations for the process of georeferencing. Figure 4-11 shows the distribution of GCPs over the study area. The coordinates of the GCPs are listed in Appendix B.

4.7   3D Point Cloud Generation

4.7.1   WebODM

A 3D point cloud was generated using WebODM, which is a free and open-source application that runs on the web. WebODM is an API (Application Program Interface) for processing drone images and produces georeferenced point clouds, maps and 3D textured models (WebODM, 2019). This API runs on all major platforms Windows, Linux, macOS, and can be integrated with software such as QGIS and AutoCAD already in existence (GitHub, 2019).

Getting WebODM running was a challenge since it requires command-line skills. However, community support was available from the Github website. Five applications needed to be installed to run WebODM, which were: Python, Pip, Git, Docker and Docker Compose. Python is a high-level, easy-to-use programming language that uses pip to install and manage Python software packages (Lutz, 2001). Git or Windows Powershell application was used to run the command lines used to start Docker. Following several steps briefed on the Github site, WebODM was successfully initiated.

Sufficient memory was required to run Docker for windows. Since Docker is a virtual drive, the computer settings should have virtualization enabled. In addition, a RAM of 4GB or above and storage of at least 16GB is required (WebODM, 2019). Once Docker begins to run, the settings should be switched from Windows to Linux containers. For WebODM to start successfully, all the five applications should be linked using the command line on Windows Powershell or Git (WebODM, 2019). WebODM started on the website: http://localhost:8000, where the username and password for logging in were created.

Once the project is created, a minimum of 5 images with an overlap of above 65% is required to be processed in WebODM (WebODM, 2019). The collected images for this project were 90 in total, with an overlap of 80% and a sidelap of 70%. Ground control points are optional when processing with WebODM. A GCP file was not uploaded since WebODM reads the positional data from images to georeference a model; however, GCPs can improve

georeferencing accuracy (WebODM, 2019). The project started using the autoprocessing node and the default settings. The time taken for processing was approximately 6 hours.

WebODM has the capability of exporting all the products and files generated. These include a 3D point cloud, an orthophoto, 3D textured model, a digital elevation model (DEM), georeferencing log, and other attribute data. The product of interest was a 3D point cloud with color information. The point cloud was visualized on WebODM, and it appeared to be registered such that there was no missing data except the water body, which appeared to have lost its color. The steps involved in the generation of a 3D point cloud are shown in figure 4-7.
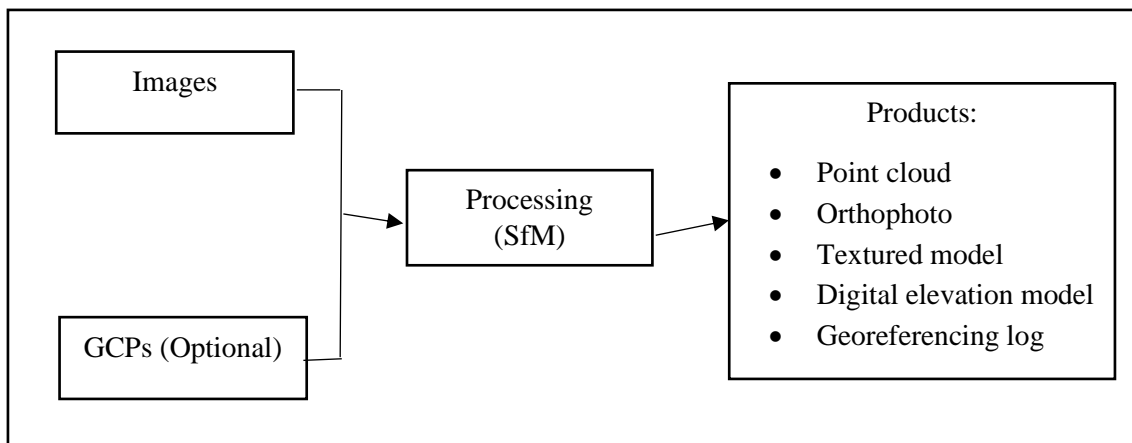
Figure 4-7: Generating photogrammetric products using WebODM

4.7.2 Pix4DMapper

The point cloud was generated in WebODM. However, Pix4DMapper was also used to produce a point cloud. Pix4dMapper is a commercial photogrammetry software for processing images taken by a drone (Pix4DSA, 2019). Unlike WebODM, no programming skills are required to start a project on Pix4DMapper; the entire process was automated. The reason behind using Pix4dMapper was to compare the point clouds from WebODM and Pix4dMapper. The two software uses the same SfM technique, transforming 2D images into 3D models.

The same number of images, nadir and 90 in total, were added to a new project on Pix4DMapper. A 3D maps option that produces othormosaic, DSM, and a point cloud was selected to process the images. This option is associated with slow processing speed; however, it supports both oblique and nadir flights. In addition, aerial images acquired utilizing grid

flight plans with high overlap are recommended for this software (Pix4DSA, 2019). Thus, the flight plan was in a grid format.

The stages involved in Pix4DMapper are as follows:

- Initial processing
- Point cloud and Mesh
- DSM, Orthomosaic and Index

Once the project begins to run, the image keypoints are computed; this takes much time, and it depends on the number of images imported. First, the keypoints are written, followed by computing and writing matches. The automatic tie points are initialized. These are points that are visible in multiple images and can be utilized as GCPs since they are visible (Remondino et al., 2017). The tie points are built and initialized. Lastly, the camera calibration report is produced by Pix4DMapper, giving the parameters of the camera lens and distortions.

4.8   Georeferencing

The georeferencing process was performed during the generation of the point cloud. The GCPs were not uploaded, but instead, the software used the geotag information from Exif data. The drone recorded this metadata during the flight mission. Each image is associated with the geographic coordinates measured with the GPS onboard. The SfM process used the Universal Transverse Mercator (UTM) coordinate system. The resulting point cloud was situated on the UTM zone 36S coordinate system. The actual georeferencing on Pix4DMapper was performed at a later stage after generating the point cloud. The surveyed GPS points in the Hartebeesthoek94 coordinate system were converted to the UTM zone 36S system using a coordinate conversion utility obtained from the Chief Directorate of National Geo-Spatial Information. Coordinates were converted to be recognized by the Pix4Dmapper software. The converted GCPs are listed in appendix C.

The UTM coordinate system was transformed into the South African National Grid, the Hartebeesthoek94 Lo31. This was performed using the transformation tool in ArcMap. The orthomosaic was further georeferenced using the natural GCPs measured with a GPS instrument. The point cloud was also transformed into Hartebeesthoek94 Lo31. At this point, both the point cloud and the orthomosaic of the study area were in the same coordinate system.

4.9   3D Point Cloud Classification

4.9.1   Unsupervised Classification using Pix4DMapper

The classification algorithm in Pix4DMapper uses the pixel values and the geometry to identify object classes. It is also crucial to state that Pix4DMapper acknowledges that more work needs to be done regarding their machine learning algorithm (Pix4D, 2017). Becker et al. (2017) introduced the incorporation of colour information in addition to the geometric features. This machine learning technique allows the users to define their object classes of interest and it will be comprehended in Pix4DMapper in the future. The current Pix4DMapper software does not support any supervised classification option. However, the tools for managing and refining the classification are provided (Pix4D, 2017).

The classification approach utilized by the Pix4DMapper software is fully unsupervised. There was no option to train the classifier and the entire process was automated. Before densification, the initial point cloud was displayed as a sparse point cloud under the 'tie points' layer. This point cloud was not vivid; the features could not be easily identified. Next, another layer titled 'Point Clouds' was loaded, and this layer displayed a densified point cloud, vivid and comprised of clearly identifiable features.

The point clouds layer contained the following groups:

- Unclassified
- Disabled
- Ground
- Road Surface
- High Vegetation
- Building
- Human Made Object

The unclassified group comprises of points not belonging to any other group and all points are unclassified by default. The disabled group contained points not to be utilized to generate DSM, orthomosaic and index (Pix4DSA, 2019). The remaining groups pre-established for point cloud classification are ground, road surface, high vegetation, building, and human-made object. Unchecking the boxes next to these groups hides the classified points for each group if the classification was successful (Pix4DSA, 2019).

After the classification process, point cloud groups were modified. Points incorrectly classified were manually digitized and allocated to the appropriate classes. This was performed for all classes and the classification process was therefore repeated. The results after re-running the classification tool were visually impressive such that the buildings were classified as buildings. This was true for the rest of the classes. Figure 4-8 shows the procedure that was followed on Pix4DMapper. First, the densified point cloud was cleaned by removing the outliers. This was achieved using the edit tool, which allows the user to manually select the points by drawing polygons and assigning them to a new group, Group 1. Unchecking the new Group 1 class removes the selected points from the entire cloud.
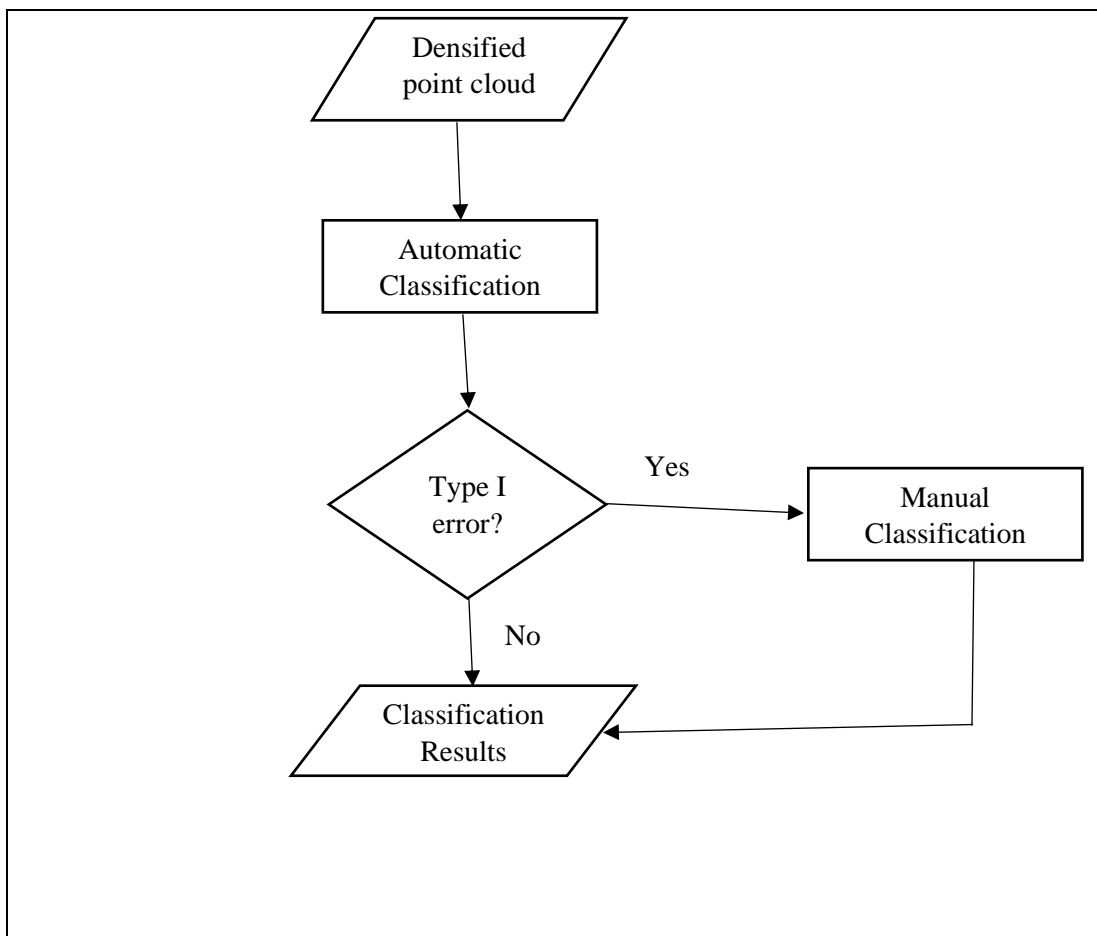
Figure 4-8: Classification procedure in Pix4DMapper.

4.9.2   Classification in CloudCompare

A free and open-source 3D point cloud software CloudCompare, for editing and processing, was utilized for automatic classification. The classification process was performed using a supervised approach that utilized training samples for the classification of different objects. This supervised approach used the multiple-scale CANUPO (CAractérisation de NUages de POints) suite as a plugin developed by Brodu and Lague (2012) to classify a 3D point cloud automatically.

4.9.2.1 Supervised Classification using CANUPO

The CANUPO plugin was employed to perform the automatic classification of points in a 3D point cloud. It is based on the local dimensionality characteristics of points in a point cloud. Points can be classified as 1D, 2D, or 3D depending on a specified scale and location. For example, consider a site (such as figure 3-3) consisting of the power line, the ground surface, trees, and buildings. At a scale of a few centimeters, the ground surface and the building walls will appear as 2D; the trees will appear as a mixture of 1D (branches) and 2D (leaves). At a sizeable scale (~50cm), the ground surface will still look 2D, and the trees will be 3D, while the power lines will remain 1D (Brodu and Lague, 2012).

A combination of information from various scales contributes towards the creation of descriptors that can recognize other object classes present in the scene. This was achieved by employing support vector machines (SVM) and linear discriminant analysis (LDA) (Brodu and Lague, 2012). During the training stage, the descriptors are determined automatically. The creation of a classifier involves two steps: firstly, the data is projected on a plane of maximal separability; secondly, the classes in that plane are divided employing a boundary (Brodu and Lague, 2012). The point cloud is divided into two subsets when the classifier is applied and only one classifier at a time. The advantage of CANUPO is its ability to give a classification confidence value, which enables the user to troubleshoot troublesome cases. Since it employs a probabilistic approach, incorrectly classified points can be filtered from a specific class (Brodu and Lague, 2012).

The training data was obtained from a different area of study shown in figure 3-2. The point cloud generated using the SfM technique was utilized for the extraction of training samples. Additional imagery from another different area was used to generate a 3D point cloud. The final training samples were obtained from different point clouds. The samples were merged to

increase the chances of training robust classifiers. Figure 4-9 shows a different 3D point cloud from which additional training data was extracted.

Figure 4-9: Additional 3D point cloud for training data.

Three classes were defined for classification: Ground, High Vegetation, and Building. This was performed using the segment tool in Cloud compare. The class representatives for training the classifiers were obtained from a different point cloud to distinguish between the training and the testing data. Using the CANUPO plugin, two samples at a time were selected. The first classifier, classifier A was trained to filter ground from non-ground points. The second classifier, classifier B, separated high vegetation from a building. To speed up the training process, the points were subsampled to reduce the number of core points used during the computation of descriptors.

Trials were conducted to find the best combination of scales to be utilized for the computation of descriptors. Both classifiers were trained at 12 almost similar scales. The scales ranged from as small as 0.04m up to 50m. The classifiers' competence was examined using the balanced accuracy, ba (equation 2.11), and the fisher discriminant ratio, fdr (equation 2.14) incorporated by Brodu and Lague (2012). Figure 4-10 illustrates the classification approach used to achieve multiple classes.
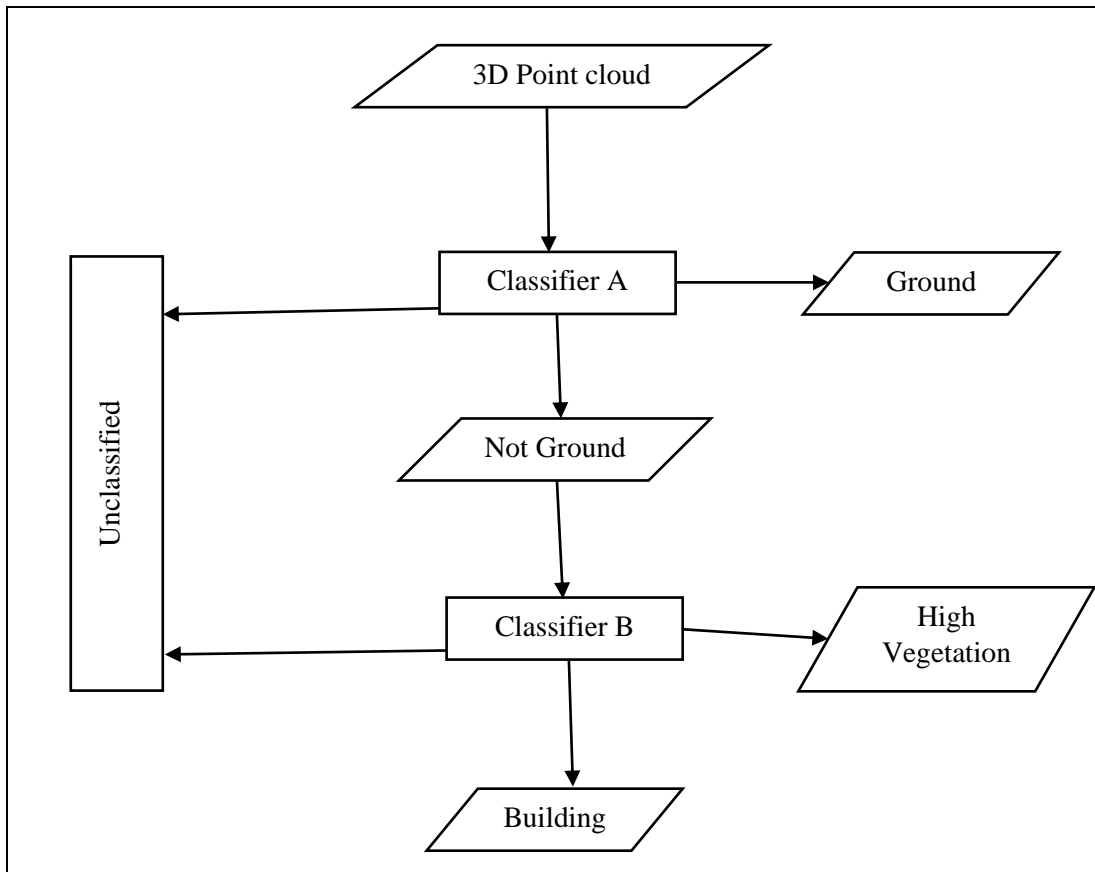
Figure 4-10: CANUPO classification approach

The entire point cloud was first classified using classifier A. Since classifier A aims to filter ground from non-ground, all the points labelled ground were filtered according to the scalar field value assigned to them. The remainder was non-ground and unclassified points. The non-ground class was also separated from the unclassified points following the scalar field value assigned to them. Classifier B was applied to the non-ground class. This classifier separated high vegetation from the building class. The same procedure was followed to filter the two classes. The remaining unclassified points were added to the class of points that were unclassified using classifier A.

4.10   Accuracy Assessment

The accuracy of classification was evaluated using a georeferenced orthophoto generated from aerial imagery of the site. The same imagery used to create the orthophoto was also used to generate the 3D point cloud. The confusion matrices and the Kappa coefficient were used for quantifying the accuracy. The classification results were also assessed qualitatively.

Site visits were conducted for ground truth verification since all parts of the area of study were accessible. Georeferencing simplified the process of assessing accuracy. A classified 3D point cloud was verified using a georeferenced orthomosaic. Also, the site was surveyed using a Trimble R4 GPS to measure the positions of checkpoints precisely.

4.10.1 Qualitative Assessment of Accuracy

The performance of the Pix4DMapper classification tool was evaluated qualitatively, employing the approach utilized by Sithole and Vosselman (2004) for classifying bare earth and object classes. On the Pix4DMapper user interface, the Type I and Type II error were easily identified. Furthermore, the points belonging to a particular class were visualized; unchecking the class layers made the points invisible and the opposite was true. The same approach employed in the evaluation of the Pix4DMapper classification was adopted for the CANUPO classification.

4.10.2 Quantitative Assessment of Accuracy

The CANUPO classification, which is the main focus of this research, was further assessed quantitatively. The ground truth information was obtained through site visits and precise GPS surveys since the study area was accessible. Some ground truth information was gathered using GIS techniques. An orthorectified mosaic was used for digitizing points to extract additional information of the sites where the GPS could not operate.

Random checkpoints were generated using ArcMap. In addition, the ground truth points were surveyed using a GPS to add more points for accuracy assessment. The checkpoints generated from ArcMap were associated with the positional data, Y and X coordinates. These points were also located on the georeferenced 3D point cloud. The classified point cloud was checked against the georeferenced orthomosaic for validation of ground truth. This information was used for developing a confusion matrix from which the classification accuracy was quantitatively assessed. Figure 4-12 and figure 4-13 show the ground truth sites. The coordinates of checkpoints used for ground truth verification are listed in Appendix B. Figure 4-14 showing the classified point cloud layer over the orthomosaic was captured from ArcMap.
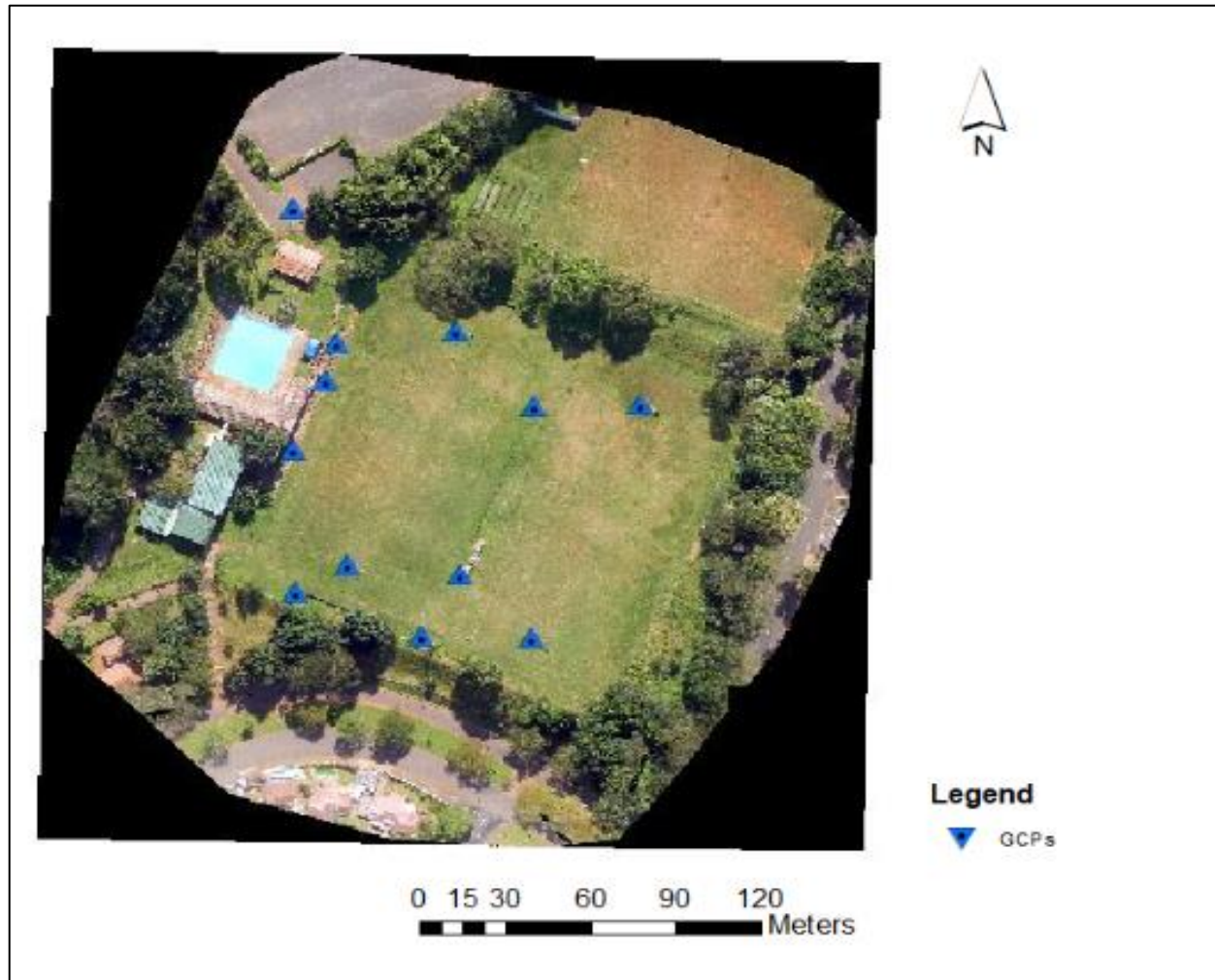
Figure 4-11: Ground Control Points
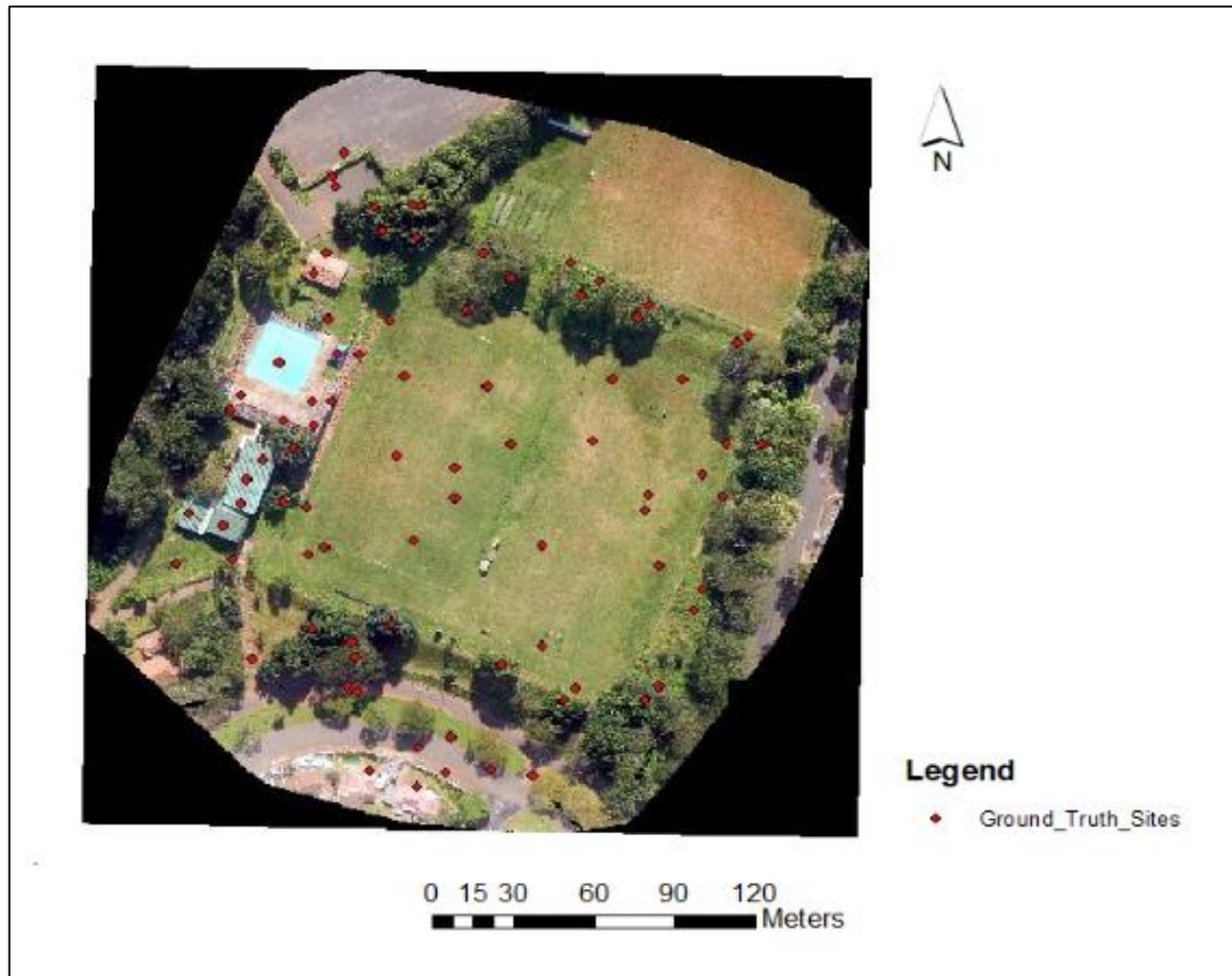
Figure 4-12: Ground truth sites
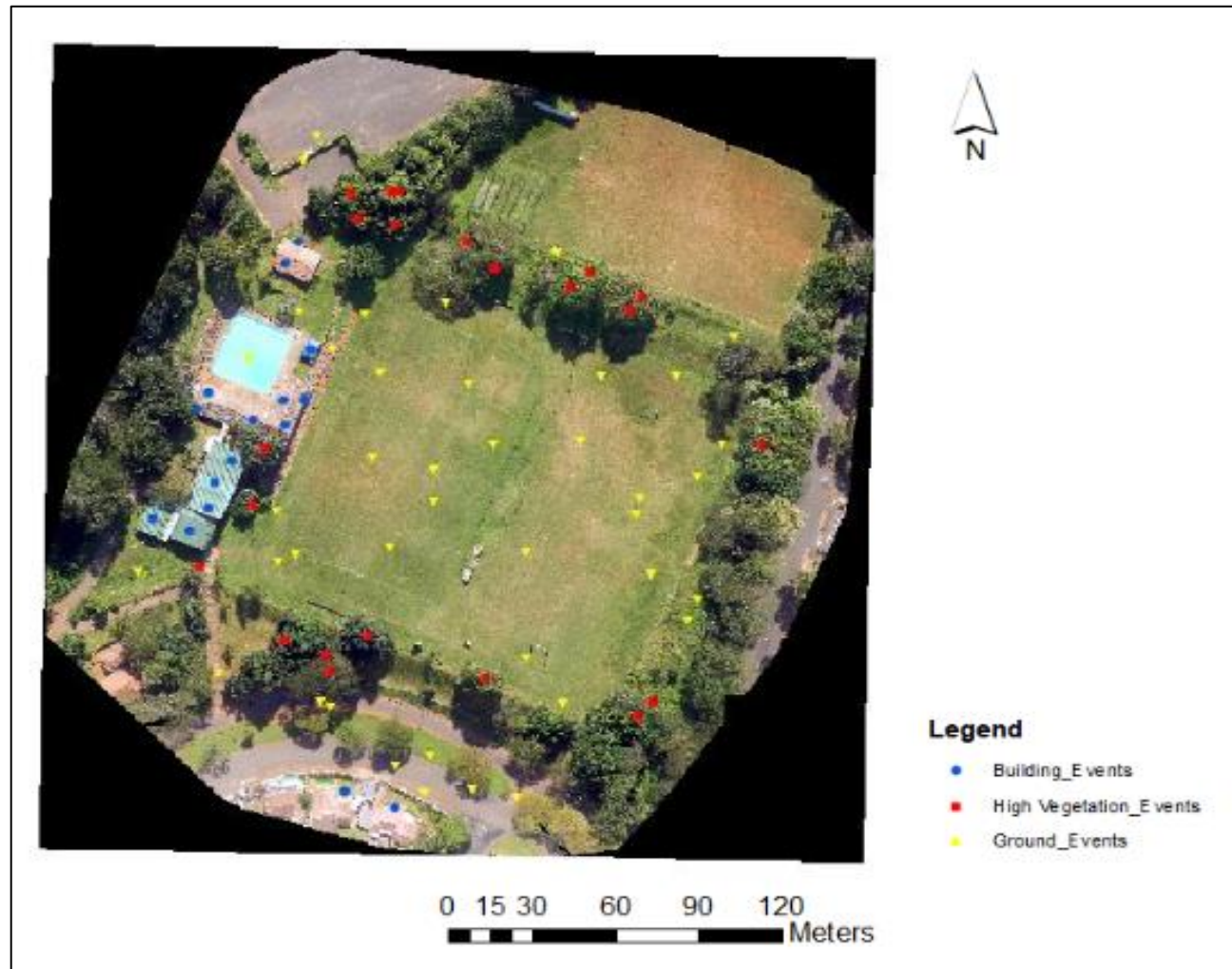
Figure 4-13: Ground truth site categories
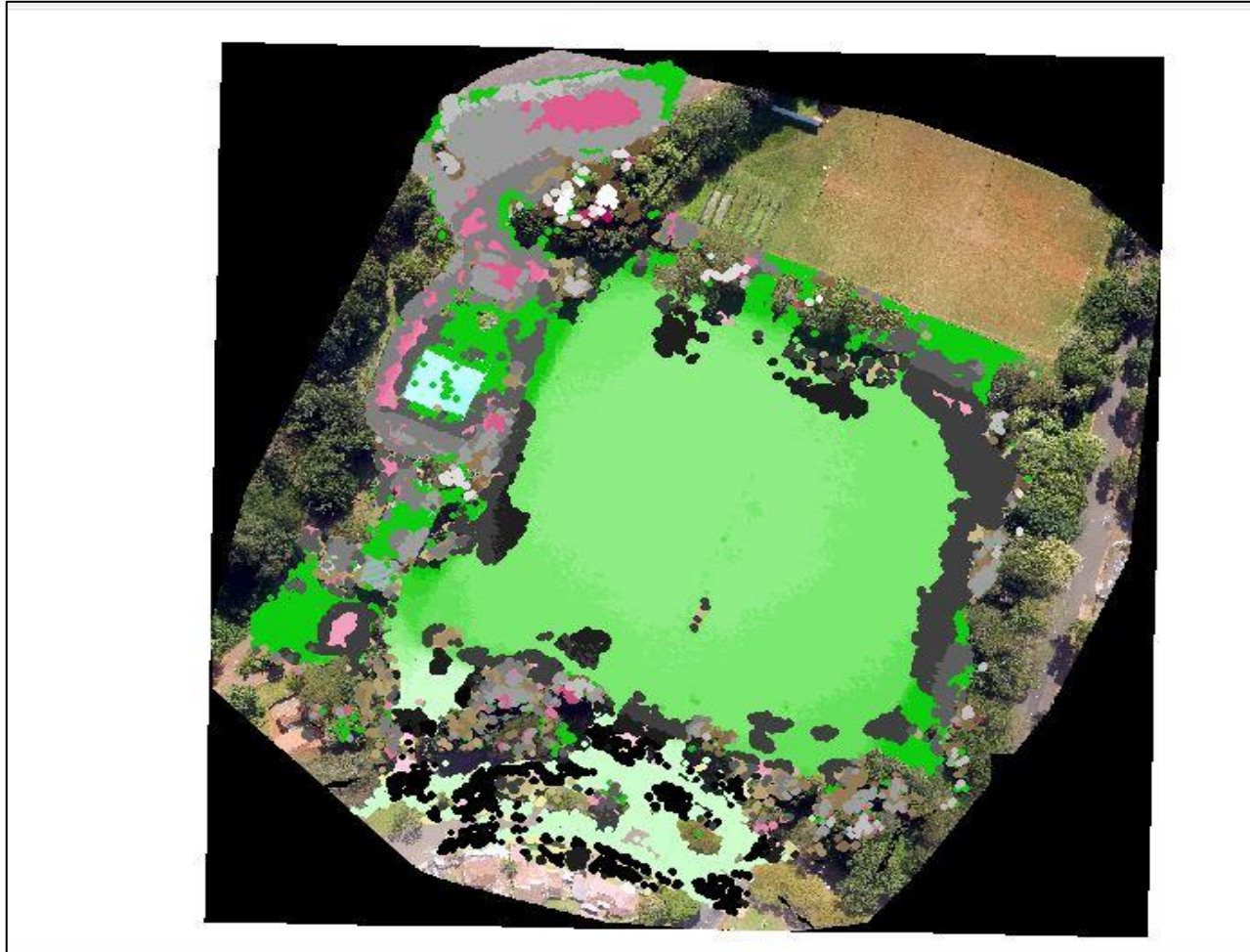
Figure 4-14: Classified point cloud layer over the orthomosaic

4.11 Summary

This chapter outlined a chronological sequence of processes followed for this study. The primary data was collected using a drone, and the SfM technique was adopted to generate a 3D point cloud. Ground truth information was verified through site visits and the use of a GPS survey. To perform the classification of points, both supervised and unsupervised approaches were employed. The accuracy of the classification was assessed using both qualitative and quantitative assessment measures. Finally, the error matrix and the Kappa statistic were computed to quantify the overall accuracy of classification.

CHAPTER 5

RESULTS AND ANALYSIS

5.1   Introduction

This chapter presents the outcomes of this research. The results from the calibration of the UAV camera, generation and the classification of a 3D point cloud are detailed. The classification accuracy assessment results are also included in this chapter. Matrices, tables, graphs, maps and pictures from software are utilized to present the results.

5.2 UAV Camera Calibration Results

The calibration results were calculated in two steps. The first step produced parameters after initialization, while in the second step, the parameters were computed after optimization. In the initialization step, the distortions were not included. On the other hand, the non-linear optimization was comprised of lens distortions.

Calibration parameters after initialization:

- Focal Length: fc = [2326.92147   2326.92147]
- Principal point: cc = [1999.50000   1499.50000]
- Skew: alpha_c = [0.00000]   => angle of pixel = 90.00000 degrees
- Distortion: kc = [0.00000   0.00000   0.00000   0.00000   0.00000]

Calibration results after optimization (with uncertainties):

- Focal Length: fc = [2346.62700   2349.88146] +/- [61.58243   61.28156]
- Principal point: cc = [2014.79146   1510.17880] +/- [5.93212   9.38874]
- Skew: alpha_c = [0.00000] +/- [0.00000]
                        => angle of pixel axes = 90.00000 +/- 0.00000 degrees
- Distortion: kc = [-0.00318   -0.00460   0.00293   -0.00042 0.00000]
                        +/- [0.00348   0.00613   0.00057   0.00048 0.00000]
- Pixel error: err = [0.28358   0.20695]

From these results being satisfactory, the pixel error was very small and negligible. Figure 5-1 shows the reprojection error. With the aid of this plot, the reprojection error was analyzed. This error resulted from image grid corners extracted imperfectly.
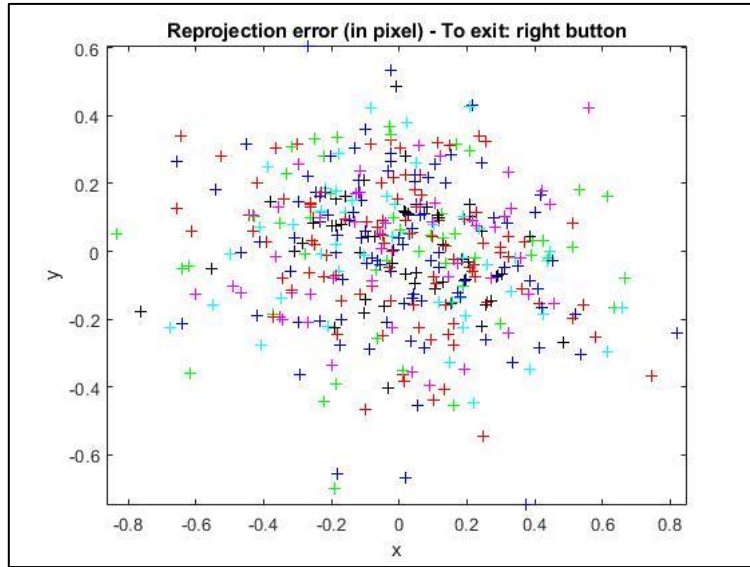
Figure 5-1: Reprojection error

The extrinsic parameters are displayed in a 3D plot. In figure 5-2, the camera reference frame is shown with the red pyramid corresponding to the camera's Field of View (FoV). The green pyramids in figure 5-3 represent the camera's positions and orientations at the time images were captured.
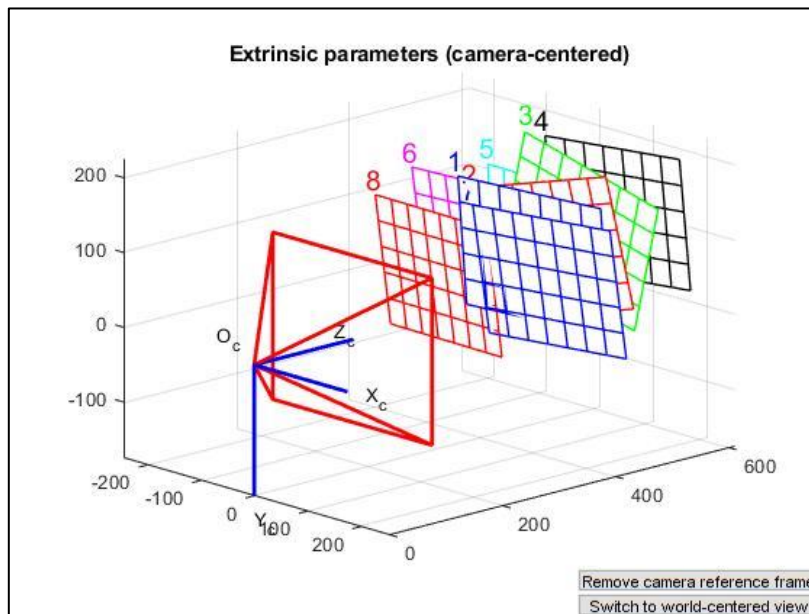
Figure 5-2: Extrinsic parameters (camera-centered)
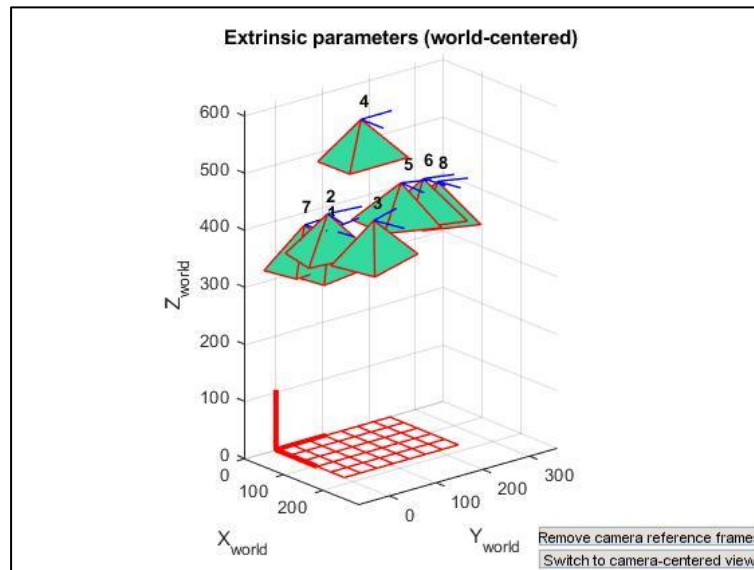
Figure 5-3: Extrinsic parameters (world-centered)

The distortions on the pixel image were visualized after running the command line 'visualize_distortions' on the MATLAB command window. Figures 5-4 and 5-5 show the tangential and radial components of the distortion models, respectively. These lens distortions were minimal and negligible. However, lens distortions introduce errors; the arrows illustrate the significant pixel displacement due to these lens distortions (Fetić et al., 2012). A complete distortion model, which includes both the tangential and radial distortion, is shown in figure 5-6.
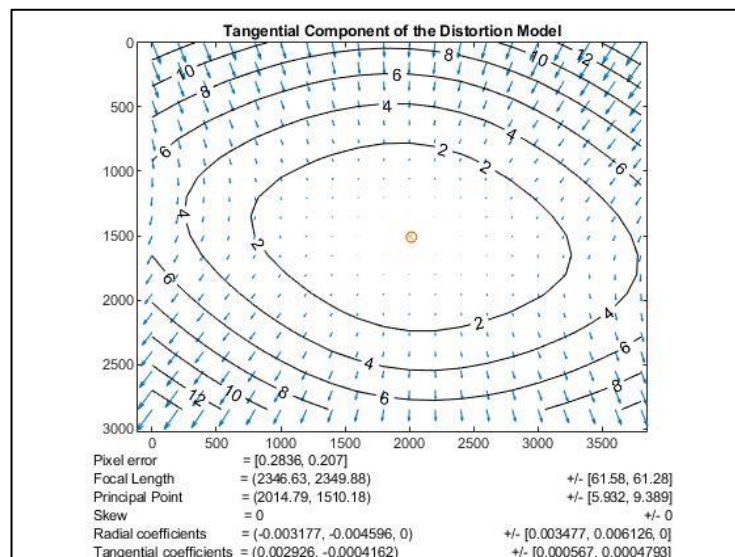
Figure 5-4: Tangential Component of the Distortion Model
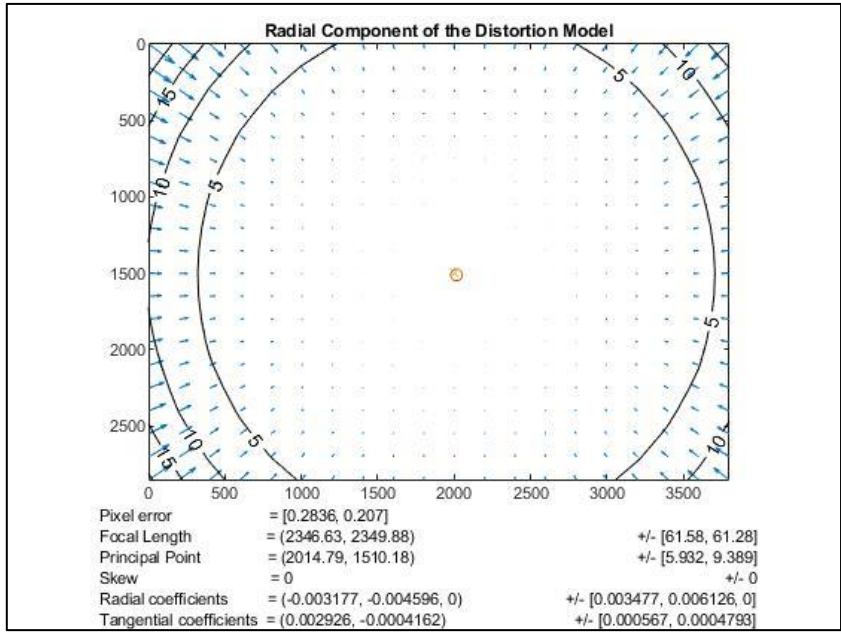
Figure 5-5: Radial Component of the Distortion Model
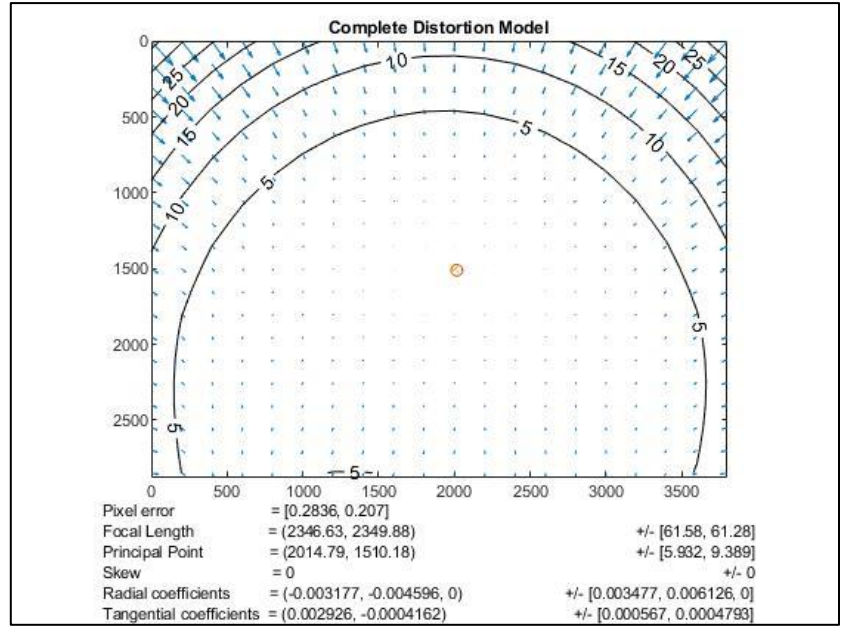
Figure 5-6: Complete Distortion Model (radial and tangential)

5.3 Point Cloud and Georeferencing

Pix4DMapper generated the point cloud in two steps. The first step produced a sparse 3D point cloud shown in figure 5-7 using the automatic tie points. This point cloud was not vivid, and its density was very low. A densified, vivid point cloud in las format was created in the second step. Figure 5-8 shows a densified point cloud created and visualized in Pix4DMapper.

Figure 5-7: Automatic tie points: Sparse point cloud

The densified 3D point cloud contained 5 706 957 points. Pix4DMapper created classes once a densified point cloud had been created, but the classes were empty with no points allocated to them. The point cloud was georeferenced using Pix4DMapper. The best configuration of 3D GCPs achieved a mean root-mean-square error of 0.032m.
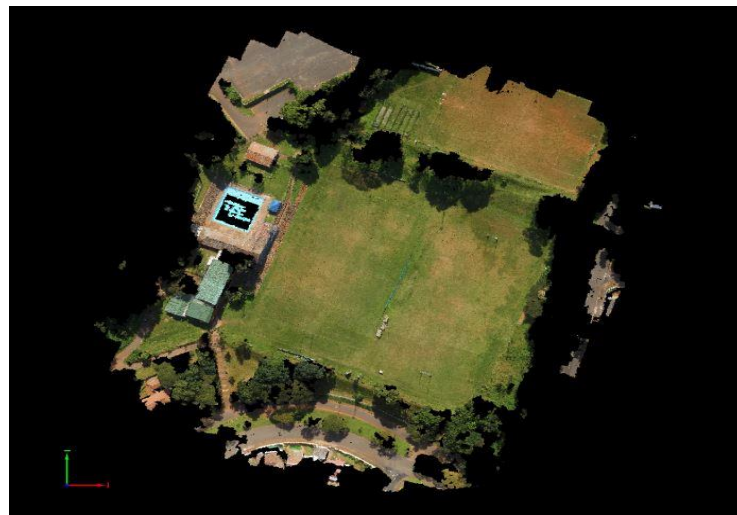
Figure 5-8: Densified point cloud

Figure 5-9 shows a 3D georeferenced laz point cloud visualized in CloudCompare. This was produced using the open-source software WebODM. This cloud of points contained 9 803 414 points, requiring fast processing machines with sufficient memory. An overall root-mean-square error of 0.053m was achieved from georeferencing using the CloudCompare software.
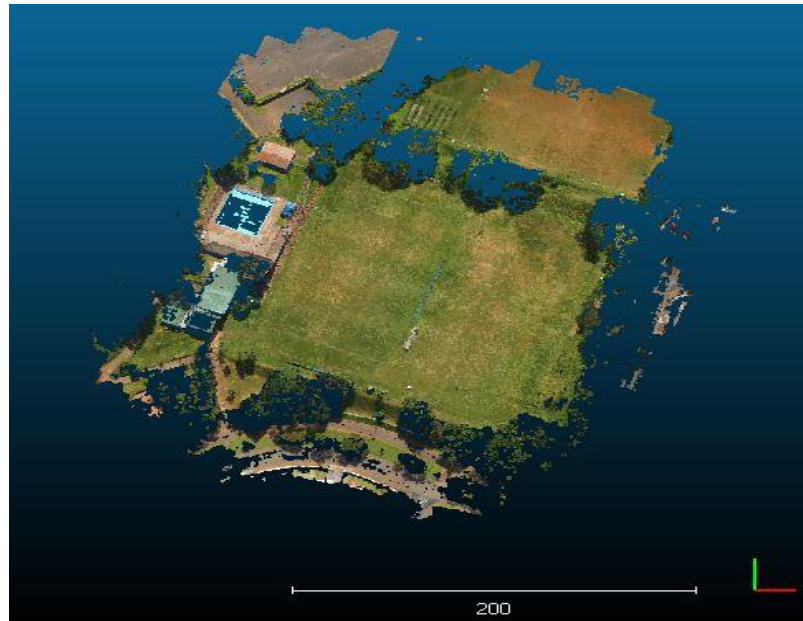
Figure 5-9: Georeferenced point cloud from WebODM

5.4   Point Cloud Classification

The classification was performed using different software employing different algorithms. The first part involved the Pix4DMapper software, which performed the unsupervised classification. The point cloud was classified using the predefined classes in Pix4DMapper. The second part utilized the CloudCompare software. The CANUPO plugin incorporated in CloudCompare was utilized to perform a supervised classification whereby the classifiers were trained using class samples and later applied to the point cloud.

5.4.1   Pix4DMapper Classification

The overall classification results were satisfactory; points were classified into appropriate groups. However, some categories appeared to have problematic results. The results were visualized in Pix4DMapper. Figure 5-10 and figure 5-11 show the classification results with the class of interest hidden since this approach was the most effective way to visualize the results. This means that the results displayed show the remainder after filtering a specific category. For example, the image corresponding to the ground category displayed what is not

ground, the remainder of points. Figure 5-10 shows the results of classification. The images at the top (in figure 5-10 (a), (b), and (c)) show the results of the unsupervised classification, while the images at the bottom (in figure 5-10 (d), (e) and (f)) show results after the manual classification whereby points were assigned into the appropriate classes.

The initial classification results were obtained from performing classification without any user interference with the classes. The classification process was fully unsupervised. The results of the final classification were obtained after the elimination of the Type I error. This was performed by manually digitizing the points belonging to a specific group and assigning them to appropriate classes. Figure 5-11 (e) shows the entire point cloud before classification. The Type II error was dominant across all classes except for the ground category.

The class labelled ground achieved the best results since the classification into this category seemed to be exhaustive. No points were manually assigned to this class. However, a Type II error was detected; some points belonging to the road surface category were classified as ground. This was a particular case of ambiguity since the road surface is also the actual ground. However, the expectations were that the road surface category would not be classified as ground. Hence the Road Surface category was dominated by the Type I error rectified by manually assigning the outstanding points.

5.4.1.1 Qualitative Assessment of Accuracy

Table 5-1 shows the qualitative performance of the Pix4DMapper classification tool. The ratings used in Table 5-1 are explained in Table 5-2.

Table 5-1: Qualitative performance of Pix4Dmapper classification tool

Feature	Associated Error	Pix4DMapper rating
Ground	Type II	***
Road Surface	Type I	*
High Vegetation	Type I	***
Building	Type I	**
Human Made object	Type I	*

*: poor

**: fair

***: good

Table 5-2: Explanation of ratings

Rating	Item filter rating	Influence rating
Poor	Item not filtered most of the time (<50%)	Huge influence on neighbouring points
Fair	Item not filtered a few times	Small influence on neighbouring points
Good	Item filtered most of the time (<90%)	None
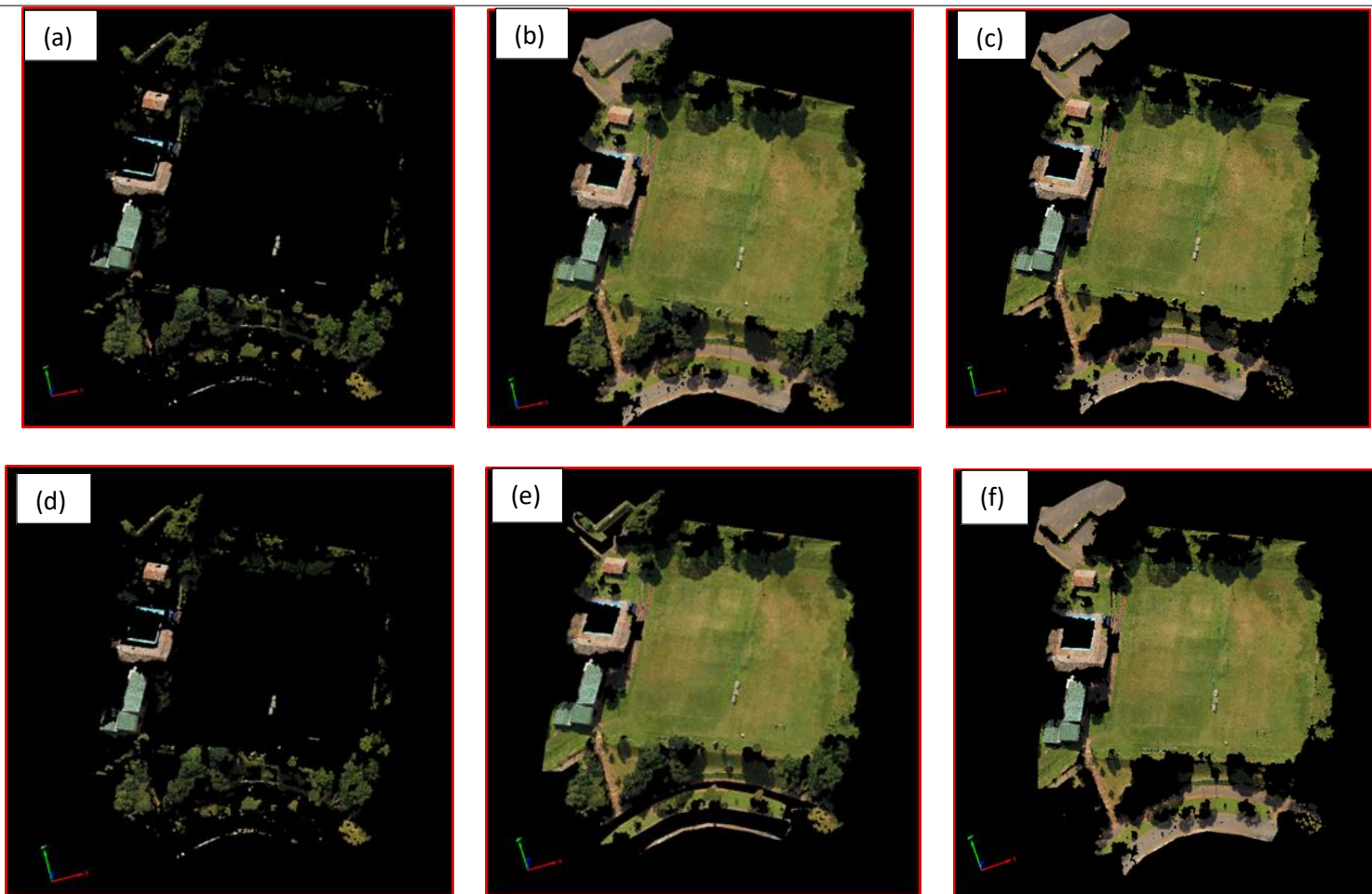
Figure 5-10: Initial classification results: (a) Ground, (b) Road Surface, (c) High Vegetation. Final classification results: (d) Ground, (e) Road Surface, (f) High Vegetation
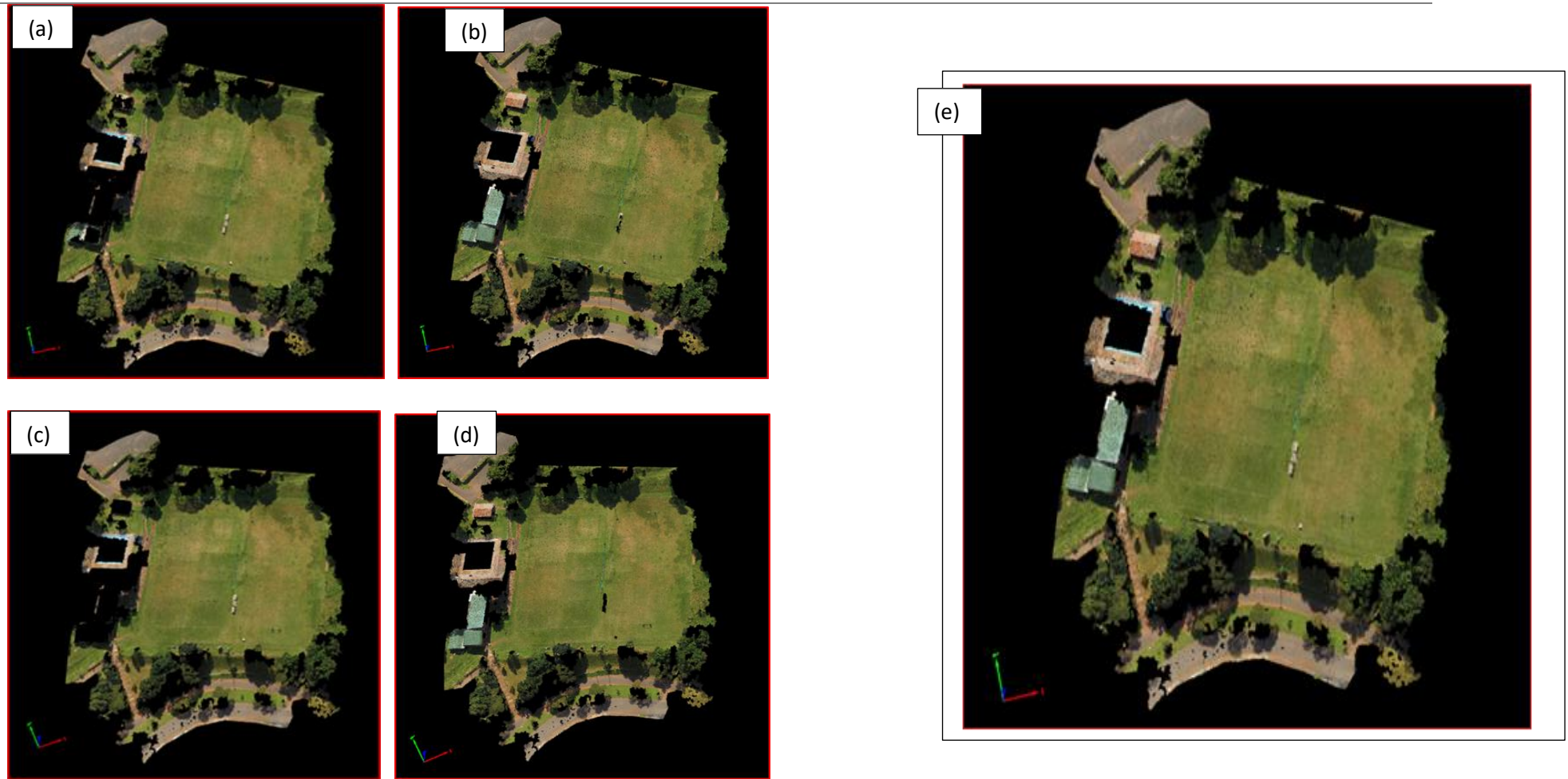
Figure 5-11: Initial classification results: (a) Building, (b) Human-Made Object. Final classification results: (c) Building, (d) Human Made Object, (e) Unclassified point cloud

5.4.2 CANUPO Classification

The CANUPO classification was conducted using the CloudCompare software. The results of classification were satisfactory, and the entire 3D scene was classified into appropriate categories. The classification using CANUPO is supervised since the user trains the classifiers. However, the classification may also be referred to as unsupervised since the classifiers were applied to a different area of study that was not seen before.

The training phase yielded excellent results. Classifier A achieved a ba of nearly 100% (0.994295) and the fdr of 6.82624. Classifier B provided a ba of 0.95715 and the fdr of 6.03814. The results were influenced by the number of scales utilized during the training process. Figure 5-12 shows the statistics of each classifier and the maximal separability of the classes involved.

Figure 5-12: Results of the training phase:(a) Separation of Ground from Non-Ground points, (b) Statistics of Classifier A, (c) Separation of High-vegetation from Building points and (d) Statistics of Classifier B.

Table 5-3: Results of the training phase - Classifier A

		Reference Data		
		Ground	**Non-ground**	**Sum**
Classified Data	**Ground**	7796	4	7780
	Non-ground	85	7715	7780
	Sum	7881	7719	15600

Balanced accuracy for Classifier A:

Accuracy of Ground (a_g) $= t_g/(t_g + f_n)$

$$= 7796/(7796 + 86)$$

$$= \mathbf{0.989}$$

Accuracy of Non-ground (a_n) $= t_n/(t_n + f_g)$

$$= 7715/(7715+4)$$

$$= \mathbf{0.999}$$

balanced accuracy (ba) $= \frac{1}{2}(0.989+0.999)$

$$= \mathbf{0.994}$$

Table 5-4: Results of the training phase - Classifier B

		Reference Data		
		High vegetation	**Building**	**Sum**
Classified Data	**High vegetation**	9578	422	10000
	Building	435	9565	10000
	Sum	10013	9987	20000

Balanced accuracy for Classifier B:

Accuracy of High vegetation (a_v) $= t_v/(t_v + f_b)$

$$= 9578/(9578 + 435)$$

$$= \mathbf{0.957}$$

Accuracy of Building (a_b) = $t_b/(t_b + f_v)$

$$= 9565/(9565+422)$$

$$\mathbf{= 0.957}$$

balanced accuracy (ba) = ½(0.957+0.958)

$$\mathbf{= 0.957}$$

5.4.2.1 Qualitative Assessment of Accuracy

Table 5-5 shows the qualitative performance of the classification using the CANUPO plugin. The ratings used in Table 5-5 are explained in Table 5-6.

Table 5-5: Qualitative performance of the CANUPO classification

Feature	Associated Error	CANUPO rating
Ground	Type II	***
High Vegetation	Type II	***
Building	Type I	**

*: poor

**: fair

***: good

Table 5-6: Explanation of ratings

Rating	Item filter rating	Influence rating
Poor	Item not filtered most of the time (<50%)	Huge influence on neighbouring points
Fair	Item not filtered a few times	Small influence on neighbouring points
Good	Item filtered most of the time (<90%)	None

5.4.2.2 Quantitative Assessment of Accuracy

The confusion matrix shown in table 5-7 was generated to perform the quantitative assessment of CANUPO classification.

Table 5-7: Results of CANUPO Classification

		Reference Data				
		Ground	High Vegetation	Building	Sum	UA (%)
Classified Data	**Ground**	**36**	2	1	39	92.3
	High Vegetation	2	**18**	2	22	81.8
	Building	2	1	**11**	14	78.6
	Unclassified	2	1	2	5	
	Sum	42	22	16	**80**	
	PA (%)	86.7	81.8	68.8		

$$\text{Overall Accuracy (OA)} = \frac{(36+18+11)}{80} * 100$$

$$= \mathbf{81.3\%}$$

Computation of the Kappa statistic:

$$\hat{k} = \frac{0.8125 - 0.3666}{1 - 0.3666}$$

$$= \mathbf{0.70}$$

A Kappa statistic of 0.70 was achieved, which is a substantial agreement according to the Kappa ratings.

Figure 5-13 shows the results of the CANUPO classification. The entire scene's classification is displayed in figure 5-13: (a), the light green, blue, and red colors represent the ground, high vegetation, and building classes, respectively. In figure 5-13: (b), the results displayed comprises of high vegetation and building classes. The ground class was filtered from the classification results leaving high vegetation and building as a remainder.

72

Figure 5-13: (c) shows the remaining points that were not classified into any defined classes. The grey color represented the unclassified points in all figures.

Figure 5-14: (a) shows the classification results whose training samples were obtained from the same test area. This is also known as a semi-supervised classification approach. In this case, the classifiers were very close to perfection since the dimensionality of points in the training samples was very similar to the dimensionality of the tested points. Figure 5-14: (b) and (c) show the unclassified point cloud, the raw and textured point clouds, respectively.
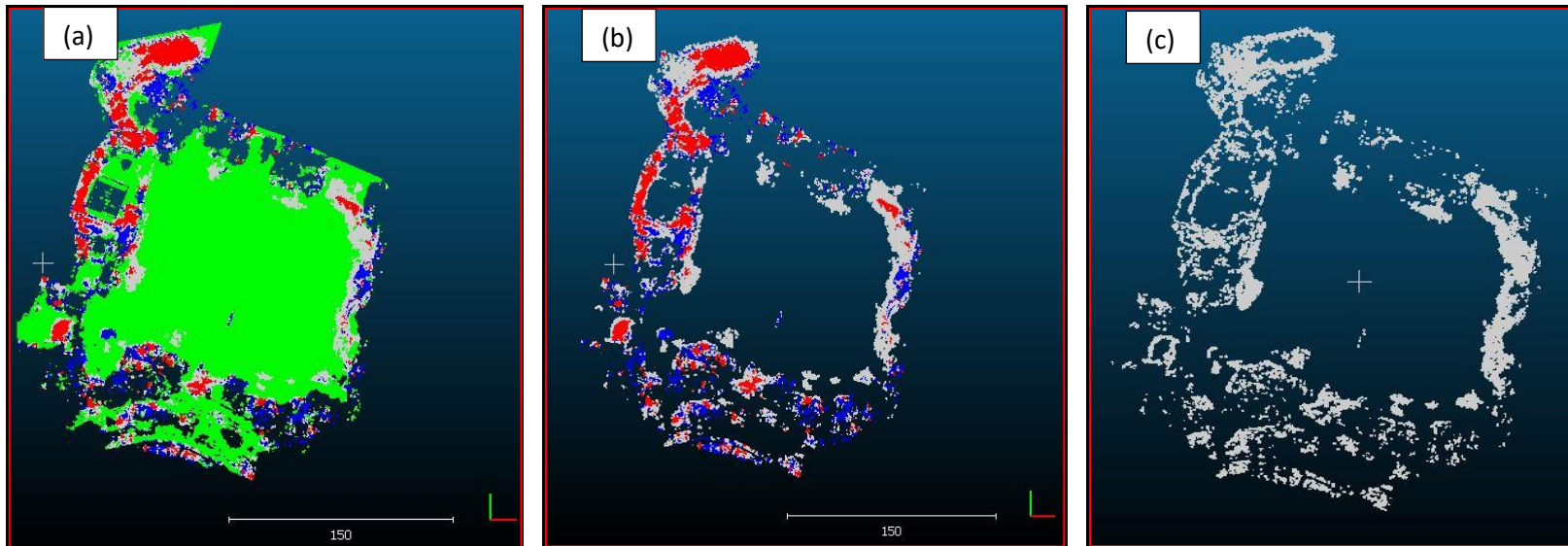
Figure 5-13: CANUPO classification results: (a) Classification of the entire study area, (b) Classification of High vegetation and Building, (c) Unclassified points
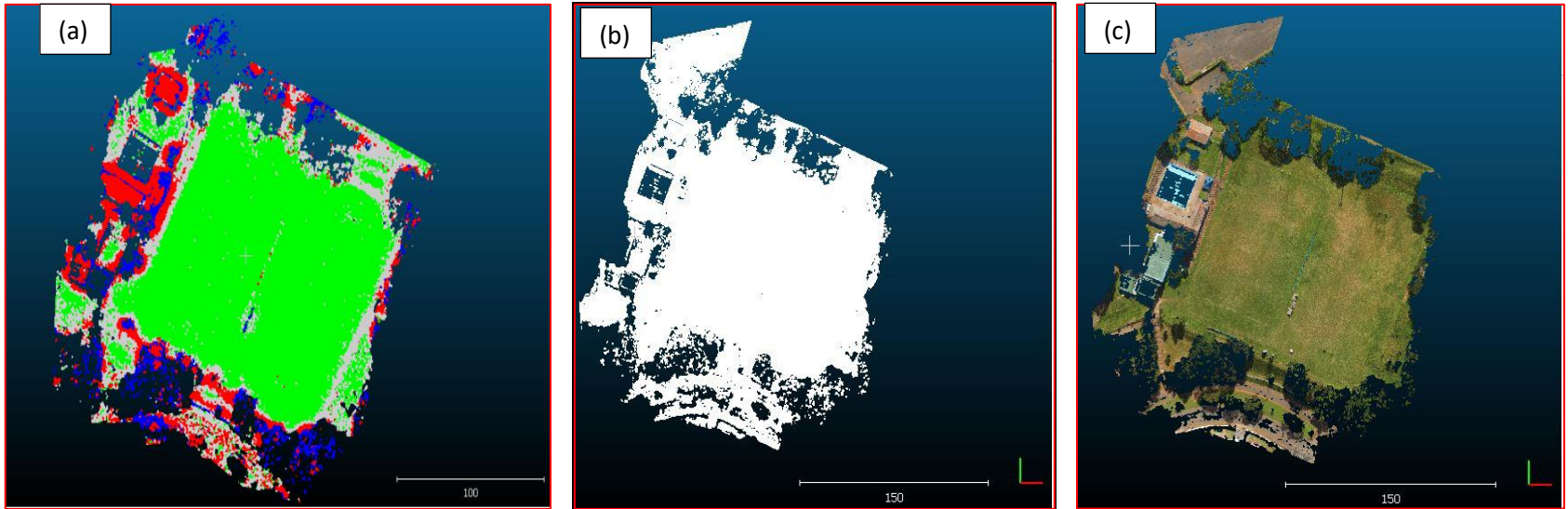
Figure 5-14: (a) Classified point cloud, (b) Unclassified raw point cloud, (c) Unclassified RGB point cloud

The classification procedure showing the number of points (in percentage) filtered is shown in Figure 5-15. Classifier A successfully filtered 78.1% of points, and 10.8% were not classified. The remainder of points belonging to 'not ground' was further passed to the second classifier, classifier B. 2.8% and 6.1% of points were classified as high vegetation and building, respectively. The remaining unclassified points amounted to 2.2%.
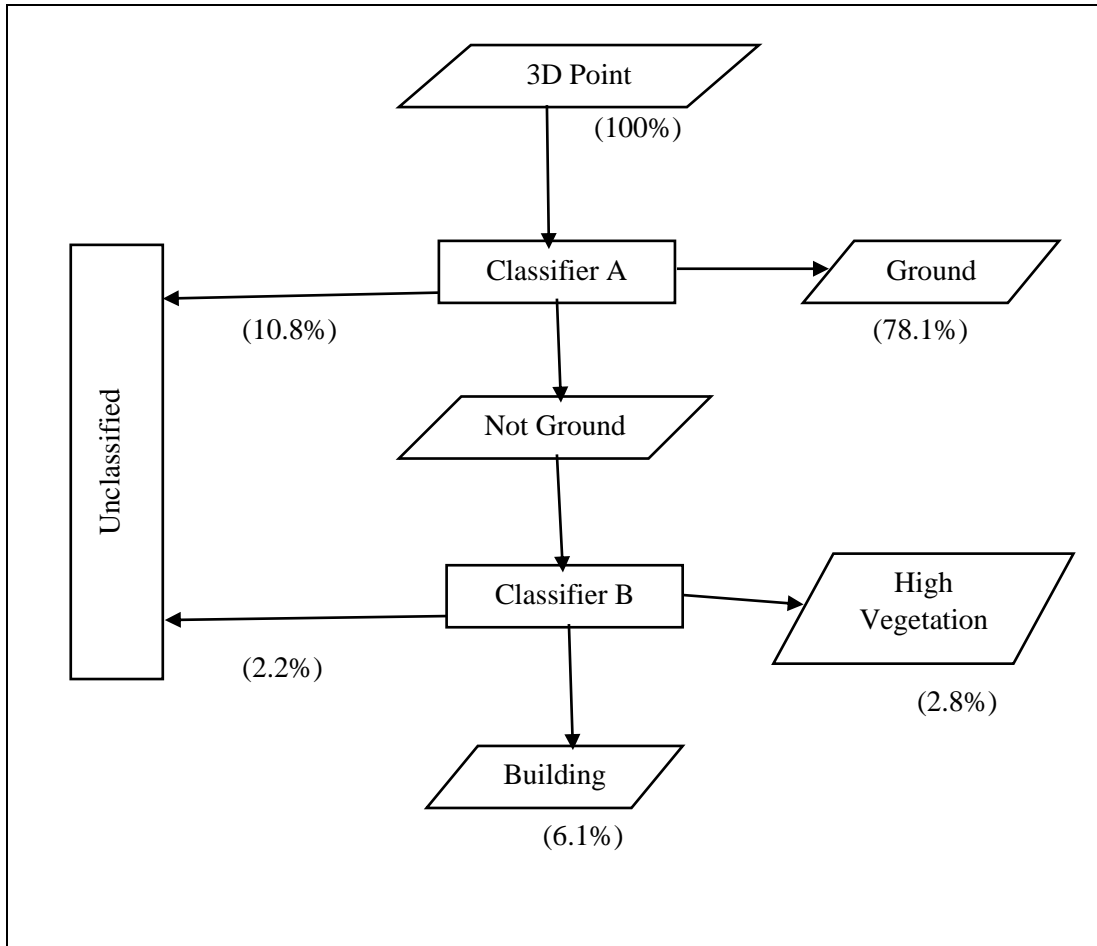
Figure 5-15: CANUPO Classification results in percentage

The point clouds produced using the SfM technique, both from the Pix4DMapper and WebODM software, appeared to have discontinuities. Some points were isolated, resulting in uncertainties concerning the geometry of objects. A total of 13.0% of points were not allocated to any class. In most cases, the unclassified points were situated in sites where a possible intermediate land cover category was observed. For example, the high vegetation and ground categories are separable. However, the high grass on the site appeared unclassified, and in some cases, it was categorized as either ground or high vegetation. Another similar occurrence appeared whereby steps were unclassified or either classified as ground or building category.

5.5   Summary

The camera calibration results showed that the UAV camera could be used as a measuring device. Thus, the UAV imagery was used to generate a 3D point cloud using the SfM technique. Pix4DMapper resulted in good unsupervised classification results. However, misclassifications were dominant in some land cover categories. The results of CANUPO classification were satisfactory, with some misclassifications around the edges where different categories appeared to overlap. Possible intermediate classes were observed whereby the CANUPO classifiers could not allocate the land cover type to any defined classes.

CHAPTER 6

DISCUSSION

6.1 Introduction

In this chapter, the results and analysis are explained in detail. The results from the calibration of the camera lens are discussed. Comparison and analysis are made between Pix4DMapper and WebODM software in performing the SfM technique towards generating a 3D point cloud. Finally, the possible rationales for outcomes achieved from the classification of points are explained.

6.2 UAV Camera Calibration

The MATLAB calibration toolbox is equipped with numerous functions, including a function that automatically detects the grid corners between the chessboard squares. The manual identification of grid corners improved the calibration results. Figure 6-1 shows a graphical presentation of a complete distortion model. This distortion model combines both the radial and tangential components of distortion. The numerical values of radial and tangential distortion coefficients were negligible after the initial optimization of camera parameters.
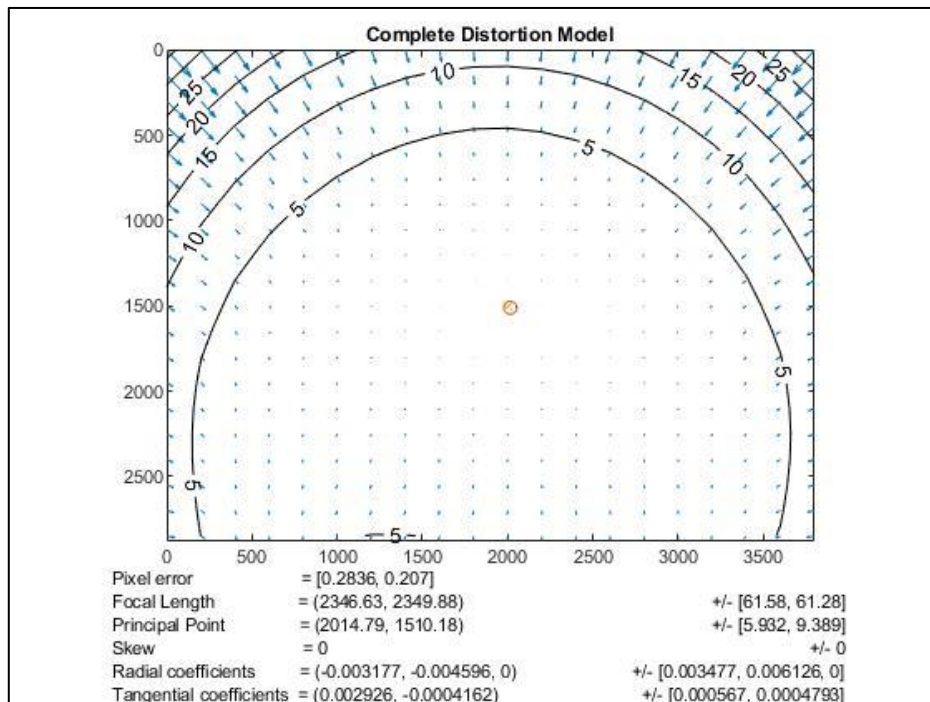
Figure 6-1: Complete distortion model

The intrinsic parameters of the camera lens resulted in the focal length of 3.6397mm +/- 0.0952mm, which is almost 3.61mm, as described in the specifications of the camera. The value of the pixel error before optimization was found to be [0.28358 0.20695] pixels, which is very small. During the SfM process, images are calibrated through self-calibration in order to eliminate associated systematic blunders (Kocaman et al., 2006). The overall calibration process indicated an excellent state of the camera for use as a measuring device.

6.3 Point Cloud Generation and Georeferencing

SfM is time-efficient; 90 of 90 images were processed in less than an hour in Pix4DMapper. On the other side, WebODM consumed much more time, approximately five hours, to complete this process. Both software produced a 3D point cloud and other photogrammetric products, including a textured 3D mesh and an orthomosaic. The georeferencing process was performed at a later stage after the point clouds were generated. The natural GCPs were used for georeferencing. However, this choice of GCPs introduces difficulties since some points could not be easily identified on the actual point cloud.

Pix4DMapper has two georeferencing options: The first option allows the user to identify the GCPs and checkpoints on the point cloud. The other option involves direct georeferencing on images and re-optimization to produce a georeferenced cloud. The GCPs were transformed from the Hartebeesthoek94 Lo31 to the UTM Zone 36S coordinate system since Pix4DMapper recognizes the UTM system. Figure 6-2 (a) and figure 6-2 (b) show the positions of GCPs on the point cloud in Pix4DMapper. Some of these points were reserved for use as checkpoints. Figure 6-2 (a) shows a sparse point cloud, while figure 6-2 (b) shows a densified 3D point cloud. The configuration of GCPs was set to allow points to be distributed over the 3D scene. Good results were achieved with a mean Root-Mean-Square error of 0.032m at an average ground sampling distance of 2.46cm.

The CloudCompare software permits direct georeferencing on the point cloud. A Root-Mean-Square error of 0.053m was achieved using the natural 3D GCPs. The Hartebeesthoek94 Lo31 coordinate system was used for georeferencing. Figure 6-2 (c) shows the positions of GCPs and checkpoints on the 3D scene. The orientation of the point cloud appeared to have been rotated by 180º after georeferencing using the Hartebeesthoek94 Lo31 system.
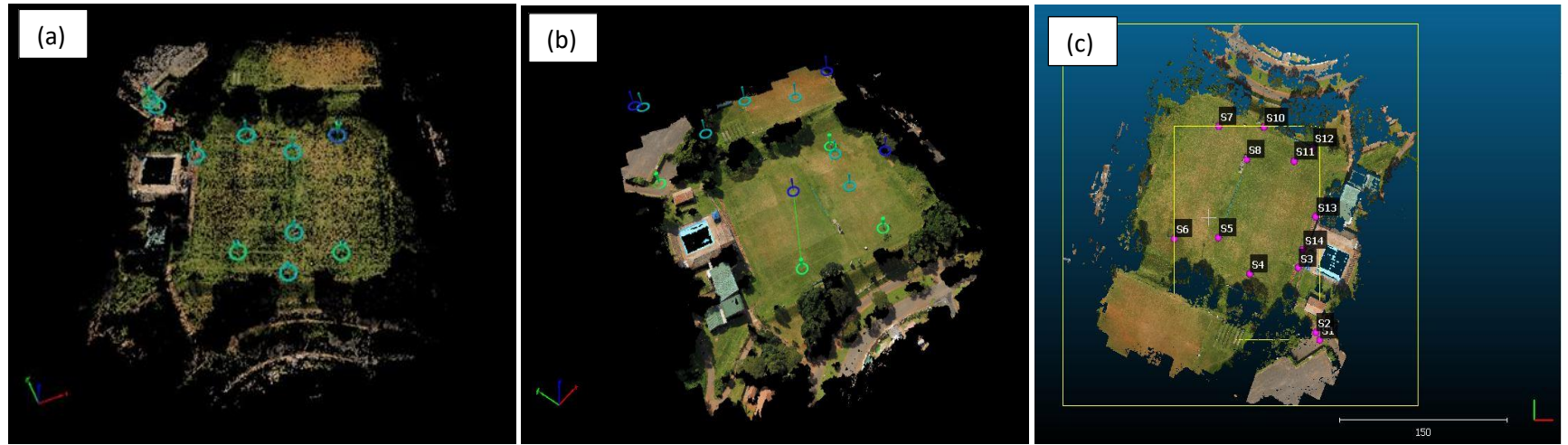
Figure 6-2: GCPs for Georeferencing: (a) Pix4DMapper (b) Pix4DMapper (c) CloudCompare

6.3.1 Point Cloud Classification

6.4.1 Discussion of Pix4DMapper Classification Results

The classification algorithm incorporated in Pix4DMapper was designed such that the user does not train the classifiers. This unsupervised classification technique was time-efficient, and the Pix4DMapper software is user-friendly. The qualitative assessment of accuracy indicated satisfactory overall classification results. It is also crucial to mention that errors of commission and omission were present in some land cover categories. The misclassifications were rectified by assigning the points manually into appropriate classes.

Most classes were dominated by a type I error. These classes included the road surface, high vegetation, building, and human-made object. The ground category was mainly affected by the type II error. The majority of points belonging to the road surface category were misclassified as ground. Classifiers can be site-specific; during classifiers' training, it is most likely that the samples for the road surface category were more or less similar to ground samples in terms of geometry or colour. This condition could also apply to other classes and introduce classification ambiguities. The classification algorithm proposed by Becker et al. (2017) may be utilized to mitigate classification ambiguities since it allows the user to define the classes. However, it will be incorporated in Pix4DMapper in the future.

6.4.2 Discussion of CANUPO Classification Results

The scales that were used to create classifiers were more or less similar. Numerous experiments were conducted to evaluate the behavior and find the best combination of scales. The objective was to provide a good value of the balanced accuracy for the two classes involved. While striving for a high balanced accuracy, which shows a good identification rate, the value of fdr was also aimed to be improved as this indicated how separable the classes were (Brodu and Lague, 2012).

Table 6-1 lists the range of scales that contributed to the development of classifiers. The properties of multiple scales of different land cover categories indicate that a particular class's dimensionality cannot be discriminated by a single scale (Brodu and Lague, 2012). Larger scales such as 30 and 50 contributed towards obtaining an improved value of fdr; however, these scales do not affect improving the actual classification (Brodu and Lague, 2012).

Table 6-1: Scales used for classifier development

Classifier A (m)	Classifier B (m)
0.04	0.1
0.1	0.5
0.5	1
1	1.5
1.5	2.5
5	5
8	8
10	10
15	15
20	20
30	30
50	50

The CANUPO plugin in CloudCompare allows the operator to specify the classification threshold before applying the classifier to a point cloud. It was noted that a classification threshold of 100% provided results with fewer points correctly classified for one particular class. The other class would then be associated with a Type I error. For example, classifier A separated ground from non-ground points; a classification threshold of 100% resulted in some of the ground points classified as non-ground. Lowering the classification threshold improved the results. The final threshold of 90% for classifier A was used to improve the classification results.

The second classifier, classifier B, was initially applied to the remainder of the point cloud with a classification threshold of 90%. Lowering the classification threshold to 85% resulted in more points being correctly classified. A general trend was observed when both classifiers were applied. Lowering the classification threshold improved the overall classification of the 3D scene. Caution must be taken when adjustments were performed to lower the classification threshold as this could introduce the errors of commission for particular land cover categories in question.

CloudCompare displays the CANUPO confidence level, which shows the performance of a classifier. Areas where a classifier produced good results, were indicated, including areas of misclassification. In figure 6-3, the classification confidences of classifiers used are presented.

Figure 6-3 (a) shows the results produced by classifier A. A graphical presentation of a color scale indicates the level of confidence ranging from 0.90 to 1.00. The amber color represents classification confidence of 100%, while violet indicates misclassifications. In this case, all points were identified as ground, but some are associated with some level of uncertainty. Figure 6-3 (b) shows the confidence level of points categorized as high vegetation obtained using classifier B. The color scale ranges from 0.80 to 1.00, with a high confidence level indicated by the red and low in blue. Lastly, figure 6-3 (c) shows the confidence level for the building category also obtained using classifier B. The color scale that ranges from 0.800 to 1.00 corresponds with red to amber. According to this figure, a few points were associated with low uncertainty for the building category.

The original article from which the CANUPO classification tool was documented employed a 3D point cloud acquired by means of a terrestrial laser scanner. The samples used in this article were available online and experiments were conducted in an attempt to learn and master the procedure of classifying a 3D scene. Two classes were defined: floor and vegetation. The 3D scene subject to classification comprised of the classes defined. The CANUPO classification outcomes by Brodu and Lague (2012) were excellent from a visual point of view, such that misclassifications were minimal. Zooming in to the classified scene indicated that few points were not classified in areas where an overlap of classes occurred. This research indicated that a similar phenomenon dominated around the edges of objects where a class overlap was noticed.

In contrast with the lidar 3D point cloud used by Brodu and Lague (2012), the 3D photogrammetric point cloud used in this research showed some discontinuities. This appeared to be a significant factor that contributed to misclassification in some classes. The dimensionality of objects is the main component of the CANUPO classification. Lidar points sampled from the 3D scene created robust classifiers. Besides, the best possible outcomes were achieved by extracting the training samples from the very same point cloud subject to classification.
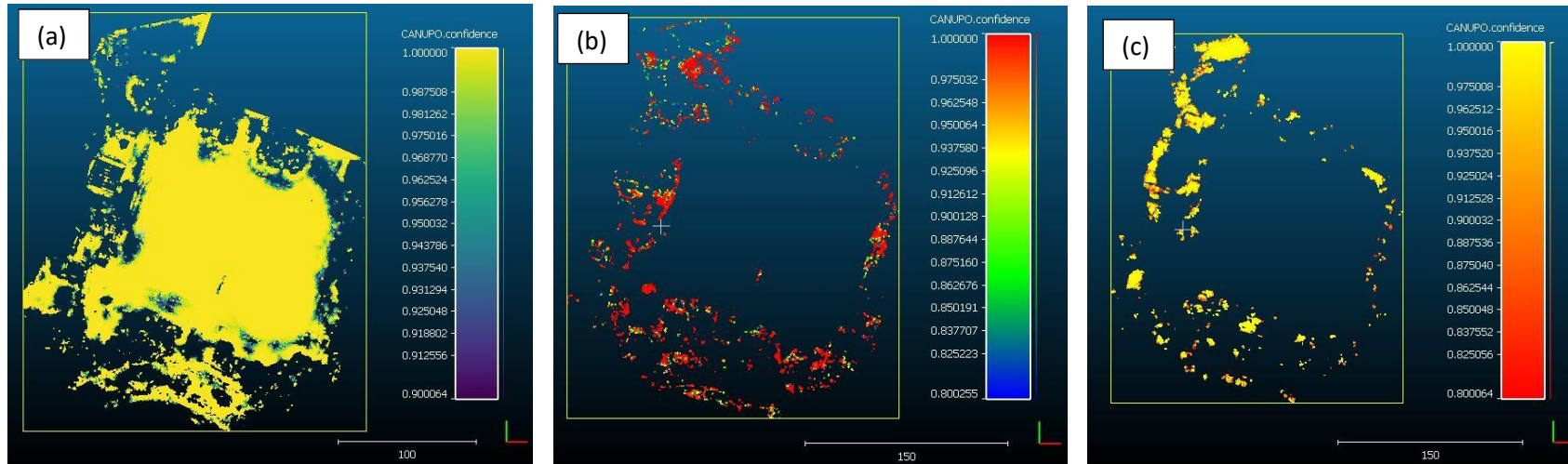
Figure 6-3: CANUPO Classification Confidence: (a) Ground, (b) High Vegetation, (c) Building

6.4 Accuracy Assessment

Both software, Pix4DMapper and CloudCompare (CANUPO) produced similar results when the correctness of classification was assessed qualitatively. However, the quantitative assessment was also conducted for CANUPO classification in CloudCompare. The associated errors of commission and omission are listed in table 6-2. The EC and EO for the ground category were 7.69% and 14.29%, respectively, which enabled this class to achieve excellent results. The high vegetation category obtained 18.18% in both EC and EO. The building category was associated with the highest EC and EO, 21.43% and 31.25%, respectively.

Table 6-2: Errors of Commission and Omission

| | | Reference Data | | | | |
		Ground	High Vegetation	Building	Sum	EC (%)
Classified Data	**Ground**	36	2	1	39	7.69
	High Vegetation	2	18	2	22	18.18
	Building	2	1	11	14	21.43
	Unclassified	2	1	2	5	
	Sum	42	22	16	80	
	EO (%)	14.29	18.18	31.25		

6.6   Summary

The photogrammetric products derived using the WebODM command line, which employed the SfM technique, were comparable to the commercial software's results, Pix4DMapper. The CloudCompare software was used to handle 3D data and address the classification problem using unsupervised and semi-supervised classification techniques. The positive outcomes obtained show that open-source software is sufficient to achieve robust photogrammetric products and solutions to the classification problem. The study area situated in the University of KwaZulu-Natal provided feature classes of diverse nature. The 3D photogrammetric point cloud classification using machine learning demonstrated the suitability of the CANUPO classification tool to filter various land cover categories in a complex 3D scene.

CHAPTER 7

CONCLUSION AND RECOMMENDATIONS

7.1 Introduction

In this chapter, a synopsis of solutions to the research problem is discussed briefly, providing a review of the aim and objectives of this research, including limiting factors and recommendations for future research and developments. Finally, the state of the art and other possible future applications of this research are examined.

7.2 Review of Objectives

7.2.1 Objective 1: Find the most suitable area of study, which comprises of different features to be utilized for point cloud classification.

Acquiring UAV images of the site situated at the University of KwaZulu-Natal was more efficient in traveling to and from the site. The most important factor was to identify objects to be classified in a 3D point cloud. This study area comprises different land cover categories, including but not limited to the ground, high vegetation, and building. The study area was accessible at any time, without any predicaments. This enabled a GPS survey and the verification of ground truth sites to be conducted with success.

7.2.2 Objective 2: Evaluate the state of the UAV payload, which is an RGB camera, through the process of camera calibration.

Radial and tangential components of distortion models provided negligible coefficients. In addition, the value of the pixel error was minimal. Negligible discrepancies were noticed in the camera lens parameters. The intrinsic parameters showed that the state of the UAV camera is almost perfect when the comparison was made between the results obtained and the manufacturer's specifications. The focal length of 3.6397mm +/- 0.0952mm was obtained from the calibration results, in contrast with 3.61mm as per specifications.

A pixel error of [0.28358, 0.20695] pixels indicated that the state of the camera was excellent. The conclusion drawn from the calibration results enables the imaging sensor to be utilized in photogrammetric applications. Since this technique is fundamental to applications in computer vision and robotics for navigation, this objective was achieved with success.

7.2.3 Objective 3: Generate a 3D point cloud using the Structure-from-Motion photogrammetric technique and georeference the resulting cloud.

Open-source WebODM software produced SfM products, which included a 3D point cloud. Positional information associated with each image acquired using a UAV played a vital role in the generation of a point cloud without GCPs. The resulting point cloud was based on the UTM Zone 36S coordinate system. The UTM coordinate system was transformed to the South African National Grid, which uses the WGS84 ellipsoid and a Hartebeesthoek94 datum. GCPs were surveyed in this South African coordinate system. The actual georeferencing of the point cloud and the orthomsaic was performed using the surveyed GCPs. CloudCompare software was used to georeference the 3D point cloud. The Orthomosaic was georeferenced in ArcMap. Root-mean-square errors of 0.053 and 0.032m were achieved, respectively, for the point cloud and orthomosaic. Thus, this objective was also achieved with success.

7.2.4 Objective 4: Perform the unsupervised and supervised classification techniques on the point cloud and evaluate the competence of classification.

The performance of two filtering algorithms was evaluated, the Pix4DMapper and CANUPO classification. Pix4DMapper is robust, and the software classified points within a short period of time. Misclassifications were rectified by the manual allocation of points to appropriate categories. Classifier training using the CANUPO tool was computationally fast. However, when the classifiers were applied to the entire 3D scene, the software utilized more time depending on the sub-sampling of points. Qualitative assessment analysis was conducted; both algorithms indicated similar results when common land cover categories were compared. The ground, high-vegetation and building classes were common in both cases. Ground and high vegetation were rated as good, while the building category was rated as fair. It was noticed that both algorithms achieved similar results, although they use different properties of points. Pix4DMapper uses the geometry and the reflectance of points, while the CANUPO tool uses only the dimensionality of points.

During the classifier training in CloudCompare, a balanced accuracy above 95% was achieved for all classifiers. The value of fdr obtained indicated a good separability of points. Further assessment was performed for the CANUPO classification in CloudCompare by employing quantitative analysis using the Kappa coefficient and error matrix. The overall accuracy of

classification was 81.3% and a Kappa value of 7.1, which indicates a substantial agreement. The success of classification performance evaluation enabled this objective to be achieved.

7.3 Review of the Aim

This study aimed to classify a 3D point cloud produced using UAV imagery and assess the accuracy of classification. Achieving all four objectives of this research contributed to accomplishing the aim and providing solutions to the research question. This study demonstrated how state-of-the-art and cost-effective SfM techniques play a vital role in achieving the abilities of a traditional laser scanner. The use of open-source CloudCompare software to train the classifiers using smaller samples and applying them to an unseen point cloud resulted in successful automatic classification of a 3D point cloud. The accuracy assessment was performed with success by employing a widely used method of developing a confusion matrix. The classified points were checked against the ground truth sites.

7.4 Limitations of the Research

The nadir images were captured during the flight mission. As a result, the point cloud generated from the SfM technique contained discontinuities around the edges of objects and some points were isolated. The 3D geometry of building facades and the side views could not be reconstructed in detail. The availability of the Pix4DMapper software was limited. Therefore, all the processing was performed in a finite period of time. The classification performed using Pix4DMapper produced acceptable results. However, the unsupervised technique does not allow the user to have an input in training the classifiers.

The main classification, which was performed using the CANUPO plugin in CloudCompare software, used the dimensionality of objects. Misclassifications occurred in cases where the geometry of objects could not be distinguished. For example, sharp edges with slopes on the ground were classified as buildings. The buildings where side views were not reconstructed were either ground or not allocated to any class. However, this was mitigated by using the best training samples at varying scales and maneuvering the classification threshold. The CANUPO is a binary classifier; filtering different classes is complicated, allowing only two classes at a time. The CloudCompare software crashed several times during the classification of points.

The use of the GPS instrument to verify the ground truth information was slightly interrupted by the loss of signal in cases where the points to be staked out were located between buildings

or under the trees. However, using a georeferenced and orthorectified mosaic of the entire study site assisted in the validation process.

7.5 Recommendations

Since the 3D point cloud generated using the SfM technique showed some discontinuities and isolated points, it is recommended that both nadir and oblique imagery are used to generate a point cloud. Part of the rationale behind misclassifications was the source of training samples. Experiments were conducted whereby the training samples were obtained from the same point cloud for testing. Excellent results were achieved with misclassifications at a minimum. Therefore, it is recommended that training samples be robust and associated with the same dimensionality as the objects to be classified. Further research on classifiers that accommodate multiple classes, including the integration of dimensionality and reflectance, is recommended for the CANUPO classification module in CloudCompare.

7.6 State of the Art and Future Applications

Point cloud classification has been used in a wide range of applications. Numerous examples have been discussed in the second chapter, the literature review. Possible applications may differ based on the accuracy. The common uses of point cloud classification include engineering and construction, where non-ground points are filtered from ground points for the generation of contours. New site developments often require the audit of land; classified points may be utilized in the decision-making for urban and regional planning. The outcomes of this research indicated that point cloud classification could be performed for monitoring purposes, including but not limited to farming, engineering, and visualization towards planning and decision-making.

7.7 Concluding Remarks

The outcomes of this research indicated that 3D point clouds generated from UAV imagery could be classified using open-source software. This promotes the recognition of the cost-effective SfM technique and free software in engineering, robotics, and other environmental management applications where thematic mapping is used towards decision-making. The CANUPO classification plugin incorporated in CloudCompare software achieved satisfactory results. The heterogeneity of the University of KwaZulu-Natal sports field (Howard College) showed that complex 3D environments could be classified into different land cover categories.

REFERENCES

Abmayr, T., Härtl, F., Reinköster, M. and Fröhlich, C., 2005. Terrestrial laser scanning: Applications in cultural heritage conservation and civil engineering. In *Proceedings of the ISPRS working group V4.*

Akca, D., 2003. *Full automatic registration of laser scanner point clouds*. ETH Zurich.

Al-Doski, J., Mansorl, S. B. and Shafri, H.Z.M., 2013. Image classification in remote sensing. *Department of Civil Engineering, Faculty of Engineering, University Putra, Malaysia*, *3*(10).

Alonso, V., 2019. A crash course in AI-driven object detection, Position IT, EE Publishers (PTY) Ltd.

Antonarakis, A. S., Richards, K. S. and Brasington, J., 2008. Object-based land cover classification using airborne LiDAR. *Remote Sensing of environment*, *112*(6), pp.2988-2998.

Arya, S., Mount, D. M., Netanyahu, N. S., Silverman, R. and Wu, A. Y., 1998. An optimal algorithm for approximate nearest neighbor searching fixed dimensions. *Journal of the ACM (JACM)*, *45*(6), pp.891-923.

Autodesk, 2018. *About Working with Point Clouds*. [Online]. Available: https://knowledge.autodesk.com/support/autocad/learn-explore/caas/CloudHelp/cloudhelp/2018/ENU/AutoCAD-Core/files/GUID-C0C610D0-9784-4E87-A857-F17F1F7FEEBE-htm.html [Accessed 04 May 2019].

Becker, C., Häni, N., Rosinskaya, E., d'Angelo, E. and Strecha, C., 2017. Classification of aerial photogrammetric 3D point clouds. *arXiv preprint arXiv:1705.08374*.

Berjón, D., Pagés, R. and Morán, F., 2016. Fast feature matching for detailed point cloud generation. In *2016 Sixth International Conference on Image Processing Theory, Tools and Applications (IPTA)* (pp. 1-6). IEEE.

Bonneau, D. A. and Hutchinson, D. J., 2019. The use of terrestrial laser scanning for the characterization of a cliff-talus system in the Thompson River Valley, British Columbia, Canada. *Geomorphology*, *327*, pp.598-609.

Bouguet, J., 2015. *Camera Calibration Toolbox for Matlab*. [Online]. Available: http://www.vision.caltech.edu/bouguetj/calib_doc/htmls/parameters.html [Accessed 14 July 2019]

Boulch, A., Le Saux, B. and Audebert, N., 2017. Unstructured Point Cloud Semantic Labeling Using Deep Segmentation Networks. *3DOR*, *2*, pp.7.

Breiman, L., 2001. Random forests. *Machine learning*, *45*(1), pp.5-32.

Brennan, R. and Webster, T. L., 2006. Object-oriented land cover classification of lidar-derived surfaces. *Canadian journal of remote sensing*, *32*(2), pp.162-172.

Briem, G. J., Benediktsson, J. A. and Sveinsson, J. R., 2002. Multiple classifiers applied to multisource remote sensing data. *IEEE transactions on geoscience and remote sensing*, *40*(10), pp.2291-2299.

Brodu, N. and Lague, D., 2012. 3D terrestrial lidar data classification of complex natural scenes using a multi-scale dimensionality criterion: Applications in geomorphology. *ISPRS Journal of Photogrammetry and Remote Sensing*, *68*, pp.121-134.

Campbell, J. B. 2002. *Introduction to Remote Sensing*: Taylor & Francis.

Campbell, J. B. and Wynne, R. H., 2011. *Introduction to remote sensing*. Guilford Press.

Canty, M. J., 2014. *Image analysis, classification and change detection in remote sensing: with algorithms for ENVI/IDL and Python*. Crc Press.

Chief Directorate: National Geo-Spatial Information, 2019. *Coordinate Conversion Utility*. [Online]. Available: http://www.ngi.gov.za [Accessed 17 June 2020].

Chehata, N., Guo, L. and Mallet, C., 2009. Airborne lidar feature selection for urban classification using random forests. In *Laserscanning*.

Cignoni, P., Callieri, M., Corsini, M., Dellepiane, M., Ganovelli, F. and Ranzuglia, G., 2008. Meshlab: an open-source mesh processing tool. In *Eurographics Italian chapter conference* Vol. 2008, pp. 129-136.

Colomina, I. and Molina, P., 2014. Unmanned aerial systems for photogrammetry and remote sensing: A review. *ISPRS Journal of photogrammetry and remote sensing*, *92*, pp.79-97.

Chief Surveyor-General, 2001. *Property Search*. [Online]. Available:
http://csg.dla.gov.za/esio/listdocument.jsp [Accessed 11 August 2019].

De Morsier, F., Alonso, V., and Nguyen, L. 2019. AI-powered Object Detection as a Mapping-business Accelerator. *The Global Magazine for Geomatics, 33,* pp.45-47.

Demirel, A. S., Akdeniz, H. and Aksu, O., 2004. Two functional software for internal use; flight planning and presenting of digital orthophotos. In *International Archives of Photogrammetry 35; 344-347 International Congress for Photogrammetry and Remote Sensing; ISPRS XXth Congress 20th, International Congress for Photogrammetry and Remote Sensing*, pp.1682-1750.

DJI, 2017. *Phantom 3 Specs*. [Online]. Available: https://www.dji.com/phantom [Accessed 30 June 2020].

Eling, C. and Klingbeil, L., 2015. UAV real-time. Data use in a lightweight direct georeferencing system. *GPS World*, *44*, pp.55.

Engels, C., Stewénius, H. and Nistér, D., 2006. Bundle adjustment rules. *Photogrammetric computer vision*, *2*(32).

Erdas Imagine. 2010. *Erdas Field Guide*. United States of America. Erdas Inc.

Farella, E. (2016). *3D mapping of underground environments with a hand-held laser scanner*. [Online]. Available: https://www.researchgate.net/publication/318368305 [Accessed 06 November 2019].

Fetić, A., Jurić, D. and Osmanković, D., 2012, May. The procedure of a camera calibration using Camera Calibration Toolbox for MATLAB. In *2012 Proceedings of the 35th International Convention MIPRO* (pp. 1752-1757). IEEE.

Foody, G.M., 2002. Status of land cover classification accuracy assessment. *Remote sensing of environment*, *80*(1), pp.185-201.

Friedman, J., Hastie, T. and Tibshirani, R., 2001. *The elements of statistical learning* (Vol. 1, No. 10). New York: Springer series in statistics.

Garcia, M. V. Y. and Oliveira, H. C., 2020. The Influence of Ground Control Points Configuration and Camera Calibration for DTM and Orthomosaic Generation Using Imagery

Obtained from a Low-Cost Uav. *ISPRS Annals of Photogrammetry, Remote Sensing & Spatial Information Sciences*, *5*(1), pp.239-244.

Geavis, 2020. *Why GCPs are Needed in Photogrammetry?* [Online] available at: https://www.geavis.si [Accessed 20 August, 2020].

Gevaert, C. M., Persello, C. and Vosselman, G., 2016. Optimizing multiple kernel learning for the classification of UAV data. *Remote Sensing*, *8*(12), pp.1025.

GIM, 2019. Lidar Technology for Game of Thrones. *The Global Magazine for Geomatics, 33,* pp.12.

GitHub, 2019. *Getting Started*. [Online] available at: https://github.com/OpenDroneMap/WebODM/ [Accessed 08 April, 2019].

Grilli, E., Menna, F. and Remondino, F., 2017. A review of point clouds segmentation and classification algorithms. *The International Archives of Photogrammetry, Remote Sensing and Spatial Information Sciences*, *42*, pp.339.

Guo, B., Huang, X., Zhang, F. and Sohn, G., 2015. Classification of airborne laser scanning data using JointBoost. *ISPRS Journal of Photogrammetry and Remote Sensing*, *100*, pp.71-83.

Huang, J. and You, S., 2016, December. Point cloud labeling using 3d convolutional neural network. In *2016 23rd International Conference on Pattern Recognition (ICPR)* (pp. 2670-2675). IEEE.

ICAO., 2011. *Unmanned Aerial Systems (UAS)*. Canada: International Civil Aviation Authority.

Juea, L., 2008. Research on close-range photogrammetry with big rotation angle. *aa*, *1*, pp.1.

Kamavisdar, P., Saluja, S. and Agrawal, S., 2013. A survey on image classification approaches and techniques. *International Journal of Advanced Research in Computer and Communication Engineering*, *2*(1), pp.1005-1009.

Keuchel, J., Naumann, S., Heiler, M. and Siegmund, A., 2003. Automatic land cover analysis for Tenerife by supervised classification using remotely sensed data. *Remote sensing of environment*, *86*(4), pp.530-541.

Kocaman, S., Zhang, L. and Gruen, A., 2006, January. Self-calibrating triangulation of airborne linear array CCD cameras. In *EuroCOW 2006 International Calibration and Orientation Workshop, Castelldefels, Spain*,Vol. 25, pp.27.

Kumar, A., Anders, K., Winiwarter, L. and Höfle, B., 2019. Feature relevance analysis for 3D point cloud classification using deep learning. *ISPRS Annals of Photogrammetry, Remote Sensing & Spatial Information Sciences*, *4*.

Lillesand, T., Kiefer, R. W. and Chipman, J., 2015. *Remote sensing and image interpretation*. John Wiley & Sons.

Liu, K. and Boehm, J., 2015. Classification of big point cloud data using cloud computing. *ISPRS-International Archives of the Photogrammetry, Remote Sensing and Spatial Information Sciences*, *40*, pp.553-557.

Lu, D. and Weng, Q., 2007. A survey of image classification methods and techniques for improving classification performance. *International journal of Remote sensing*, *28*(5), pp.823-870.

Lutz, M., 2001. *Programming python*. O'Reilly Media, Inc.

Mahami, H., Nasirzadeh, F., Hosseininaveh Ahmadabadian, A. and Nahavandi, S., 2019. Automated progress controlling and monitoring using daily site images and building information modelling. *Buildings*, *9*(3), p.70.

McHugh, M. L., 2012. Interrater reliability: the kappa statistic. *Biochemia medica*, *22*(3), pp.276-282.

Michelleti, N., Chandler, J. H. and Lane, S., 2015. Structure from motion (SFM) photogrammetry. *Geomorphological Techniques*.

Morgan, J. L., Gergel, S. E. and Coops, N. C., 2010. Aerial photography: a rapidly evolving tool for ecological management. *BioScience*, *60*(1), pp.47-59.

Moulon, P. and Bezzi, A., 2011, June. Python photogrammetry toolbox: a free solution for three-dimensional documentation. In *ArcheoFoss* (pp. 1-12).

Nedevschi, S., Marita, T., Vaida, M., Danescu, R., Frentiu, D., Oniga, F., Pocol, C. and Moga, D., 2002. Camera Calibration Method for Stereo Measurements. *Journal of Control Engineering and Applied Informatics (CEAI)*, *4*(2), pp.21-28.

Nevalainen, O., Honkavaara, E., Tuominen, S., Viljanen, N., Hakala, T., Yu, X., Hyyppä, J., Saari, H., Pölönen, I., Imai, N. N. and Tommaselli, A. M., 2017. Individual tree detection and classification with UAV-based photogrammetric point clouds and hyperspectral imaging. *Remote Sensing*, *9*(3), pp.185..

Nguyen, T.T., Kluckner, S., Bischof, H. and Leberl, F., 2010. *Aerial photo building classification by stacking appearance and elevation measurements*. Graz University of Technology, Austria

Niemeyer, J., Rottensteiner, F. and Soergel, U., 2012. Conditional random fields for lidar point cloud classification in complex urban areas. *ISPRS Ann. Photogrammetry. Remote Sens. Spat. Inf. Sci*, *1*(3), pp.263-268.

Paine, D. P. and Kiser, J. D., 2003. Aerial photography and image interpretation, 2nd ed. Hoboken.

Picterra, 2019. *AI-Powered Object Detection as Mapping-business Accelerator*. [Online]. Available: www.picterra.ch [Accessed 02 December 2019].

Pix4D, 2017. *Machine Learning Meets Photogrammetry*. [Online]. Available: https://www.pix4d.com [Accessed 21 April 2020].

Pix4DSA, 2019. *How To Generate The Point Cloud Classification*. [Online]. Available: https://www.pix4d.com [Accessed 13 July 2020].

Pix4DSA, 2019. *Measure from Images*. [Online]. Available: https://www.pix4d.com [Accessed 13 July 2020].

Pouncey, R., Swanson, K. and Hart, K., 1999. ERDAS field Guide Fifth Edition, Revised and Expanded, ERDAS Field Guide™ Copyright, ERDAS® Inc. *All rights reserved*.

Price, K. P., Guo, X. and Stiles, J. M., 2002. Optimal Landsat TM band combinations and vegetation indices for discrimination of six grassland types in eastern Kansas. *International Journal of Remote Sensing*, *23*(23), pp.5031-5042.

Quattrochi, D. A., and Goodchild, M. F., 1997. *Scale in remote sensing and GIS*: CRC press.

Reinoso, J.F., Moncayo, M. and Barrera, D., 2014. Close-range photogrammetry applied to the documentation of cultural heritage using telescopic and wide-angle lenses. *The Imaging Science Journal*, *62*(7), pp.387-394.

Remondino, F., Nocerino, E., Toschi, I. and Menna, F., 2017. A critical review of automated photogrammetric processing of large datasets. *International Archives of the Photogrammetry, Remote Sensing & Spatial Information Sciences*, *42*.

Rodríguez, A. S., Rodríguez, B. R., Rodríguez, M. S., & Sánchez, P. A., 2019. Laser scanning and its applications to damage detection and monitoring in masonry structures. In *Long-term Performance and Durability of Masonry Structures* (pp. 265-285): Elsevier.

Roynard, X., Deschaud, J. E. and Goulette, F., 2018. Classification of point cloud scenes with multiscale voxel deep network. *arXiv preprint arXiv:1804.03583*.

Congalton, R. G., Plourde, L. and Bossler, J., 2002. Quality assurance and accuracy assessment of information derived from remotely sensed data. *Manual of geospatial science and technology*, pp.349-361.

South African Civil Aviation Authority, 2017. *Remotely Piloted Aircraft Systems*. [Online]. Available: http://www.caa.co.za [Accessed 08 February 2020].

Schowengerdt, R. A., 2007. *Remote sensing, models, and methods for image processing*, 3rd ed. Burlington, MA: Academic Press.

Shakhatreh, H., Sawalmeh, A. H., Al-Fuqaha, A., Dou, Z., Almaita, E., Khalil, I., Othman, N. S., Khreishah, A. and Guizani, M., 2019. Unmanned aerial vehicles (UAVs): A survey on civil applications and key research challenges. *Ieee Access*, *7*, pp.48572-48634.

Shotton, J., Johnson, M. and Cipolla, R., 2008. Semantic texton forests for image categorization and segmentation. In *2008 IEEE conference on computer vision and pattern recognition* (pp. 1-8). IEEE.

Singh, K., 2013. *Change detection of invasive bracken fern (Pteridium aquilinum [L.] Kuhn) in the Royal Natal National Park and Rugged Glen Nature Reserve.* Degree of MSc, University of KwaZulu-Natal.

Sithole, G. and Vosselman, G., 2004. Experimental comparison of filter algorithms for bare-Earth extraction from airborne laser scanning point clouds. *ISPRS journal of photogrammetry and remote sensing*, *59*(1-2), pp.85-101.

Snavely, N., 2008. Bundler: Structure from motion (sfm) for unordered image collections. *http://phototour. cs. washington. edu/bundler/*.

Snavely, N., Seitz, S. M. and Szeliski, R., 2006. Photo tourism: exploring photo collections in 3D. In *ACM siggraph 2006 papers*, pp.835-846.

Song, J. H., Han, S. H., Yu, K. Y. and Kim, Y. I., 2002. Assessing the possibility of land-cover classification using lidar intensity data. *International archives of photogrammetry remote sensing and spatial information sciences*, *34*(3/B), pp.259-262.

Spetsakis, M. and Aloimonos, J. Y., 1991. A multi-frame approach to visual motion perception. *International Journal of Computer Vision*, *6*(3), pp.245-255.

Story, M. and Congalton, R.G., 1986. Accuracy assessment: a user's perspective. *Photogrammetric Engineering and remote sensing*, *52*(3), pp.397-399.

Theodoridis, S., and Koutroumbas, K., 2009. *Pattern recognition*. 4th ed. Academic Press, Inc.

Thompson, I. D., Maher, S. C., Rouillard, D. P., Fryxell, J. M. and Baker, J. A., 2007. Accuracy of forest inventory mapping: Some implications for boreal forest management. *Forest Ecology and Management*, *252*(1-3), pp.208-221.

Turner, M. G., Gardner, R. H., O'neill, R. V. and O'Neill, R. V., 2001. *Landscape ecology in theory and practice* (Vol. 401). Springer New York.

Uebersax, J. S., 1982. A generalized kappa coefficient. *Educational and Psychological Measurement*, *42*(1), pp.181-183.

Van Genechten, B., 2008. *Theory and practice on Terrestrial Laser Scanning: Training material based on practical applications*. Universidad Politecnica de Valencia Editorial; Valencia, Spain.

Venkateswaran, C. J., Vijaya, R. and Saravanan, A. M., 2013. A fuzzy based approach to classify remotely sensed images. *International Journal of Engineering and Technology*, *5*(3), pp.3051-3055.

Verykokou, S. and Ioannidis, C., 2018. A photogrammetry-based Structure-from-Motion algorithm using robust iterative bundle adjustment techniques. *ISPRS Annals of Photogrammetry, Remote Sensing & Spatial Information Sciences*, *4*.

Viera, A. J. and Garrett, J. M., 2005. Understanding interobserver agreement: the kappa statistic. *Fam med*, *37*(5), pp.360-363.

WebODM, 2019. *Drone Mapping Software*. [Online] Available at: https://www.opendronemap.org/webodm [Accessed 14 April, 2019]

Weinmann, M., Jutzi, B., Hinz, S. and Mallet, C., 2015. Semantic point cloud interpretation based on optimal neighborhoods, relevant features and efficient classifiers. *ISPRS Journal of Photogrammetry and Remote Sensing*, *105*, pp.286-304.

Weinmann, M., Jutzi, B. and Mallet, C., 2013. Feature relevance assessment for the semantic interpretation of 3D point cloud data. *ISPRS Annals of the Photogrammetry, Remote Sensing and Spatial Information Sciences*, *5*(W2), p.1.

Westoby, M. J., Brasington, J., Glasser, N. F., Hambrey, M. J. and Reynolds, J. M., 2012. 'Structure-from-Motion'photogrammetry: A low-cost, effective tool for geoscience applications. *Geomorphology*, *179*, pp.300-314.

Wolf, P. R., Dewitt, B. A. and Wilkinson, B. E., 2014. *Elements of Photogrammetry with Applications in GIS*. McGraw-Hill Education.

Wulf, O. and Wagner, B., 2003. July. Fast 3D scanning methods for laser measurement systems. In *International conference on control systems and computer science (CSCS14),* pp. 2-5.

Yi, L., Shao, L., Savva, M., Huang, H., Zhou, Y., Wang, Q., Graham, B., Engelcke, M., Klokov, R., Lempitsky, V. and Gan, Y., 2017. Large-scale 3d shape reconstruction and segmentation from shapenet core55. *arXiv preprint arXiv:1710.06104*.

Zhang, Z., 2000. A flexible new technique for camera calibration. *IEEE Transactions on pattern analysis and machine intelligence*, *22*(11), pp.1330-1334.

Zogg, H. M. and Ingensand, H., 2008. Terrestrial laser scanning for deformation monitoring: Load tests on the Felsenau Viaduct (CH). *International Archives of the Photogrammetry, Remote Sensing and Spatial Information Sciences*, *37*(B5), pp.555-562.

APPENDICES

Appendix A

Projection parameters, transformation matrix and image coordinates generated by the GPS on-board during the UAV flight mission. Information from WebODM results.

Projection

+ proj = utm + zone = 36 + south + datum = WGS84 + units = m + no_defs + type = crs

Transformation Matrix

[0.9999140,   -0.0175281,   0.0000000,   305313.4097332]
[0.0175281,   0.9999140,   0.0000000,   6693779.8812277]
[0.0000001,   0.0000001,   1.0000000,   0.0000000]
[0.0000000,   0.0000000,   0.0000000,   1.0000000]

Coordinates

WGS84 UTM 36S

	305313	6693779	
1.	40.2559044856	-120.964646861	66.374
2.	-69.9355937717	-86.9853610359	66.374
3.	70.9911349228	-73.0917099789	66.674
4.	73.9378081069	10.577974719	66.674
5.	-15.5470801521	113.983378986	66.574
6.	-10.5100202796	47.4482430406	66.574
7.	33.0273894995	70.6234858446	66.774
8.	-74.6802684331	-88.2666317541	66.474
9.	113.497774656	23.9139100416	66.274
10.	-40.1492237757	-99.6787179299	66.574
11.	38.2153974032	4.6484448798	66.474
12.	21.3601916679	-32.9686634615	66.574
13.	62.5804196406	61.3043458937	66.374
14.	-65.4155267352	-0.799447099678	66.574

15.	69.8597660286	75.4144417327	66.474
16.	-19.0548731763	28.2094985647	66.474
17.	55.4050741951	-31.4942196766	66.474
18.	101.172593991	72.2826644247	66.574
19.	11.3397098475	95.6829645447	66.574
20.	41.7420031778	89.9852698902	66.374
21.	71.9749397165	83.0741441334	66.574
22.	99.2316036088	75.5163824335	66.474
23.	-73.2335609437	58.8342424231	66.374
24.	-11.7700790224	-108.202056067	66.174
25.	-28.3481709746	83.0497212745	66.574
26.	63.0645937466	-90.3946468644	66.374
27.	36.7547179472	-73.2790126111	66.574
28.	-2.13480772945	66.412977336	66.374
29.	-52.8467187811	-48.0211687777	66.574
30.	-46.9713171498	40.9418785255	66.474
31.	83.233863408	31.8378652558	66.774
32.	-44.397261115	-28.7070641341	66.374
33.	-93.9721520097	-63.1376241259	66.774
34.	-56.2502780743	20.0979428422	66.574
35.	130.932882913	63.5398305235	66.574
36.	54.8815570826	43.8698886484	66.374
37.	-51.9787684269	106.541256659	66.474
38.	96.2698523873	-15.1201666277	66.374
39.	87.6762439914	-35.4129856527	66.574
40.	-93.7613416546	-81.5853556283	66.574
41.	-58.1095237365	92.3002991192	66.274
42.	-84.5331495026	-42.2446399042	66.574
43.	-121.707790098	-50.759532623	66.574
44.	20.2057213687	-115.800059056	66.674
45.	-45.6329312439	118.007950237	66.574
46.	-96.2880479476	5.85369031038	66.474
47.	-36.0752632704	-9.62311266363	66.474
48.	-113.686690268	-33.1991599947	66.774
49.	-65.3916715849	76.0618791236	66.374

50.	-80.687047955	41.8074403275	66.374
51.	-61.4523423372	-67.6121282279	66.374
52.	-32.2416818878	-76.0962006655	66.574
53.	-27.7015168761	9.1137135271	66.574
54.	-20.0138642942	-104.798589572	66.174
55.	105.178032101	5.29826857615	66.374
56.	64.6629744542	-10.5121628791	66.574
57.	23.7814798956	49.7216921933	66.674
58.	14.6864332951	28.6377407871	66.574
59.	79.0556429049	-54.7761710826	66.374
60.	12.9517503437	102.335988555	66.774
61.	-22.6838479957	-55.3921435755	66.474
62.	3.66266406345	-73.0582982842	66.474
63.	54.8967027435	-108.474864986	66.274
64.	46.1433952849	-52.4116765652	66.474
65.	82.5122156848	79.9171389602	66.574
66.	-101.283184091	-78.178524036	66.574
67.	40.7440324677	95.160414814	66.574
68.	-19.0996009636	104.102521747	66.574
69.	-13.3141676822	-34.3649316281	66.574
70.	92.4124544971	52.7569028465	66.574
71.	-128.874495263	-67.1407391643	66.174
72.	-37.5880049577	61.9601048743	66.574
73.	-105.068844847	-14.0021639634	66.474
74.	-40.8532528997	-95.3484639768	66.574
75.	-74.7437179211	-21.2808445226	66.574
76.	29.9240163486	-13.8928497098	66.274
77.	-5.10252386413	-92.7382423375	66.674
78.	5.68617405102	83.4615574842	66.374
79.	27.4643863842	-93.4763072524	66.774
80.	12.6412999772	-53.1497929245	66.674
81.	46.632208126	23.9988509668	66.374
82.	-27.7875340617	117.061158689	66.474
83.	23.8029808087	99.6465177713	66.674
84.	5.36594954645	7.7068997696	66.574

85.	47.9628605641	-124.217412001	66.274
86.	-44.5479773728	121.80595612	66.474
87.	-4.00553464232	-13.2217663694	66.674
88.	127.300199528	55.9305546191	66.674
89.	-87.862640397	25.0072544832	66.374
90.	19.0970347361	-112.271498829	66.374

Appendix B

GPS calibration sheet
System: WG31
Base: VRS

	Control Point	Biesheuvel (TR621)	Rekaju (TR99)
	Description	Trigonometrical Beacon	Trigonometrical Beacon
Current Survey	**Y**	2370.60	4980.63
	X	3305783.88	3305655.67
	Z	129.83	140.35
Published Values	**Y**	2370.59	4980.62
	X	3305783.89	3305655.67
	Z	130.10	140.40
Residuals	**ΔY**	- 0.01	-0.01
	ΔX	0.01	0.00
	ΔZ	0.03	0.05
	Horizontal Precision	0.01	0.01
	Vertical Precision	0.02	0.02

GPS coordinates of GCPs and checkpoints

Nos.	Y	X	Z
1	1587.643	3305741.593	87.842
2	1584.209	3305747.817	87.537
3	1568.617	3305801.218	81.644
4	1525.341	3305796.253	79.746
5	1497.273	3305825.987	79.748
6	1457.838	3305825.020	79.706
7	1497.564	3305917.780	79.719
8	1522.453	3305890.448	79.694

10	1537.848	3305917.141	79.654
11	1564.838	3305888.984	79.666
12	1581.381	3305899.853	79.881
13	1583.967	3305843.246	80.515
14	1572.406	3305815.795	80.566

GPS coordinates used for ground truth verification

Nos.	Y	X	Class
1	1437.458	3305852.230	Ground
2	1454.306	3305889.962	Ground
3	1546.979	3305740.329	High Vegetation
4	1573.527	3305921.122	High Vegetation
5	1420.006	3305794.792	Ground
6	1511.571	3305770.962	High Vegetation
7	1511.784	3305839.314	Ground
8	1454.124	3305939.882	High Vegetation
9	1584.151	3305882.215	Ground
10	1437.558	3305899.605	Ground
11	1549.562	3305740.372	High Vegetation
12	1472.423	3305812.522	Ground
13	1553.254	3305811.054	Ground
14	1570.829	3305801.876	Ground
15	1491.424	3305945.241	High Vegetation
16	1520.967	3305815.202	Ground
17	1549.631	3305879.594	Ground
18	1445.126	3305812.431	Ground
19	1522.066	3305760.170	High Vegetation
20	1533.303	3305849.285	Ground
21	1574.588	3305939.286	Ground
22	1462.671	3305786.576	High Vegetation

23	1488.740	3305764.027	Ground
24	1612.280	3305928.312	Ground
25	1556.227	3305844.190	Ground
26	1441.016	3305907.813	Ground
27	1529.318	3305784.147	Ground
28	1458.257	3305860.692	Ground
29	1486.364	3305940.554	Ground
30	1583.210	3305760.045	Building
31	1536.853	3305975.525	Ground
32	1581.232	3305728.826	Ground
33	1533.428	3305861.913	Ground
34	1581.389	3305822.120	Building
35	1620.036	3305886.894	High Vegetation
36	1582.585	3305787.790	Ground
37	1458.623	3305781.756	High Vegetation
38	1460.187	3305866.743	Ground
39	1572.174	3305927.540	High Vegetation
40	1566.530	3305974.814	Building
41	1590.440	3305884.858	Ground
42	1601.625	3305805.571	Ground
43	1500.148	3305922.897	Ground
44	1460.193	3305944.951	High Vegetation
45	1503.527	3305977.114	Ground
46	1558.719	3305788.089	Ground
47	1519.309	3305974.193	Ground
48	1588.620	3305915.788	High Vegetation
49	1607.781	3305845.695	Building
50	1571.607	3305941.527	Ground
51	1547.257	3305964.719	Ground
52	1620.313	3305825.355	Building
53	1424.376	3305797.235	Ground

54	1561.840	3305750.718	High Vegetation
55	1616.031	3305863.792	Building
56	1587.980	3305768.646	Building
57	1578.899	3305801.878	Building
58	1589.218	3305821.881	Building
59	1588.107	3305831.723	Building
60	1599.878	3305829.818	Building
61	1616.206	3305818.864	Building
62	1614.459	3305854.319	Building
63	1623.058	3305873.369	Building
64	1636.552	3305868.209	Building
65	1547.863	3305980.922	Building
66	1484.569	3305777.616	High Vegetation
67	1477.425	3305771.983	High Vegetation
68	1564.010	3305741.425	High Vegetation
69	1548.346	3305753.490	High Vegetation
70	1595.744	3305840.879	High Vegetation
71	1600.374	3305863.369	High Vegetation
72	1558.372	3305913.640	High Vegetation
73	1515.377	3305930.838	High Vegetation
74	1414.173	3305839.226	High Vegetation
75	1500.163	3305881.471	Ground
76	1576.363	3305718.487	Ground
77	1480.055	3305838.079	Ground
78	1534.559	3305960.317	Ground
79	1641.451	3305888.879	Ground
80	1428.196	3305839.667	Ground

Appendix C

GPS coordinates of GCPs and checkpoints in UTM zone 36S

Nos.	X	Y	Z
1	305246.967	6693873.586	87.842
2	305250.509	6693867.422	87.537
3	305267.028	6693814.297	81.644
4	305310.214	6693820.014	79.746
5	305338.797	6693790.770	79.748
6	305378.212	6693792.423	79.706
7	305340.102	6693698.980	79.719
8	305314.740	6693725.877	79.694
10	305299.810	6693698.918	79.654
11	305272.333	6693726.604	79.666
12	305255.980	6693715.448	79.881
13	305252.410	6693772.005	80.515
14	305263.493	6693799.655	80.566